MEASUREMENT OF β-DELAYED PROTONS FROM ^{35}K RELEVANT TO THE $^{34}Cl^{g,m}(p,\gamma)^{35}Ar$ REACTION

A Dissertation

by

ROMAN CHYZH

Submitted to the Office of Graduate and Professional Studies of

Texas A&M University

in partial fulfillment of the requirements for the degree of

DOCTOR OF PHILOSOPHY

Chair of Committee, Robert E. Tribble

Committee Members, Carl Gagliardi

Grigory Rogachev

Charles “Cody” M. Folden III

Head of Department, Grigory Rogachev

August 2019

Major Subject: Physics

ABSTRACT

One of the most challenging problems in nuclear astrophysics is answering a question about the origin and abundance of elements. There are numerous sites in the Universe where new elements can be created. In this particular work two types of extreme stellar environments are in focus: Novae and X-ray bursts. The peak temperatures achieved during a Nova explosion (ONe-type) is around $0.4*10^9$ K, while for an X-ray burst this value can be of order of 10^9 K. Temperature is one of the major factors, which determines how far (by A mass number) the nucleosynthesis can go. While there are numerous reactions to consider in such environments, in this particular study the reaction $^{34}Cl(p,\gamma)^{35}Ar$ was investigated. ^{34}Cl has a relatively short half-life (1.5264(14) s) and can quickly decay into ^{34}S. However this process competes with a reaction of proton capture $^{34}Cl(p,\gamma)^{35}Ar$, thus leaving a smaller amount of ^{34}Cl available for the decay to ^{34}S. The latter, on the other hand, is used for determining isotopic abundances in presolar grains that are extracted from meteorites. Typically, these grains have different isotopic ratios for sulphur than the one found in the Solar System. These differences can say something about the places where the pre-solar grains were synthesized. To be able to accurately predict isotopic abundances in Novae or X-ray bursts, the information about the rate of the reaction $^{34}Cl(p,\gamma)^{35}Ar$ needs to be evaluated. That, in turn, requires some knowledge about the resonances in ^{35}Ar that lie just above proton threshold separation energy (S_p). The fact that only those resonances are important is dictated by the temperatures of the previously mentioned stellar environments. The Gamow window for a temperature of $0.4*10^9$ K is located around 433 keV above S_p level in ^{35}Ar.

An indirect method was used for populating the states above the proton separation energy, S_p, in ^{35}Ar. ^{35}K undergoes β^+-decay into ^{35}Ar and the Q-value of this reaction is sufficiently high to populate states above the S_p level. ^{35}Ar then decayed into ^{34}Cl + p. The spectroscopy of the levels decaying by protons was in the main focus of this work. The AstroBoxII is the detector used in this experiment. It allows low background noise measurements with high efficiency. Also HpGe detectors were used in coincidence with the AstroBoxII to be able accurately

distinguish between states in ^{35}Ar that decay either to the ground state or excited states in ^{34}Cl that then undergo a γ-emission.

The major result of this thesis is the report of a new resonance at 6348(11) keV in ^{35}Ar. This resonance sits right in the middle of the Gamow window (for $T=0.4*10^9$ K) and potentially can have a big impact on the reaction rate of ^{34}Cl(p,γ)^{35}Ar. The estimate for the reaction rate dependence as a function of temperature is given in the Conclusions chapter.

ACKNOWLEDGEMENTS

I wanted to express my sincere gratitude to Prof. Robert E. Tribble, who has been my advisor for this Ph.D. work. His support throughout the whole process was invaluable. He gave me the opportunity to become a student at a great school, Texas A&M University, that completely changed the course of my life. Needless to say about numerous meetings and discussions we had through all these years, sharing his expertise and knowledge with me was an instrumental part in completing this thesis.

I would also like to say thanks to Dr. Antti Saastamoinen, who played an important role in every aspect of the experiment from planning and executing it. Through countless interactions with him I gained the knowledge necessary to do this Ph.D. work.

Also I wanted to say thanks to Dr. Brian Roeder who helped with providing a beam for the experiment and being very helpful as an expert on a variety of topics.

I wanted to mention Dr. Goldberg for his numerous advices on different aspects of Nuclear Physics. I also wanted to say thanks to all our group members and invited scientists who were helping me with performing the experiment as well as Cyclotron Institute staff and a big thanks to the graduate students who helped with the night shifts. I wanted to say words of appreciation to my defense committee members: Prof. Gagliardi, Prof. Folden, Prof. Rogachev as well as Prof. Ko (who could not attend my defense) for their valuable input for the thesis.

Finally, wanted to say thanks to my family and, specifically, to my brother Andrii Chyzh, who inspired me to pursue a Ph.D. degree in USA.

CONTRIBUTORS AND FUNDING SOURCES

This work has been supported by the US DOE Grants. The author thanks to the committee members: Prof. R. Tribble (chair), Prof. C. Gagliardi, Prof. G. Rogachev, Prof. C. Folden as well as Prof. C. Ko (who was a committee member but could not attend the defense). Also major contribution came from Dr. A. Saastamoinen and Dr. B. Roeder who helped tremendously with organizing of the experiment and data analysis. During the experiment we had a visitor from University of Jyvaskyla (Finland) Dr. Anu Kankainen and people from Horia Hulubei National Institute for R&D in Physics and Nuclear Engineering (Romania), Dr. L. Trache and a student I. Stefanescu who helped to setup hardware. E. Pollaco (Universite Paris-Saclay, France) should be credited for his technical assistance during the experiment and off-line tests. A lot of help came from a Dr. Tribble's group former member Dr. A. Spiridon.

TABLE OF CONTENTS

Page

LIST OF FIGURES

Figures Page

LIST OF TABLES

Page

1. INTRODUCTION

1.1 History background

One of the most important questions [1], [2] that the field of Nuclear Astrophysics is trying to answer is the origin of the elements and mechanisms that led to their production. In 1920 it was discovered by Aston that the mass of the helium atom is a bit smaller than the mass of the hydrogen atom multiplied by a factor of four. Almost immediately after that Edington proposed the fusion of hydrogen into helium as a mechanism that generates energy in the Sun. However the temperature of the Sun deduced from the observations was too "small" for what was needed to initiate any nuclear reactions within the star. In 1928 George Gamow [3] provided a comprehensive theory of α-decay which took into account quantum tunneling and the ability of particles to penetrate a potential barrier and initiate a nuclear reaction. And so quantum tunneling would allow nuclear fusion to take place even if the environment was deemed to be too "cold".

In 1932 Cockcroft and Walton [4] produced the first nuclear reaction using artificially accelerated particles:

$$^{7}_{3}Li + p \rightarrow \alpha + \alpha + Q.$$

In the reaction protons were accelerated to a few hundred keV. A reaction of lithium with a proton followed by creation of two α-particles would be later called one of the pp chain reactions [5]. In 1934 Crane and Lauritsen [6] bombarded carbon nuclei with relatively low-energy protons. This reaction would later be known as one of the reactions in the CNO cycle. The fusion of hydrogen as a production energy mechanism in stars was first proposed by Atkinson in 1936 [5]. A detailed theoretical description of the production of solar energy was given by Bethe and Critchfield in 1938 [5]. The energy production mechanism in stars via the CNO cycle was independently developed by Weizsacker in 1938 and Bethe in 1939 [5]. The work of Bethe was in particular the first quantitative attempt in assessing the rate of energy production in the CNO cycle, as well as its temperature dependence.

In the following years the understanding of the formation of nuclei within the stars was theoretically developed by Hoyle [5]. It is important to notice that by then some experimental information had already been accumulated. Very soon a new mystery appeared in the

proposed mechanisms for the production of heavier elements. It was already known at the time that no stable nucleus with the mass number 5 or 8 existed in nature. Therefore it was impossible to tell how these mass gaps could be omitted in the process of formation of heavier nuclei. In 1951 it was suggested by Salpeter [5] that some amount of unstable ${}^{8}_{4}Be$ could capture an α – particle to form a stable ${}^{12}_{6}C$. This process also known as the triple-α reaction was proposed as the main energy source in red giant stars. It is interesting to point out that the probability for ^{8}Be to capture an α – particle would be big enough only if ^{12}C had an excited 0^{+} state at about 7.7 MeV. This level was later verified [7] and so the triple-α reaction was established as the mechanism to bypass mass 5 and 8.

One of the very early milestones in the development of the field of nuclear astrophysics was the discovery by Merrill in the observed atomic spectra (in the paper the results from absorption and emission lines are compared for various stars) of traces of technetium in 1952 [5]. ^{98}Tc is a nucleus with a half-life of $4.2 * 10^{6}$ y. However this is a relatively short time on the cosmological time scale $\sim 10^{10}$ y. This fact pointed to the need for some active sources in the universe that produce technetium.

1.2 Formation of elements

We now know that there is a great variety of mechanisms leading to nuclear reactions in stellar systems. There are several dominant processes in stellar environments, which lead to the creation of new elements. For example, the r-process (rapid neutron capture) [8], [1] is thought to happen when neutron stars or black holes merge and is responsible for producing most neutron-rich heavy nuclei. Another example is the s-process (slow neutron capture) [1], which happens mostly in AGB stars. In this case a nucleus captures a neutron and then can undergo β^{-}– decay, which effectively increases the atomic number and creates a new element. In novae and X-ray bursts one of the most important mechanisms for nucleosynthesis is the rp-process (rapid proton capture process). As its name suggests, a proton is captured by a nucleus thus increasing its atomic number by one. The rate of these reactions will depend of the temperature of the environment, with the probability increasing as the temperature goes up due to Coulomb barrier tunneling. This however is counteracted by the decreasing number of isotopes available for the reaction (this will be discussed in more details in the Theory Chapter). This process

occurs in the environment with the presence of heavier seed nuclei and high temperature to overcome the Coulomb barrier. The work reported here is important for proton capture reaction rates at temperatures that are associated with classical Novae and X-ray bursts [9], [10] where the rp-process plays an important role.

1.3 Classical novae

To better understand classical novae one must first define a white dwarf. At the end of its lifecycle, stars with a relatively small mass (<$10M_{\odot}$) turn into a white dwarf which primarily consists of carbon and oxygen (CO-type) or oxygen and neon (ONe-type)[2], [11], [12]. Further contraction due to the gravitational force is balanced by electron degeneracy pressure. When a white dwarf is in a binary system it can interact with its companion star. The white dwarf can accrete matter from the main sequence star. Eventually as this process continues types of explosive events become possible depending on the mass of the white dwarf and the rate of accretion certain. For a large white dwarf and high accretion rate it is possible to reach the Chandrasekhar limit [13] (the maximum mass of a white dwarf at which electron degeneracy pressure can resist gravitational collapse) and explode as a supernova (type Ia). For a lighter white dwarf and slower accretion rate another type of explosion is possible called classical novae. In the latter process mass transfer between a main sequence star and a white dwarf happens through the Lagrangian point [14] (if an object of a relatively small mass is placed in this point it will not move relative to the other two bodies) of the system. As hydrogen rich matter builds up on the surface of a white dwarf it gets compressed by the gravitational field of the white dwarf. As the temperature and density increases a thermonuclear runaway (TNR) becomes possible. This leads to a massive explosion that is today called a classical nova. The explosion is accompanied by mass ejecta into space. The amount of mass ejected into space is typically $\sim 10^{-4} - 10^{-5}\ M_{\odot}$ at a speed of $10^{2} - 10^{3}$ km s^{-1} [15]. As an example the GK Persei nova is depicted in Fig 1.1. The blue light corresponds to X-ray radiation, the optical part of the spectra is in yellow and radio frequencies are in pink.

Novae are considered to be a common phenomenon in our universe yet only 3-5 are discovered every year, mostly by amateur astronomers. The primary reason for such scarcity is the

presence of interstellar dust which makes it harder to see. The expected rate of novae in Milky Way is around 30 ± 10 yr^{-1} [16]. Unlike a supernova explosion, which completely destroys a white dwarf, novae occur with the typical periodicity 10^4-10^5 years [17]. High energy output makes novae very luminous events with luminosity higher than Solar by several orders of magnitude ($\geq 10^4 - 10^{10}\ L_\odot$).

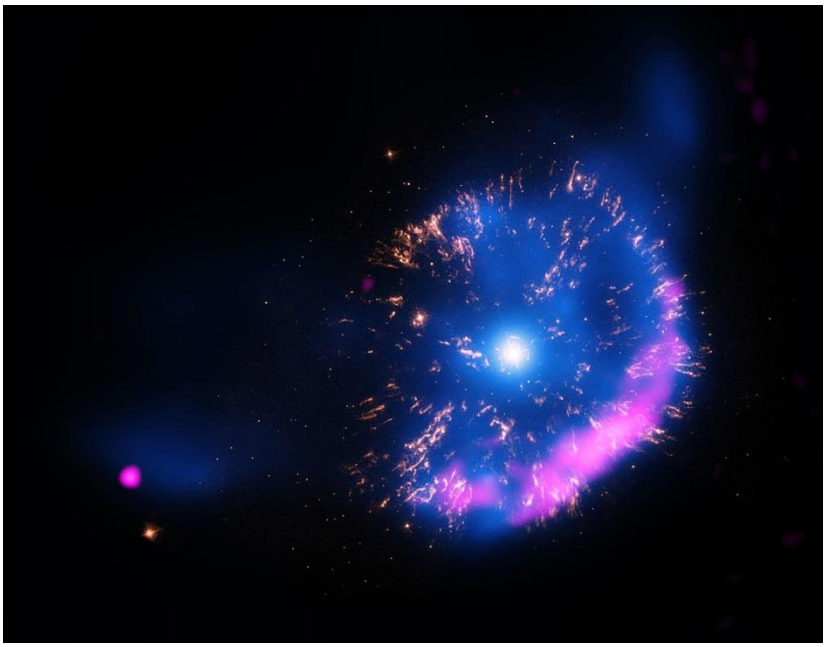

Figure 1. 1 : GK Persei (Nova Persei 1901) Surrounding the nova is the Firework nebula. This picture was obtained by NASA. X-rays are in blue, optical spectrum in yellow and radio data in pink color [18].

1.4 Types of novae

Novae explosions will depend on the type of white dwarf (either CO-type of ONe-type) that is taking part in the process. This difference in the composition of a white dwarf is dictated by the mass of the progenitor star and, as a result, the difference in the evolutionary path that each

type follows. CO-type novae are the most common in the Milky Way and the mass of the progenitor star is around $\sim (9-10)M_{\odot}$. In the case of the ONe-type, the progenitor star mass is bigger and evolution of the star creates a core that is mainly made of oxygen and neon with some traces of magnesium and sodium. The calculated minimum mass of the progenitor star for the ONe-type is $\sim 9.3\ M_{\odot}$ and the resulting mass of a white dwarf is $\sim 1.1\ M_{\odot}$ provided that the evolution of the star happened in the binary system [12]. It is worth mentioning the presence of a CO buffer on top of the ONe core, which prevents mixing of accreted material with the core. The typical range of temperatures reached in the novae explosion is 0.1-0.4 GK. Classical nova explosions on CO type white dwarfs achieve lower peak temperatures and lack a significant amount of NeNa-MgAl nuclei. As a result the main nuclear activity does not go much beyond the production of oxygen. On the other hand the ONe-type nova is characterized by higher peak temperatures and nuclear activity that goes up to silicon ($\sim 1.15\ M_{\odot}$ ONe) and calcium ($\sim 1.35\ M_{\odot}$ ONe) [15]. Therefore the presence of intermediate-mass nuclei in the spectra of novae suggests the type of underlying white dwarf.

1.5 Nucleosynthesis in novae

Nuclear activity in novae happens over a wide range of atomic numbers. Studies of the nucleosynthesis in novae explosions can shed light on many interesting problems in modern astrophysics, such as the creation of ^{7}Li, which is produced by the β-decay (electron capture) of ^{7}Be. In this process, a γ-ray of 478 keV is released. Detection of this signature γ-line has been a problem for decades [2]. Another interesting problem is that of the nucleosynthesis of the CNO group nuclei. The reaction that triggers thermonuclear runaway, ^{12}C(p,γ)^{13}N eventually leads to the creation of ^{13}N, ^{14,15}O, ^{17}F. All of them β-decay into ^{13}C,^{14,15}N, ^{17}O, correspondingly, and in the process release enormous amounts of energy that power the outburst of the novae. These nuclei are among the most abundant in the ejecta following novae explosions.

CO-type novae do not show a significant amount of nuclear activity in the region above the CNO group [15]. However ONe-type novae have more “seeds” of intermediate mass of nuclei as well as higher peak temperature, T_{peak}. These two factors contribute to the much larger

nuclear activity all the way to calcium ($A < 40$). This represents the theoretical endpoint of nova nucleosynthesis and agrees with the observable spectra of ejecta.

Nuclear activity in the Si-Ca region has been scarcely addressed and requires additional experimental and theoretical research. The main reaction that opens up a path to heavier elements is ${}^{30}_{15}P(p,\gamma){}^{31}_{16}S$ which is followed by ${}^{31}_{16}S(p,\gamma){}^{32}_{17}Cl(\beta^+){}^{32}_{16}S$ or by ${}^{31}_{16}S(\beta^+){}^{31}_{15}P(p,\gamma){}^{32}_{16}S$.

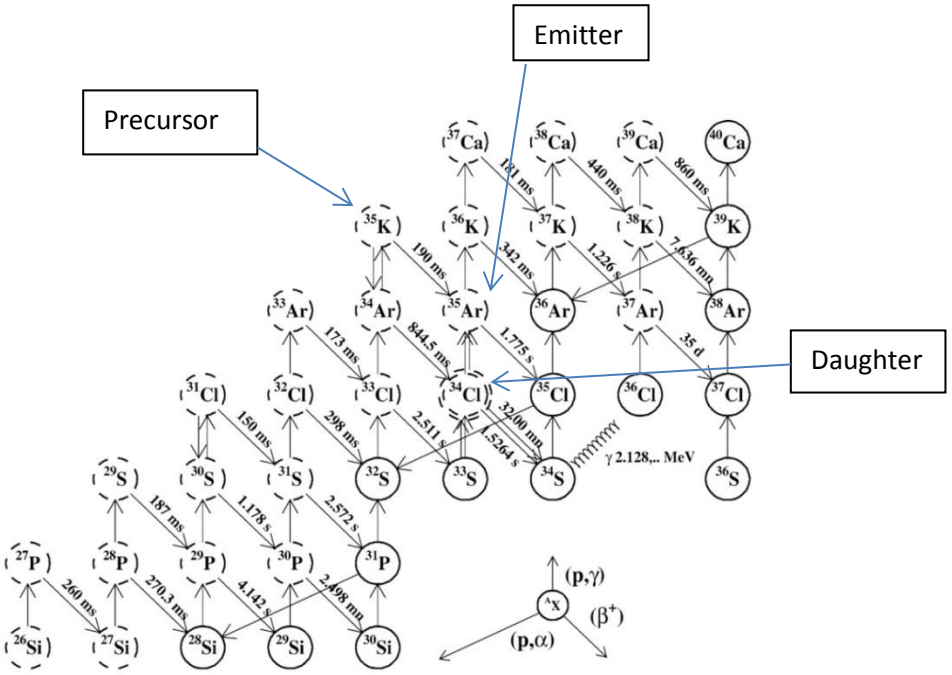

Figure 1. 2 : Nucleosynthesis near the endpoint in novae modified from [15]. Solid circles represent stable isotopes. Dashed circles correspond to radioactive isotopes that can undergo β^+ decay. ^{34}Cl is circled twice as it additionally to ground state (half-life 1.5264 s) has a long lived metastable state (half-life 32min). In some cases (p,α) reaction is possible as shown in the picture.

The currently estimated rates of these reactions are based on theoretical Hauser-Feshbach calculations [12], [15]. The major uncertainty comes from temperatures in novae during the explosions. The rate of this reaction will eventually determine the abundance pattern for heavier elements like S, Cl, Ar, K. In this work one of these elements is studied more thoroughly namely ^{35}Ar.

1.6 X-ray bursts

X-ray bursts are thermonuclear explosions that happen on the surface of a neutron star [19], [20]. They also happen to be the most frequent thermonuclear explosions in the Milky Way. By the total energy output in one burst, they are ranked third right behind novae and supernovae. Around one hundred active X-ray binaries are known today. Soon after the discovery of the X-ray burst in 1975 the mechanism was proposed that explains such events. The system of a binary is similar to novae except that a white dwarf is replaced by a neutron star. The neutron star can accrete the matter from its companion a main sequence star. A strong gravitational interaction then compresses and heats up the accreting matter thus making thermonuclear runaway possible. Fairly soon (1976) the existence of a Rapid Burster was discovered with periodicities of bursts as small as 10 seconds. As a result of this, a new classification was established [21] with the type I and type II X-ray bursts. Type I is associated with thermonuclear flashes and type II is related to instabilities in accretion from the main sequence companion star. Type I XRB is more of an interest for nuclear physics as it is directly linked to the thermonuclear reactions that happen on the surface of a neutron star. Typical light curves of the type I burst display a rise time in the order of 1 to 10 seconds and the decay times somewhere between 10 seconds to several minutes. Periodicities of these kinds of bursts are about one to several hours. Type II on the other hand has reoccurrence times from 7 seconds to 1 hour.

During X-ray bursts, a peak temperature achieved can exceed 1 GK and the density of the material can grow to close to 10^6 g/cm^3. These numbers are significantly higher than those of nova explosions by almost an order of magnitude. As a result realistic modeling of an XRB requires the use of hundreds of isotopes and thousands of different nuclear reactions. This

complicates the process of modeling. It is obvious that the location of the nucleosynthesis endpoint in an XRB will depend on the astrophysical parameters included in the model. Along with novae, X-ray bursts produce isotopes (more so than in novae due to higher peak temperatures) with mass number somewhere between 40 and 100. It was identified in the work of A. Parikh and J. Jose (2013) [19] that the knowledge of the reaction ${}^{34}_{17}Cl(p,\gamma){}^{35}_{18}Ar$, along with others, is important for correctly modeling X-ray bursts.

1.7 Presolar grains

Presolar grains are defined as small pieces of stardust material found in meteorites and in some interplanetary dust particles [22], [12]. When our solar system was formed, it was made out of gas and dust that was supplied by some dying stars. A small portion of this dust remained intact during the Sun formation process about 4.55 billion years ago. Therefore presolar dust grains are the ones that were formed in some sort of ejecta (like novae) and largely remained intact from the moment they were formed. They traveled to the solar system in the form of meteorites. Isolation and extraction of these micron-sized objects is a complicated process. The main reason to study presolar grains is that one can trace isotopic signatures characteristic for certain types of processes like novae. The composition of these grains can reveal some information about the stellar environments where they were formed.

Historically noble gas studies played an important role in the characterization of presolar grains. Trace amounts of these gases can be trapped in meteorites and their isotopic composition is very different to that on Earth. In the studies of dust formation in novae, physicists were looking at the low $^{20}Ne/^{22}Ne$ ratios. The general idea being that ^{22}Ne was presumably formed through decay of ^{22}Na, since ^{22}Ne is a noble gas and does not form any grains. However recently some silicon carbide and graphite grains (from the Murchison and Acfer 094 meteorites) show isotopic signatures that are characteristic of classical novae [23]. These grains were characterized by low $^{12}C/^{13}C$ and $^{14}N/^{15}N$ ratios compared to solar abundances. Along with these the ratio of $^{29}Si/^{28}Si$ was slightly lower than solar. These findings provide valuable information about possible constraints for nova nucleosynthesis models.

1.8 ^{35}Ar problem

The thermonuclear reaction rate for ${}^{34g,m}_{17}Cl(p,\gamma)^{35}_{18}Ar$ is uncertain due to lack of experimental data about low lying resonances in ^{35}Ar [24]. In the ONe-type novae, production of ^{34}S depends on the amount of ^{34}Cl. The reaction ${}^{34g,m}_{17}Cl(p,\gamma)^{35}_{18}Ar$ takes place alongside the destruction of ^{34}Cl by means of β-decay with a half-life $t_{1/2}$=1.5266 s. These two processes compete with each other and the production of ^{34}S will eventually be strongly dependent on the nuclear reaction rate of ^{34g,m}Cl(p,γ)^{35}Ar. In the model study done by Iliadis *et al*., it was determined that varying the rate of this reaction by a factor of 100 will change the final abundance of ^{34}S by a factor of five [11]. Also information about sulfur isotopic ratios can help in the classification of presolar grains. It is interesting to note that in the current nova models, reaction rates of ^{33}S(p, γ)^{34}Cl and ^{34}Cl(p, γ)^{35}Ar are calculated without consideration of the first excited isomeric state of ^{34m}Cl (half-life $t_{1/2}$=31.99min). However, the most recent work by Grineviciute *et al.,* which was studying the role of excited state in proton capture reactions, shows that ^{34m}Cl may be playing a larger role than was previously believed.

1.9 The Spectroscopy of 35Ar

The first studies of ^{35}Ar levels date back to 1968 in works done by Kozub et al. [25] and R. R. Johnson et al. [26]. The first measurements were done at the Michigan State University cyclotron. A beam of protons at 33.6 MeV was used on the gaseous target consisting of ^{36}Ar. A reaction ^{36}Ar(p,d)^{35}Ar was used to populate states in ^{35}Ar followed by gamma emission. The reaction products were measured by a telescope detector consisted of silicon surface-barrier detector (ΔE) and lithium-drifted silicon counter (E).

Energy, MeV	Spin-parity, J^{π}
6.82(3)	$3/2^{+}$, $5/2^{+}$
6.62(3)	
6.01(3)	$3/2^{+}$, $5/2^{+}$

Table 1. 1: ^{35}Ar level assignment for the states above S_p from ^{36}Ar(p,d)^{35}Ar reaction in from the work of R. L. Kozub modified from [25]

The proposed levels in ^{35}Ar are shown in the Tab 1.1. As can be seen there were three levels reported in this work that are located above proton threshold separation energy (S_p=5896.3 keV): 6.01(3) MeV, 6.62(3) MeV, and 6.82(3) MeV. All three are located in the astrophysical relevant region. The same (p,d) reaction was used in the work of R. R. Johnson et al. [26]. The beam produced at the University of Colorado Nuclear Physics Laboratory had an energy of the incident protons of 27.5 MeV. The measurements were done with a semi-conductor detector telescope. There were three states above S_p level reported in that work: 6.03(2) MeV, 6.70(2) MeV, and 7.03(2) MeV. The state 6.01(3) MeV from the reference [25] and the state 6.03(2) from the reference [26] are assumed to be the same state from Nuclear Data Sheets. Another extensive study of levels in ^{35}Ar was done by R. R. Betts at al. [27]. The reaction used in their studies was ^{36}Ar(^{3}He,α)^{35}Ar with an energy of incident ^{3}He of 18 MeV. The experiment was done at the University of Pennsylvania tandem Van de Graaff accelerator. Reported in that work was the discovery of many new levels above S_p level for ^{35}Ar. Along with that angular distributions for certain levels were presented. Two of those that were above S_p had spin-parity assignment made for them 6033 MeV (J^{π}=$3/2^{+}$,$5/2^{+}$) and 6631 MeV (J^{π}=$1/2^{+}$). Also there was a comparison presented between the experimental and the theoretical shell model calculations (multiple models) showing good agreement overall.

The first attempt to measure β-delayed protons from ^{35}Ar was published in the article by G. T. Ewan at al. in 1980 [28]. The ^{35}K isotope was produced at the ISOLDE facility at CERN. The

production method was the ^{45}Sc(p,8n3p) reaction. The gamma spectrum was collected with a Ge(Li) detector with a resolution of 2.1 keV FWHM at 1.33 MeV. The β-delayed charged particle spectrum was collected with a detector telescope consisting of two silicon surface barrier detectors. The gamma rays with energies up to 5 MeV were collected. The β-delayed protons reported in this work is shown in Table 1.2

Peak number	E_p(lab), keV
1	1282(20)
2	1425(20)
3	1555(20)
4	1705(20)
5	1875(20)
6	1980(20)

Table 1. 2: The list of β-delayed protons (up to 2000 keV above S_p level) reported in the article by G. T. Ewan et al. modified from [28]

As can be seen the lowest energy protons were at 1282(20) keV. This is somewhat high for resonances that can be important for typical Novae temperatures (0.1-0.4 GK).

One of the most recent experiments regarding the states in ^{35}Ar was described in a paper by C. Fry, *et al*. [24]. They used the reaction ^{36}Ar(d,t)^{35}Ar to produce different states of ^{35}Ar. ^{36}Ar was implanted into a carbon foil and a beam of deuterons of 22 MeV was used in their experiment. They claim the discovery of 17 new states in ^{35}Ar above the proton separation energy (S_p= 5896.3(8) keV for ^{35}Ar) [29]. However they could not tell the spin and parity of those states so the

resonance strength of the states cannot be estimated from their measurements. For calculations of the thermonuclear reaction rates, knowledge about the energy as well as spin and parity of the states is essential. The importance of low lying resonances close to S_p level in ^{35}Ar will be revealed in more detail in the theory section.

A recent paper by P. Banerjee et al. [30] on effective stellar beta decay rates of nuclei with long-lived isomers discusses the dependence of effective beta decay rate for the ground state and the long-lived (half-life ~ 32 min) isomeric state in ^{34}Cl. These two states connect to each other by an M3 gamma transition, which gives weak coupling. However at the typical temperatures of Novae explosions and X-ray bursts the likely scenario is the communication of the isomeric state (IS) and ground state (GS) through the 1^+ state at 461 keV. This state couples to the GS by an M1 transition and to the IS by an E2 transition [30]. This can lead to a big uncertainty in the production of ^{35}Ar, since the reaction ^{34m}Cl(p,γ)^{35}Ar also has to be considered as a significant contributor to the creation of ^{35}Ar. In that paper it was calculated that the effective β-decay rates for the ground state and isomeric state in ^{34}Cl merge together at the temperature ~0.3 GK.

To be able to accurately predict the reaction rate of ^{34}Cl(p,γ)^{35}Ar, one needs to know the resonances in ^{35}Ar, including - their energy, spin-parity, and proton width. Today, very little is known about the states above S_p (proton threshold separation energy) in ^{35}Ar. The method used in the present dissertation allows an extraction of spectroscopic information along with some restriction of spin-parity assignment of the states.

2. THEORY

2.1 Historical background

An important part of an indirect technique that is used in this work is β-decay. β-decay from a parent nucleus is used to populate states in the daughter nucleus that may be relevant in the proton capture reactions that take place in novae. In the present work it is β^+ decay that is used to transform a proton heavy nucleus with Z protons into a daughter nucleus with (Z-1) protons. During this process it is possible that a daughter nucleus will end up being in the ground state and this case is irrelevant to us. However it is also possible that a nucleus after β decaying will end up in some excited states and they can have some astrophysical significance. So knowing the fundamentals of β-decay is essential for understanding the population of resonances of the nucleus of interest.

The history of discovery and theoretical description of β-decay has always been filled with mysteries. In 1934 the Joliot-Curies first observed emission of positrons following the reaction $^4He + ^{27}Al \rightarrow ^{30}P + n$ [3]. At the time of the discovery it was already established that β particles were not present in nuclei. It suggested that there was a new kind of process that is different from α-decay which was already known at the time. Another puzzling characteristic of β-decay was the fact that the spectrum of β-particles was continuous. In α-decay the spectrum of the emitted α-particles had a well-defined peak. Its energy was equal to the difference between the energies of initial and final state of a nucleus. In 1931 Pauli proposed his explanation to this phenomenon, claiming that there was another particle involved in β-decay process. Conservation of charge and momentum required it to be electrically neutral and to have spin $\frac{1}{2}$. This particle was interacting very weakly with matter and therefore it was not detected in the initial experiments that involved β-decay. Fermi proposed the name “neutrino” for the particle. In the 1956 an article [31] by C. Cowan, F. Reines, F. B. Harrison, H. W. Kruse and A. D. McGuire was published in which authors claimed an experimental discovery of the neutrino. Almost forty years later the authors were awarded the Nobel Prize for their discovery. The physics

behind the neutrino has been full of surprises, but in this work β-decay is looked at from a different prospective.

The three the most basic β-decay like processes are shown below:

$n \rightarrow p + e^- + \bar{\nu}$ negative β^-- decay or neutron decay ($\bar{\nu}$ – stands for antineutrino)

$p \rightarrow n + e^+ + \nu$ positive β^+- decay or proton decay

$p + e^- \rightarrow n + \nu$ electron capture

It is convenient when writing β–decay energetic equations (1), (2), (3), (4) to use atomic mass units. Consider first β^-–decay. When a neutron is transformed into a proton the daughter nucleus has its charge increased by one. To neutralize the newly formed ion one needs to add one electron. Coincidentally in β^- - decay we already have an emitted electron. Neglecting the difference in binding energies of electrons in parent and daughter nuclei one can write a fairly simple equation for Q_{β^-} value. The rest mass of the antineutrino is sufficiently small that the energy balance equation for β^- - decay can be written [3], [5]:

$$Q_{\beta^-} = \{[m({}^A_Z X) - Zm_e] - [m({}^A_{Z+1} X) - (Z+1)m_e] - m_e\} * c^2. \qquad (2.1)$$

After some simplifications it can be written as follows:

$$Q_{\beta^-} = [m({}^A_Z X) - m({}^A_{Z+1} X)] * c^2, \qquad (2.2)$$

where $m({}^A_Z X)$ is atomic mass of parent atom, $m({}^A_{Z+1} X)$ atomic mass of daughter atom, m_e and Z is respectively mass of electron and the number of protons in parent nucleus the equation (2.1). Similar logic can be used for deriving expression for β^+–decay. In this case a proton is transformed into a neutron and the charge of a nucleus is reduced by one. It is worth mentioning that a free neutron can decay into a proton (with half-life 613.9(6) s [32]). It is energetically impossible to observe a decay of a free proton by means of β - decay. In β^+ - decay a proton transforms into a neutron reducing the charge of the nucleus by one. As a result the atom in which the decay takes place would have to lose one electron. If written in atomic mass units the energetic equation for β^+ - decay will look like this [3], [5]:

$$Q_{\beta^+} = \{[m(^A_Z X) - Zm_e] - [m(_{Z-1}{}^A X) - (Z-1)m_e] - m_e\}c^2. \quad (2.3)$$

In the right hand side, m_e stands for the mass of the positron, but since that is equal to the mass of electron it is convenient to write it as the mass of electron.

This can also be simplified so the final equation will look like:

$$Q_{\beta^+} = [m(^A_Z X) - m(_{Z-1}{}^A X) - 2m_e]c^2. \quad (2.4)$$

As it follows directly from the above equation, β^+–decay has a threshold and the difference in atomic masses of parent and daughter nuclei has to be bigger than $2m_e c^2 = 1.022$ MeV. Those elements that are created in some stellar environments via (p,γ) reactions have an abundance of protons and very often undergo β^+ - decay moving closer to the stability region in the table of elements. Finally in the case of electron capture the equation for the Q value can be written as follows:

$$Q_e = [m(^A_Z X) - m(_{Z-1}{}^A X)]c^2 - B_n. \quad (2.5)$$

In this case we have a term B_n that is not negligible. It presents the binding energy of the captured electron. Since electron capture happens mostly for inner shell electrons, the binding energy can be of the order of a few tens of keV. In this case right after electron capture a newly created vacancy is quickly filled with another atomic electron accompanied by X-ray emission. The Q –value for the electron capture in the case of ^{35}K is 11874.5(9) keV [33].

If certain conditions are met, it is possible for a given nucleus to decay by two different modes: positron β^+-decay and electron capture. They both will produce the same daughter nuclei. As a result these two processes will compete against each other. As it is clear from the equations (4) and (5) for positron decay and electron capture, the latter is energetically more beneficial. In particular when the condition

$$0 < [m(^A_Z X) - m(_{Z-1}{}^A X)] < 2m_e$$

is met electron capture is allowed but positron β^+-decay is forbidden. In general if two channels are available (β^+ and electron capture) the transition probability per unit time is then given by a simple sum of the two.

$$\lambda^+ = \lambda^{\beta^+} + \lambda^{EC}, \tag{2.6}$$

where λ^{β^+} stands for the transition probability per unit time given only by β^+–decay, and λ^{EC} represents the transition probability per unit time for electron capture. It can be shown that the $ft_{1/2}$ value in this case is determined by [34]

$$ft_{1/2} = [f^+ + f^{EC}]t_{1/2} = \frac{k}{B_F + B_{GT}}, \tag{2.7}$$

where B_F and B_{GT} are Fermi and Gamow-Teller reduced transition probabilities respectively, and k is a constant given by $k \equiv \frac{2\pi^3\hbar^7 ln2}{m_e^5 c^4 G_F^2}$. For energies higher than 2 MeV the half-life of the β – decay is determined by the β^+ decay, but for small energies electron capture dominates the decay branch and for the decay energy below 1.022 MeV electron capture is the only one possible.

It is important to briefly mention the definition of decay constant, half-life, and mean lifetime as these physical quantities frequently appear in the present dissertation. If there are N radioactive nuclei at time t, then the time evolution of this number will be determined by the equation [3], [5]

$$\lambda = -\frac{\frac{dN}{dt}}{N}, \tag{2.8}$$

where λ is called decay constant. This quantity is defined in such way that the right-hand side of the equation (2.8) gives probability per unit time for a decay to occur. It is assumed that this value remains constant regardless of the age of the nuclei. Integration of the differential equation (2.8) gives a simple result:

$$N(t) = N_0 e^{-\lambda t}. \tag{2.9}$$

The relation (2.9) allows calculation of the number of remaining nuclei $N(t)$ after the time t has elapsed since the measurement was taking place, where the initial number of nuclei was N_0. The half-life $T_{1/2}$ is extracted from the equation (2.9) putting $N = N_0/2$. This yields simple relation between half-life and decay constant

$$T_{1/2} = \frac{ln2}{\lambda}. \tag{2.10}$$

Mean lifetime τ by definition is the time required for N to fall by a factor $1/e$. After working out simple math from the equation (2.9) mean lifetime is given by

$$\tau = \frac{1}{\lambda} = 1/ln2 * T_{1/2}. \tag{2.11}$$

If there are multiple decay channels available for a given nucleus the total decay probability will be determined by the sum of the decay probabilities of each individual channel. Therefore one can write useful expressions [3], [5]

$$\lambda = \sum_i \lambda_i \quad \text{or} \quad \frac{1}{\tau} = \sum_i \frac{1}{\tau_i} \tag{2.12}$$

2.2 Fermi and Gamow-Teller transitions

A complete β-decay theory goes well beyond the scope of this thesis, but two types of β-decay transitions are important in the present work: Fermi transition and Gamow-Teller transition [34]. By definition allowed beta decay has the leptons emitted in a s state relative to the nucleus ($l = 0$). There are other types of transitions called forbidden. They are characterized by higher values of leptons orbital momentum, but have orders of magnitude smaller transition probability values and in the present work do not play a significant role [5].

In a Fermi transition the spins of the emitted particles (β-particle and (anti-)neutrino) are antiparallel and the total spin is $S = 0$. Also in a Fermi type transition a nucleon does not change its shell-model orbital. Therefore a Fermi transition (also known as superallowed) happens between analog states of a parent and a daughter nucleus. (These states are also known as isobaric analog states [3], [35]. If one considers two nuclei ^{A}X and ^{A}X' there is at least one state in the nucleus ^{A}X' that has very similar nuclear structure and properties as the

reference nucleus ^{A}X. These states have the same spin, parity and isospin. The existence of the isobaric analog state is closely related to the fact that a proton-proton, a proton-neutron, and a neutron-neutron interaction are very similar in nature. Only coulomb forces account for some difference in the nuclear structure of the two analog states in two isobaric nuclei.) As a result the net change of angular momentum is zero ($\Delta J = 0$). An important characteristic of both Fermi and Gamow-Teller transitions is the conservation of parity ($\Delta\pi = 0$). As an example we can consider the decay of ^{35}K: $^{35}_{19}K \rightarrow {}^{35}_{18}Ar + \beta^{+} + \nu_e$. In this case the initial state is $J_i = 3/2^{+}$ and the final state $J_f = 3/2^{+}$ so the net change of angular momentum $J_f - J_i = 0$.

In a Gamow-Teller transition the spins of the emitted β-particles and (anti-)neutrino couple to total spin ($S = 1$). As a result the total angular momentum can be either changed by 1 or remain the same. So the difference between the final and the initial the angular momentum of the nucleus is $\Delta J = 0, \pm 1$. In the literature Fermi transitions and Gamow-Teller transitions are often called s*uper-allowed* and *allowed* decays [3], [5] correspondingly. It is worth mentioning that the number of β-decay transitions is more than just two. And the change in angular momentum can be more than $\Delta J = 1$. Those transitions are often referred to as *forbidden.* Somewhat an inaccurate name as they are not forbidden completely but suppressed compared to Fermi and Gamow-Teller transitions. In the present text, as noted above only s*uper-allowed* and *allowed* decays are considered as the transition probabilities for *forbidden* decays are typically many orders of magnitude smaller.

The expression for transition probability per unit time is given by Fermi's Golden Rule (2.13). It is written in the form of [3], [5]

$$\lambda = \frac{2\pi}{\hbar}\left|V_{fi}\right|^2 \rho\left(E_f\right), \tag{2.13}$$

where $\rho\left(E_f\right)$is the density of the final states and V_{fi} are the matrix elements of the interaction V between the initial and final states. When working out the expression for V_{fi} elements, the final wave function will be a multiplication of the three wave functions of the nucleus, electron and neutrino. The expression for the latter two is given in a free-particle form:

$$\phi_e(r) = \frac{1}{\sqrt{V}} e^{p*r/\hbar} \tag{2.14}$$

$$\phi_\nu(r) = \frac{1}{\sqrt{V}} e^{q*r/\hbar} \tag{2.15}$$

The expressions (2.14) and (2.15) are already normalized in the volume V and p and q stand are the momenta of the electron and neutrino correspondingly. If $p/\hbar$ and $q/\hbar$ are small then only the first term in Taylor expansion is relevant. Therefore the exponent is essentially replaced by a numerical value 1. The resulting transition probabilities calculated from equation (2.13) will give an allowed approximation. Skipping the math while working out equation (2.13) one arrives at an expression, which is known in the literature [3], [5] as the Fermi integral. It is a dimensionless integral that is directly related to the expression for transition probability and is represented as

$$f(Z', E_0) = \frac{1}{(m_e c)^3 (m_e c^2)^2} \int_0^{p_{max}} F(Z', p) p^2 (E_0 - E_e)^2 \, dp. \tag{2.16}$$

Where $p^2(E_0 - E_e)^2$ is a statistical factor that can be obtained from the number of final states in β–decay and $F(Z', p)$ is the Fermi function that takes into account the nuclear Coulomb field.

A very useful physical quantity that is used to describe β-decay is the comparative half-life (ft-value):

$$ft_{1/2} = ln2 \frac{2\pi^3 \hbar^7}{g^2 m_e^2 c^4 |M_{fi}|^2}. \tag{2.17}$$

Where m_e stands for the mass of electron, M_{fi} are nuclear matrix elements, and the value of the constant g determines the strength of the interaction. It is often used as a measure of β-decay probabilities in different nuclei as bigger values of $ft_{1/2}$ represent decays of higher probability. Since charge and energy are already included in f, the differences between $ft_{1/2}$ values must be explained by the differences in M_{fi} matrix elements. The range of ft – values is very broad from 10^3 to 10^{20} s [3]. So instead of using ft – value it is often the log ft – value that is quoted. Superallowed decays normally have log $ft \cong 3 - 4$.

2.3 Basics of shell model

To be able successfully explain and predict experimental results one needs to have a good model for the processes that take place in nuclei. The difficulty of creating a complete nuclear model is related to the fact that the information about nuclear forces is not fully known and various approximations are used [3], [36]. Another problem arises from the fact that even if such information was available, calculating the wave function of a nucleus (especially heavier nuclei) would be nearly impossible. The three body problem in classical mechanics does not have an analytical solution and an attempt to solve a similar problem for a larger number of particles while taking into account their quantum mechanical properties is not feasible. Luckily, to build a successful nuclear model one does not necessarily need to have all the information about the microscopic state of the system. Likewise in statistical physics only a few parameters are used for the description of the properties of a gas like temperature and pressure and information about each individual particle (its momentum and coordinates) are not needed.

Coverage of the full history of nuclear model development goes well beyond the scope of this dissertation. An example of the earlier attempt to describe a nucleus was made by N.Bohr [36] in his liquid drop model. However very quickly it became obvious that it could not explain the non-spherical shape of some nuclei, as well as correctly calculate quadrupole moments of nuclei. Eventually the single-particle model was chosen as the most accurate one for light nuclei [36]. One of the key characteristic of this type of model is the assumption that a nucleon (either proton or neutron) moves inside of a nucleus that has some average potential. The development of the nuclear shell model like any physical model was based on the experimental results. It turned out that some nuclei require a lot higher energy for separation of a nucleon than others. Nuclei with Z (number of protons) or N (number of neutrons) of 2, 8, 20, 28, 50, 82, 126 were called magic nuclei [36], [3]. The energy required to take away one nucleon from these nuclei is much higher than the average separation energy. Those nuclei that had both Z and N magic numbers were called doubly magic and were especially strongly bound. The analogy between the atomic shell model and experimental results for nuclei was apparent. However Z values for inert atoms are different 2, 10, 18, 36, 54, 86. Atoms with these Z values have spherical symmetry, are chemically inactive and have high ionization energy. However as

it can be seen from direct comparison the magic numbers for nuclei and for atoms are different (except for the first one). So the motion of a nucleon inside of a nucleus is governed by the average potential created by all the nucleons. Nucleon density stays relatively constant all across the nucleus and quickly drops to zero near the surface of the nucleus. It was convenient to choose an analytical form of the potential which takes into account this fact. Such a potential also has to be spherically symmetric. For light nuclei it was discovered that potential for harmonic oscillator [36] works really well, so:

$$V(r) = \left(\frac{1}{2}\right) m\omega^2 r^2 \tag{2.18}$$

for $r < R$ and $V(r) = 0$ for $r > R$, where R – radius of the nucleus, ω is an angular frequency of the oscillator, and m is a mass of the oscillating particle. After choosing the potential we need to solve the Schrodinger equation for a harmonic oscillator. Let us first take a look at what magic numbers are going to be like if we use only the potential of the harmonic oscillator form. The energy spectrum of a one dimensional potential is given by:

$$E_x = \left(n_x + \frac{1}{2}\right) \hbar\omega. \tag{2.19}$$

Where E_x is the energy of a one-dimensional oscillator and n_x is the main quantum number. An analogous expression can be written for E_y and E_z so the total energy of a three dimensional oscillator is:

$$E = E_x + E_y + E_z = \left(n + \frac{3}{2}\right) \hbar\omega, \tag{2.20}$$

where $n = n_x + n_y + n_z$. Quantum numbers $n_x,\ n_y,\ n_z$ can only be positive integers or zero. It is important to note that the energy levels of three dimensional oscillator are degenerate and equal $(1/2)(n+1)(n+2)$ so for the case of $n = 1$ energy levels are three times degenerate. For the case of $n = 2$ levels are six times degenerate. Now if we take into account the projection of the spin of the nucleon which can be $+1/2$ or $-1/2$ the number of the states that correspond to the same energy needs to be doubled. It is natural to assume that to each n corresponds to a new shell. Therefore in the model of the three dimensional harmonic oscillator the numbers of nucleons in each shell would be 2, 6, 12, 20, 30, 42 [36]. The magic

numbers are obtained by adding every of these numbers to the sum of the previous numbers. So the magic numbers will be 2, 8, 20, 40, 70, 112. The first three numbers coincide with the experimentally observed magic numbers, but the rest are different namely 28, 50, 82, 126. This discrepancy must be related to the fact that the form of a nuclear potential chosen for this problem was not exact. In the 1940s nuclear scientists were looking for a correction that needed to be added to the potential to match the observed magic numbers. Mayer and Jensen in 1949 [36] showed that adding a term which takes into account a spin- orbit interaction cures the problem. The spin of the nucleon can be directed along its orbital momentum or against it. The resulting energies for these states will be going up or down correspondingly. This shift of levels must be appropriately taken into account to obtain the observed magic numbers. The spin-orbit interaction is taken into account by the choice of the Hamiltonian in the Schrodinger equation $\widehat{H}\psi = E\psi$. The Hamiltonian has a form:

$$\widehat{H} = V(r) + U(r)\boldsymbol{s} * \boldsymbol{l}, \tag{2.21}$$

where $\boldsymbol{s}$ is the vector of the spin of a nucleon, $\boldsymbol{l}$ – orbital momentum of the nucleon. As it was mentioned before vectors $\boldsymbol{s}$ and $\boldsymbol{l}$ can be parallel or antiparallel. The potential $V(r)$ usually has a shape that resembles a well but with slightly rounded edges and eventually approaches zero. $U(r)$ is a centrally symmetric potential and is weaker than $V(r)$. The potential $U(r)$ has a shape that is usually expressed like [36]:

$$U(r) = b\frac{1}{r}\frac{\partial V}{\partial r}. \tag{2.22}$$

Where b is called a constant of the spin-orbit interaction. Energy levels in a nucleus are calculated from the Schrodinger equation with the Hamiltonian mentioned above that is empirically chosen. The form of $U(r)$ does not play a big role, rather what matters here is the $\boldsymbol{l} * \boldsymbol{s}$ factor. In the similar way as in atomic physics it is convenient to characterize the states by the total angular momentum:

$$\boldsymbol{j} = \boldsymbol{l} + \boldsymbol{s}. \tag{2.23}$$

Since the spin of a nucleon is $s = 1/2$ the possible values for the total angular momentum are $j = l + 1/2$ or $j = l - 1/2$ in the parallel and antiparallel configurations respectively. The special case when $l = 0$ gives only one possible value for $j = 1/2$. The expectation value of $\boldsymbol{l} * \boldsymbol{s}$ can be calculated by squaring both sides of the equation for $\boldsymbol{j} = \boldsymbol{l} + \boldsymbol{s}$:

$$\boldsymbol{j^2} = (\boldsymbol{l} + \boldsymbol{s})^2 = \boldsymbol{l^2} + \boldsymbol{2}\, \boldsymbol{l} * \boldsymbol{s} + \boldsymbol{s^2}. \tag{2.24}$$

From this expression $\boldsymbol{l} * \boldsymbol{s} = 1/2(\boldsymbol{j^2} - \boldsymbol{l^2} - \boldsymbol{s^2})$ and finally substituting expectation values for $\boldsymbol{j^2}$, $\boldsymbol{l^2}$, $\boldsymbol{s^2}$ [37], [38] we obtain

$$\langle \boldsymbol{l} * \boldsymbol{s} \rangle = \tfrac{1}{2}[j(j+1) - l(l+1) - s(s+1)]\hbar^2. \tag{2.25}$$

Likewise in atomic physics states with $l = 0, 1, 2, 3$ … correspond to letters s, p, d, f. The filling of each state in a nucleus happens in accordance to Pauli principle so that two nucleons cannot be in the same state. The number of nucleons in each shell is determined by the degeneracy of each level which is equal $(2j + 1)$. Taking into account the spin-orbit interaction for $l = 0$ we have $j = 1/2$ and so the total number of nucleons in the shell is 2. That corresponds to $1s_{1/2}$ state. The next one is $l = 1$. This will produce two values of $j = 1 - \frac{1}{2} = \frac{1}{2}$ and $j = 1 + \frac{1}{2} = \frac{3}{2}$. The total number of nucleons in the shell will be given by $2 + 4 = 6$ nucleons and the total number of nucleons in the nucleus is the sum of shell with $j = 0$ and $j = 1$ and that will give 8 nucleons. The first two examples give the explanation to the magic numbers 2 and 8, but the same logic is applied for the derivation of the rest of the magic numbers.

The success of the nuclear model in explaining magic numbers was historically strong and important in accepting this model. The shell model was also instrumental in explaining the spins and parities of the nuclei.

2.4 Nucleon decay

When a nucleus undergoes β^+- decay this creates a different element with the Z number reduced by one. An important physical quantity that needs to be defined here is the proton separation threshold energy S_p. It is written as [3]

$$S_p = \left[(m(^A_Z X) + m_p) - m(^{A+1}_{Z+1}X)\right]c^2, \quad (2.26)$$

where m_p is the mass of a proton. From equation (2.26) it becomes obvious that positive values of S_p will correspond to a situation when one needs to supply an emitter with excess of energy otherwise nucleon emission is energetically impossible. For the case when ^{35}K decays into ^{35}Ar, the S_p value for the latter is 5896.3 keV [29]. However, the newly created nucleus (^{35}Ar) will not necessarily be in the ground state. It will be in the states allowed by the selection rules of β^+-decay. If the excitation energy of one of these states is above S_p (proton separation threshold energy) proton emission becomes energetically feasible. In the literature [3] the original nucleus that undergoes β^+- decay is called the precursor and the nucleus that emits the proton is called the emitter. And following the logic of the naming, the nucleus created after proton emission is called the daughter. The spectrum of protons is determined by two factors: the intensity of the transition from the precursor to the emitter (namely unbound states that have enough energy to undergo proton decay) and the branching ratio for the proton emission which competes with γ-decay. From the theory of β delayed proton emission it is known that the probability of proton decay versus gamma decay grows with the excitation energy of the state of the emitter [3]. However the rate at which the states in the emitter are populated by β-decay decreases with higher energy. These two competing processes eventually will determine the energy spectrum of protons. The intensity of the transition from a state *i* in the emitter to a state *f* in the daughter can be written in the following way (true if only proton and gamma decays are considered):

$$I_p^{if} = I_\beta^i \frac{\Gamma_p^{if}}{\Gamma_p^i + \Gamma_\gamma^i}. \quad (2.27)$$

Where I_β^i is the beta decay branching ratio from the precursor to a state *i* in the emitter, Γ_p^{if} partial width for proton emission between states *i* and *f*, Γ_p^i full proton width of the i^{th} state, and Γ_γ^i full gamma decay width of the i^{th} state of the emitter.

Experimentally it was determined that the β-delayed proton spectrum greatly depends on the atomic mass and charge of the precursor [3], [39]. For light nuclei the β-decay feeds the levels

in the emitter that have relatively low density. And when the final proton spectrum is measured the peaks are separated well. The general decay scheme of beta-delayed proton emission is shown in Fig. 2.1:

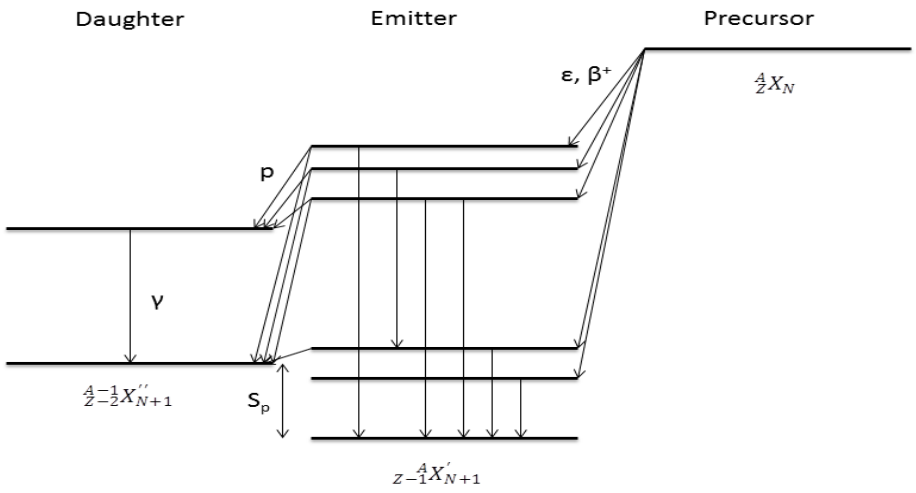

Figure 2. 1: Beta-delayed nucleon emission schematic. After β+ or EC process precursor nucleus turns into an emitter. Electric charge is reduced by one unit, but the mass number stays the same (A). Following that an emitter can de-excite by either gamma emission or proton emission (multiple variations are possible).

In the case studied here ^{35}K is the precursor, ^{35}Ar is the emitter and ^{34}Cl is the daughter. ^{35}K (half-life 178(8) ms) [29] after undergoing the β-decay can populate states in ^{35}Ar according to the selection rules if some of the populated states lie above proton separation threshold energy (S_p), the possibility for proton decay opens up. These states can also decay by γ-emission and so these two processes always compete with each other. For ^{35}Ar, S_p=5896.3(8) [29] keV. In the literature there are a lot of states that lie above S_p. Many of these states, especially those that lie just above S_p do not have assigned spins and parities. The method deployed in this work does not provide accurate information about spins and parities but can give some constraints to these values. ^{35}K has the ground state with spin parity $J^{\pi} = (3/2)^{+}$ [29] and the states in

^{35}Ar that are populated through Fermi transition can only have $(3/2)^+$and Gamow-Teller transitions $(1/2)^+$, $(3/2)^+$, $(5/2)^+$.

2.5 Gamma decay

When a nucleus (precursor) undergoes β-decay it can populate states in the emitter other than the ground state. These states are called excited states. The electromagnetic radiation that occurs when a nucleus goes from excited states to energetically lower states is called gamma radiation. A gamma spectrum is always discrete since the levels of nuclei are discrete. When a nucleus goes from an excited state to an energetically lower state it may not necessarily reach the ground state in one transition. In this case we can see cascades of gamma radiation and instead of one gamma ray we see two or even more.

There are two types of γ-radiation that correspond to the change in electric and magnetic multipoles respectively. The parity of the radiation field is given [3], [34] by two following formulas:

$$\pi(ML) = (-1)^{L+1} \tag{2.28}$$

$$\pi(EL) = (-1)^{L} \tag{2.29}$$

Here L stands for the order of multipole. It is interesting to note that magnetic and electric fields of the same order of multipole always have opposite parity. It is convenient to characterize gamma decay by the probability per unit time λ. There are some good approximations developed for electric and magnetic multipole transitions. For electric transitions probabilities are given by [3] in units s^{-1}

$$\lambda(E1) = 1.0 * 10^{14} A^{2/3} E^3 \tag{2.30}$$

$$\lambda(E2) = 7.3 * 10^{7} A^{4/3} E^5 \tag{2.31}$$

$$\lambda(E3) = 3.4 * A^2 E^7 \tag{2.32}$$

$$\lambda(E4) = 1.1 * 10^{-5} A^{8/3} E^9 \tag{2.33}$$

E1, E2, E3, E4 stand for multipole order transitions. Energy is scaled in MeV.

Similar formulas for magnetic transitions are [3] in units s^{-1}

$$\lambda(M1) = 5.6 * 10^{13} E^3 \tag{2.34}$$

$$\lambda(M2) = 3.5 * 10^{7} A^{2/3} E^5 \tag{2.35}$$

$$\lambda(M3) = 16 * A^{4/3} E^7 \tag{2.36}$$

$$\lambda(M4) = 4.5 * 10^{-6} A^2 E^9 \tag{2.37}$$

These estimations are known in the literature as *Weisskopf estimates* [3], [34] Although these are not precise theoretical calculations for the actual probabilities they provide a very good and quick approximation for the rates of gamma transitions solely based on energy and atomic number. Also as can be seen from the general form of the formulas the lower multipoles are dominant. Increasing the order of multipole by one reduces the probability by a factor 10^{-5}. For a given multipole order electric transitions are more likely to occur than magnetic ones. For the case of ^{35}Ar for energies just above S_p M1 and E2 are the only significant contributors to gamma decay with the former approximately two orders of magnitude larger than the latter.

The type of emitted radiation, magnetic or electric, is determined by the parities of the initial and final state. If there is no change in parity the radiation field must have even parity and if the parity is changed then radiation field must have odd parity. From the previously written expression for parities of electric and magnetic transitions and conservation of angular momentum, it is possible to summarize selection rules for gamma transitions in the nuclei:

$$\left|I_i - I_f\right| \leq L \leq I_i + I_f \qquad (no\ L = 0)$$

$\Delta\pi = no$: even electric, odd magnetic

$\Delta\pi = yes$: odd electric, even magnetic

Where I_i, I_f stand for angular momentum of initial and final states correspondingly. There is an exception to this rule for the case $I_i = I_f$ because there is no monopole ($L = 0$) transitions. It is related to the fact that the spin of the photon is equal one and such transition is prohibited due angular momentum conservation. In classical electrodynamics monopole is just the electric charge and it does not change with time and under these conditions no electromagnetic radiation can be produced.

2.6 Thermonuclear reactions

While Q-value gives us the total amount of energy released in a particular reaction what is important in stellar environments is total energy liberated per unit volume. This will depend on two things: the nuclear cross section for a given reaction and the velocity distribution of interacting particles. The nuclear cross section is a measure of probability for a given reaction to occur. It is defined as follows [5]

$$\sigma \equiv \frac{\left(\frac{N_r}{t}\right)}{\left[\frac{N_b}{tA}\right]N_t}, \tag{2.38}$$

where N_r/t the total number of interactions that occur per unit time, $\frac{N_b}{tA}$ the number of incident particles per unit area per unit time, and N_t is the number of non-overlapping target particles within the beam. Using the above equation we can write the rate of a nuclear reaction (per unit time t and unit volume V) as

$$\frac{N_r}{Vt} = (\sigma N_t)\left(\frac{N_b}{VAt}\right) = \sigma \frac{N_t}{V}\frac{N_b}{At} = \sigma \frac{N_t}{V} v \frac{N_b}{V}, \tag{2.39}$$

where v is the velocity of incident particles. If we consider a reaction $0 + 1 \rightarrow 2 + 3$ where 0 is a projectile and 1 is a target the reaction rate for this reaction can be written as $r_{01} \equiv N_r/(Vt)$ or using previous expression

$$r_{01} = N_0 N_1 v\sigma, \tag{2.40}$$

Here $N_0 \equiv N_t/V$ and $N_1 \equiv N_b/V$ are the number densities for the interacting particles. The value of σ cross section in general may have velocity dependence. In stellar plasma relative

velocities are not constant and they have certain distribution that is described by probability function $P(v)$. So $P(v)dv$ gives the probability of the relative velocity of interacting particles to be between v and $v+dv$. As a probability distribution function it satisfies normalization condition $\int_0^\infty P(v)dv = 1$. Finally using the probability distribution function the reaction rate can be written more general as [3], [5]

$$r_{01} = N_0 N_1 \int_0^\infty vP(v)\sigma(v)dv \equiv N_0 N_1 \langle \sigma v \rangle_{01}. \tag{2.41}$$

Here $\langle \sigma v \rangle_{01}$ is the reaction rate per pair.Another aspect of thermonuclear reactions one needs to consider is the temperature. Matter in most stellar environments where thermonuclear reactions take place is non-degenerate and non-relativistic. Therefore in most cases the velocities of the nuclei can be accurately described by a Maxwell-Boltzmann distribution

$$P(v)dv = \left(\frac{m_{01}}{2\pi kT}\right)^{3/2} e^{-\frac{m_{01}v^2}{2kT}} 4\pi v^2 dv, \tag{2.42}$$

This gives the probability that a given nuclei has a velocity in the interval between v and $v+dv$. In the equation (2.42) m_{01} is a reduced of the two interacting particles and v is their relative velocity. This distribution can be rewritten using energy as a variable.

$$P(E)dE = \frac{2}{\sqrt{\pi}} \frac{1}{(kT)^{3/2}} \sqrt{E} e^{-E/kT} dE. \tag{2.43}$$

The factor $(kT)^{-3/2}\sqrt{E}e^{-E/kT}$ that appears in such distribution (2.43) has its importance in the reaction rate in stellar environments like Novae along with Gamow factor that will be discussed later.

2.7 Gamma induced reactions

If we replace 2 with a photon in the previously considered case then $\gamma + 3 \rightarrow 0 + 1$ [5] is called a photodisintegration reaction. Using the analogy from the previous chapter one can write the reaction rate for the photodisintegration as following [5]

$$r_{\gamma 3} = N_3 N_\gamma c\sigma\left(E_\gamma\right), \tag{2.44}$$

where $N_3 \equiv N_t/V$, $N_\gamma \equiv N_b/V$, c – speed of light. The probability of decay per nucleus per second for this process is given by [36]

$$\lambda_\gamma = \frac{8\pi}{h^3c^2}\int_0^\infty \frac{E_\gamma^2}{e^{\frac{E_\gamma}{kT}}-1}\sigma(E_\gamma)dE_\gamma. \tag{2.45}$$

It is worth mentioning that since most of the photodisintegration reactions are endothermic the lower integration limit is given by the threshold energy of the given reaction. It is interesting to note that (2.45) does not depend on stellar density.

2.8 Non resonant thermonuclear reactions

The general expression for a particle-induced reaction rate is given by [5]

$$N_A\langle\sigma v\rangle = \left(\frac{8}{\pi m_{01}}\right)^{\frac{1}{2}}\frac{N_A}{(kT)^{3/2}}\int_0^\infty E\sigma(E)e^{-E/kT}\,dE. \tag{2.46}$$

Here $m_{01} = m_0m_1/(m_0+m_1)$ is the reduced mass of interacting particles, $\sigma(E)$ is the reaction cross section. The given rate is in the units of $[cm^3\,mol^{-1}s^{-1}]$. Here in equation (2.46), N_A was added to normalize the reaction rate per mol^{-1}. If the cross section is known the integral in eq. (2.46) can be solved either analytically or numerically.

For non-resonant nuclear reactions cross-section changes smoothly with time but decreases by several orders of magnitude for smaller energies due to reduction in transmission probability through coulomb barrier ($l = 0$ case). Cross section for non-resonant reactions can be written using the astrophysical S-factor:

$$\sigma(E) \equiv \frac{1}{E}e^{-2\pi\eta}S(E). \tag{2.47}$$

Here the factor $e^{-2\pi\eta}$ factor arises from the solution to the problem about transmission through the Coulomb barrier. The definition (2.47) essentially separates $1/E$ dependence of nuclear cross section and Coulomb barrier transmission probability, making the value of $S(E)$

weakly varying with energy. The factor in the exponent is $2\pi\eta = 0.9895 Z_0 Z_1 \sqrt{\frac{M_0 M_1}{M_0+M_1}} \sqrt{\frac{1}{E}}$. Where M_i and E are in units of [u] and [MeV] respectively.

$$e^{-2\pi\eta} \equiv \exp\left(-\frac{2\pi}{\hbar}\sqrt{\frac{m}{2E} Z_0 Z_1 e^2}\right). \tag{2.48}$$

This definition makes the $S(E)$ value much less dependent on energy than nuclear cross section. After plugging equations (2.47) and (2.48) into (2.46) one can get the final expression for the non-resonant reaction rate

$$N_A\langle\sigma v\rangle = \left(\frac{8}{\pi m_{01}}\right)^{1/2} \frac{N_A}{(kT)^{3/2}} \int_0^\infty \exp\left(-\frac{2\pi}{\hbar}\sqrt{\frac{m_{01}}{2E}} Z_0 Z_1 e^2\right) S(E)\, e^{-E/kT} dE. \tag{2.49}$$

Here N_A is Avogadro constant, m_{01} – the reduced mass of two nuclei, Z_0 and Z_1 are charges of target and projectile. If we consider the case where $S(E)$ is constant then it can be moved out of the integrand. The factor $e^{-E/kT}$ has its origin from Maxwell-Boltzman distribution and it goes to zero as energy goes to infinity. The term in the equation (2.48) presents the Gamow factor. One can see that for a given pair of nuclei with charges Z_0 and Z_1 the Gamow factor will only depend on energy. Therefore the actual dependence on energy has a form $e^{-1/\sqrt{E}}$ and it approaches zero as energy becomes very small. Therefore the maximum contribution to the integral will come from the energy that maximizes the multiplication of the two terms. One can easily calculate the position of Gamow peak by taking the derivative from the integrand and then setting $E = E_0$. It can be shown that the position of the Gamow peak is given by [5]

$$E_0 = 0.122\left(Z_0^2 Z_1^2 \frac{M_0 M_1}{M_0+M_1} T_9^2\right)^{1/3}. \tag{2.50}$$

Where masses are given in the atomic units of u and energy is in MeV and temperature in GK. It is possible to approximate the Gamow peak by a Gaussian function and calculate the width of the peak Δ that is calculated at 1/e height of the approximation function [5]. The expression of the width is given (in MeV units) by

$$\Delta = \frac{4}{\sqrt{3}}\sqrt{E_0 kT} = 0.2368\left(Z_0^2 Z_1^2 \frac{M_0 M_1}{M_0+M_1} T_9^5\right)^{1/6}. \tag{2.51}$$

Using equations (48) and (49) for typical Novae temperature of 0.4 GK and the reaction ^{34}Cl+p the Gamow peak will be located at around 433 keV and the width of 280 keV.

2.9 Resonant thermonuclear reactions

An isolated resonance can be described by the Breit-Wigner formula [3],[5]

$$\sigma_{BW}(E) = \frac{\lambda^2}{4\pi}\frac{(2J+1)(1+\delta_{01})}{(2j_0+1)(2j_1+1)}\frac{\Gamma_\gamma\Gamma_p}{(E_r-E)^2+\Gamma^2/4}, \tag{2.52}$$

where E_r and J are energy and the spin of the resonance, Γ_γ and Γ_p are partial widths of the gamma and proton decay channel, Γ is the total resonance width, j_0 and j_1 are the spins of the target and the projectile, δ_{01} is Kronecker delta. Using the above definition of the cross section the reaction rate for a single resonance can be written as

$$N_A\langle\sigma v\rangle = \left(\frac{8}{\pi m_{01}}\right)^{1/2}\frac{N_A}{(kT)^{3/2}}\int_0^\infty E\sigma_{BW}e^{-E/kT}\,dE. \tag{2.53}$$

After plugging the expression (2.52) into the integral (2.53) one can get an explicit relation for the reaction rate. It is possible to calculate the integral in equation (2.53) because for a narrow resonance the value of E stays approximately constant. The expression for $N_A\langle\sigma v\rangle$ is then given by [5]

$$N_A\langle\sigma v\rangle = N_A\left(\frac{2\pi}{m_{01}kT}\right)^{3/2}\hbar^2 e^{-E_r/kT}\omega\gamma. \tag{2.54}$$

where $\omega\gamma \equiv \frac{(2J+1)(1+\delta_{01})}{(2j_0+1)(2j_1+1)}\frac{\Gamma_\gamma\Gamma_p}{\Gamma_\gamma+\Gamma_p}$ is proportional to the area under the peak resonance and called the resonance strength. If more than one resonance contributes to the cross section then they have to be summed up, giving a numerical expression

$$N_A\langle\sigma v\rangle = \frac{1.5399*10^{11}}{\left(\frac{M_0M_1}{M_0+M_1}T_9\right)^{3/2}}\sum_i(\omega\gamma)_i e^{-11.605E_i/T_9}. \tag{2.55}$$

The expression is in ($cm^3mol^{-1}s^{-1}$) units. E_i and $(\omega\gamma)_i$ are given in MeV and all masses depend on the energy and the resonance strength but not the exact shape of the resonance. From expression (2.53) it is obvious that the reaction will be dominated by those resonances located

in the Gamow window, since σ_{BW} will give a major contribution to the integral, while the $E * e^{-E/kT}$ factor will be getting smaller as energy grows. Therefore locating resonances in the region a few hundred keV is important, as they are going to be major contributors to the overall reaction rate. In the formula (2.55) the resonance strength is the one that requires more elaboration. It can be rewritten as

$$\omega\gamma = \omega \frac{\Gamma_p \Gamma_\gamma}{\Gamma_p + \Gamma_\gamma} . \tag{2.56}$$

For the case of $\Gamma_p \ll \Gamma_\gamma$ (that is normally true for a low lying resonance) Γ_γ cancels out and the expression (2.56) only depends on the proton width Γ_p. The proton width can be calculated from the width of single-particle state multiplied by the spectroscopic factor [1]

$$\Gamma_p = 2 \frac{\hbar^2}{mR^2} P_c * C^2S * \theta^2_{pc,} \tag{2.57}$$

where P_c is the penetration factor or probability that a proton can penetrate the Coulomb barrier and angular momentum barrier, $\theta^2_{pc} = \frac{R}{2}\left|u_{pc}(R)\right|^2$ is the dimensionless single-particle reduced width, and C^2S is a spectroscopic factor. The value u_{pc} stands for single-particle eigenfunction. The spectroscopic factor is a physical measure of how closely the wave-functions of a single-particle state and an actual state overlap.

3. EXPERIMENTAL SETUP

3.1 Overview of cyclotron facility

The experimental work in this dissertation, along with data analysis, was planned and completed at the Cyclotron Institute at Texas A&M University. The K-150 cyclotron was initially commissioned in 1967 and was used till mid 1985 when a new K-500 [40] superconducting cyclotron was built. The original cyclotron was refurbished and recommissioned in 2012. The way the two accelerators are setup allows simultaneous experiments performed on both as long as they use different beam lines that do not intersect. The work for this Ph.D. thesis was done with the K-500 cyclotron, which can provide beam energies ranging from light nuclei to the heavy ones for protons from 8 MeV/A to 70 MeV/A and uranium between 2 MeV/A to 15 MeV/A. The main magnet of the K-500 uses a coil wire made of superconducting material (niobium-titanium) that can run an electric current up to 800 A. This allows creating a magnetic field of 50 kilogauss. A cyclotron type of accelerator was invented by E. O. Lawrence in 1934 [41] and is widely used today in the field of nuclear physics for accelerating heavy ion beams. The operating principle of the cyclotron is based on using hollow "D"-shaped elements that are working as electrodes that have electric fields $\boldsymbol{E}$ between them. As ions are injected into the center of the "D", a magnetic field $\boldsymbol{B}$ that is perpendicular to the plane where particles rotate, keeps them in the circular orbit. Every time the particle passes the gap between the "D's" it gets an additional acceleration from the electric field $\boldsymbol{E}$. As a result the ions will cycle inside the "Dees" until their trajectory reaches the outer boundary of the magnets where they get deflected into a beamline. The maximum energy that can be achieved in cyclotron type accelerators (non-relativistic case) can be obtained by equating the centripetal force $F_c = \frac{mv^2}{r}$ and Lorentz force $F_b = qvB$ where m stands for mass of the particle, q is the charge and $B -$ magnetic field. The velocity v is given by as $v = \frac{qBR}{m}$ and R stands for the radius of the dee. Therefore the energy can be written as

$$E = \frac{1}{2}mv^2 = \frac{q^2B^2R^2}{2m}. \tag{3.1}$$

As it can be seen from (3.1) the major limitations on the energy that can be achieved by a cyclotron come from the strength of the magnetic field B and radius of the magnet R as well as the charge state q.

The K-500 uses an ECR ion source [42], which uses the principle of electron cyclotron resonance to produce an ionized plasma. For the present work two types of ions were used for producing beam: ^{28}Si and ^{36}Ar with the charge states of 10^{+} and 13^{+} coming out of the K-500. These two species of nuclei were injected from the ECR source into the K-500 cyclotron producing primary beams at 36 MeV/A (for both) that were used for the calibration and measurement, correspondingly. The basic layout of the cyclotron facility is shown in Fig. 3.1. While having multiple elements and beamlines optimized for a specific type of experiment the entire work of this thesis was performed on MARS (Momentum Achromat Recoil Separator), which was designed to produce secondary radioactive beams.

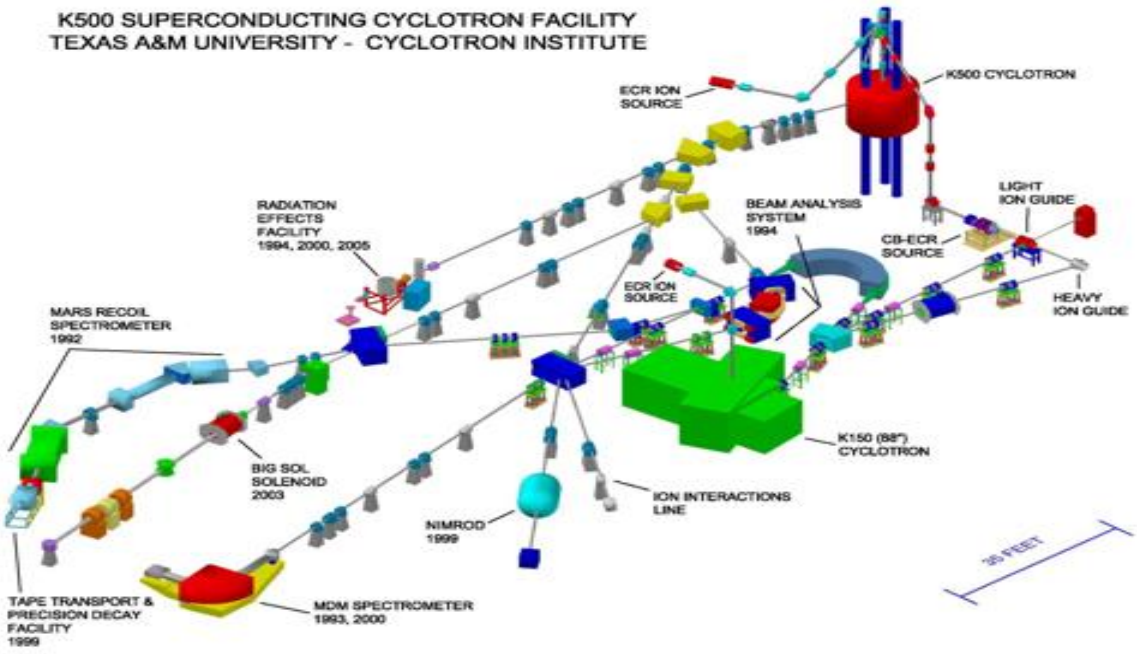

Figure 3. 1: Cyclotron Institute layout

3.2 MARS

Use of the indirect technique for populating relevant states from the astrophysical point of view often requires a radioactive beam. MARS was designed and built for this purpose [43] [44]. Studies in the field of nuclear astrophysics often require production of exotic beams away from stability, since a lot of processes that take place in the stellar environments (X-ray burst, Novae explosions) involve unstable nuclei. Also due to short half-lives it is practically impossible to create targets from these nuclei. MARS can be used for producing radioactive beams, which can be used for studying the excited states and properties of proton and neutron rich nuclei. The schematic of MARS layout is presented in Fig. 3.2 below.

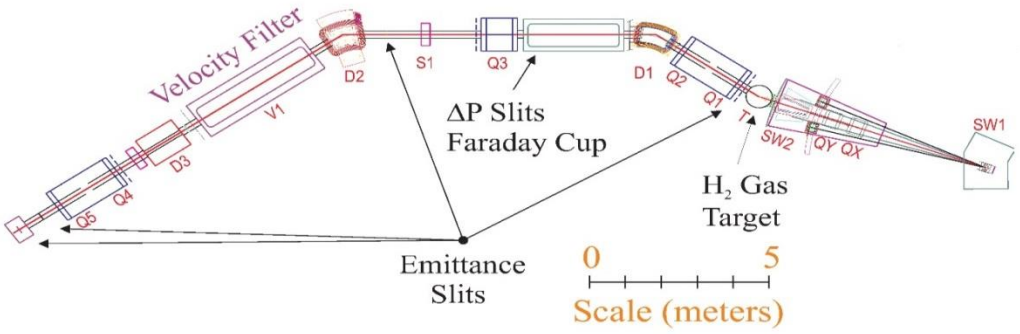

Figure 3. 2: Schematic of MARS

The design of MARS was optimized for use over a wide energy range along with good mass resolution. Radioactive beams can be made in the range of scattering angles from 0^0 to 30^0. However for the present work MARS was always set at 0^0. Operation at 0^0 allows for good efficiency using inverse kinematics reactions, which are typically used in the experiments with a target consisting of light nuclei and a heavy ion beam.

The optics that was developed for MARS uses two dispersing planes. The dipole magnet D1 (Fig 3.2) provides a p/q dispersion in the horizontal direction. The concept of magnetic rigidity uses the fact that when the centripetal force is equal to the Lorentz force one can extract the useful relation $B\rho = p/q$ where B is the magnetic field, and ρ is the radius of the trajectory inside the D1 magnet. The quadrupoles Q1, Q2, Q3 and the dipoles D1, D2 deliver an achromatic beam into the velocity filter. The velocity filter in turn provides vertical dispersion of the beam. Inside the velocity filter there are magnetic and electric fields that are perpendicular to one another. As a result only those ions that have the Lorentz force equal to the electrostatic force are passed through the velocity filter unaffected ($v = \frac{|E|}{|B|}$). After that the beam is bent by the D3 dipole and finally focused by the quadrupoles Q4, Q5 to form an M/Q focal plane. Another important part of MARS is a chamber located after the D1 dipole magnet. Inside the chamber there is a Faraday cup which is used to monitor the beam intensity. Right after the D1 magnet the beam enters a chamber, where the beam is buried hence the name - coffin. Most of the primary beam passes through the target chamber without reacting with the target nuclei and it eventually is caught by the Faraday cup inside the coffin.

The primary beams used in the production of $^{25}Si^{14+}$ and $^{35}K^{19+}$ were $^{28}Si^{10+}$ and $^{36}Ar^{13+}$ coming out of the cyclotron at 36 MeV/A (energy per one nucleon). ^{25}Si was used for calibration and required a different production method compared to ^{35}K production. An aluminum solid target was used to produce ^{25}Si. There was a target ladder installed inside the target chamber with three different aluminum target thicknesses - 15.6 mil (396 μm), 11 mil (279 μm), 10 mil (254μm). The set of targets is used in case the correction to the energy of the secondary beam is needed. The same chamber can also host gaseous targets in a gas cell, but for the production of ^{25}Si the gas cell was removed and a ladder with aluminum targets was installed. For the given experiment an 11 mil (279 μm) target was used. After the calibration is finished the target is changed for hydrogen gas, H_2 that is used in the production of ^{35}K secondary beam. The gas is cooled to LN_2 temperature (77 K). The gas cell inside the target chamber has windows for beam entrance and beam and secondary particles exit that are 0.75'' in diameter and made of 0.16 mil (4 μm) havar. The target chamber utilized a magnetic stirrer inside to maintain uniform pressure in the gaseous target as it can have local pressure gradient along the path of the

beam. Initial tuning for the production of ^{25}Si was done with guidance from the program LISE++ [45], which gives starting values for every magnet. These values are then dialed into MARS for fine tuning with the actual secondary beam.

To control the tuning process, a ΔE-E telescope of silicon detectors was placed at the end of MARS. Also colloquially referred to as the target detector, it uses 1000 μm (for a present experiment) thick silicon strip detector model X1 [46] from Micron Semiconductor, which gives a ΔE measurement. It utilizes 16 strips on the front. The strip has a size 3.00mm x 50.00mm and has readout along two ends of the strip to get the position measurement along the strip. Because of relatively small size of the beam spot only the central six strips are normally used for beam tuning. The back of the telescope uses a 500 μm E (internal number 6) plate produced by Micron Semiconductor model MSX25 [47] that gives an $E_{residual}$ measurement. It has a size 50 mm x 50 mm. The back of the ΔE detector was biased at +150 V and the E plate was biased at -70 V.

The tuning process starts with closing the coffin slits, which serve as the viewer there. It has a special phosphorescent coating that produces light when the beam hits it. If the values for the D1 magnet are correct the beam spot should be visible in the center of the viewer. During this process, the beam can be checked to verify it is entering MARS at 0 degrees. After performing the position check of the beam spot the target detector gets connected to the electronics (Fig. 3.3) and the beam reaction products are sent through the rest of MARS by changing the current in the D1-D2 magnets.

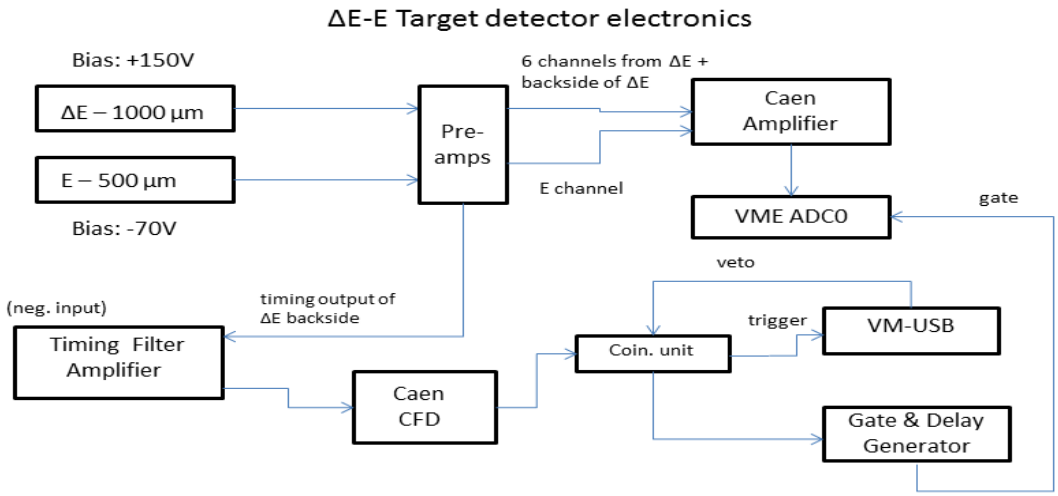

Figure 3. 3: The target detector electronics setup

It is worth mentioning that even though both ΔE and E are biased, for these studies the primary secondary beam was fully stopped in the ΔE strip detector.

The next step is to connect the Faraday Cup (FC) that is located in the coffin. MARS actually utilizes two FCs located on the left and right side of the beam. The choice of which one is used depends of the rigidity of the primary beam compared to the reaction products. In the present experiment the right FC, from the beam direction perspective, was used. The next step is to check the position of the FC relative to the beam. This is done by moving the FC in the coffin along the z-axis (beam travel) and observing the current. After that the coffin slits are opened along with the valve in the velocity filter. An important step one needs to do is a position calibration of the target detector. It is done with the 4^{th} slits. They are located right before the target detector and for the purpose of the position calibration were closed at three different positions in the y-direction (vertical) +4, 0 -6 mm. The zero level corresponds to the center on

the y axis. The other two positions give reference points at the y axis at positive 4mm and negative 6mm. The gap between the slits at each position is approximately 0.1 mm. After determining the positions of the centroids created by the secondary beam from three different slit positions, the calibration can be established for every strip.

Once the calibration is done it becomes possible to do particle identification. This process not only involves identification but optimization of the production of the secondary beam. The D3 magnet is used to steer the beam of interest exactly into the center of the target detector. Next is to optimize the settings for the D1-D2 dipoles. The secondary beam comes in a wide acceptance angle and by the manipulation the D1-D2 magnets one can optimize the production for the desired isotope in the cocktail of different species. The final phase includes optimization of the quadrupoles and velocity filter (if necessary). After all magnets are set the last ("fourth") slits are closed to limit the acceptance angle so that only isotopes with the same mass to charge ratio can make it to the AstroBoxII.

3.3 The AstroBoxII

The AstroBoxII is an update of the original AstroBox detector [48], which was specially designed to measure low energy protons emitted after beta decay. The AstroBoxII is a gas detector and the ions of interest are stopped inside of it [49]. As the ions create electrons the drift field inside the detector pushes them towards the sensitive element of the detector – the Micromegas. The Micromegas (Micro-mesh-gaseous Structure) is the main element of the detector [50]. The AstroBoxII is a two-stage avalanche chamber. In the first stage the electrons are driven by the cathode towards the micromesh, and in the second phase the electric field between the mesh and anode pads creates an avalanche proportional to the ionization in the first stage. The strength of the electric field in the amplification region (128 μm) is ~ 30 kV/cm. The Micromegas that were manufactured for the AstroBoxII have a structure divided into 29 rectangular-shape pads. Each has an individual readout that is fed into a MPR16-100 preamplifier. The total active region of the AstroBoxII is 100 mm x 145mm. The general schematic of the detector is presented in the picture below Fig. 3.4

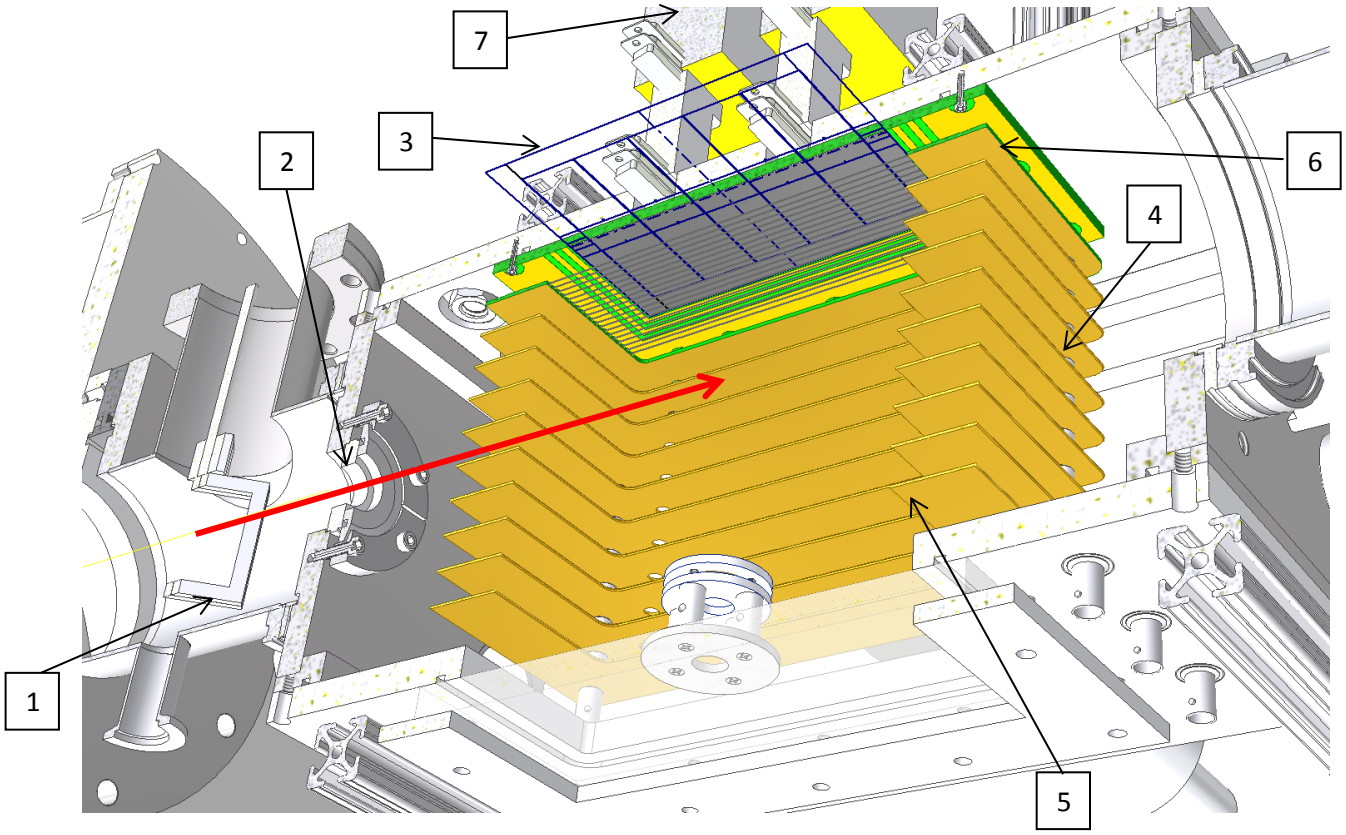

Figure 3. 4: The AstroBoxII schematic [51]. The red arrow shows the direction of the beam travel. (1) Degrader frame. (2) Entrance window. (3) Micromegas. (4) Equipotential rings for uniform drifting field. (5) Cathode. (6) Gating Grid. (7) MPR-16 preamplifiers.

The red arrow shows the direction of the beam travel. An aluminum degrader is installed in the frame (1). An aramica window (2) (50 µm) is used to isolate the gas mixture of the AstroBoxII from the vacuum of the beamline. The Micromegas plate with the pads (3) is located above the beam and faces downwards. A drift field is created by the cathode (5) at -3.3 kV giving the strength of the electric drifting field ~ 200 V/cm and its uniformity is maintained by the sets of equipotential rings (4). These rings are made of copper and have a thickness 1 mm. There are ten rings that are spaced 14.2 mm apart from each other. The uniformity of the rings is realized

by the resistor chain (8 resistors) with every resistor at 8.9 MΩ that steps down the negative potential on each ring in a direction from the cathode to the Micromegas. The ninth ring is actually a pc board that is 1.6 mm thick and hosts the set of gating grid (GG) wires. To ensure the uniformity of the electric field both sides of the gating grid pc board are connected by a 1.43×10^6 ohm resistor. The gating grid (6) controls the transparency of the field upward for drifting electrons. It has a negative polarity (-330 V) during a beam-off phase and helps push the drifting electrons towards the Micromegas. During a beam-on period it has a positive polarity +38 V (can be adjusted if needed) that inhibits the drift of electrons towards the Micromegas, for the reasons that are explained below. In the Fig. 3.5 the operational principle of the AstroBoxII is explained.

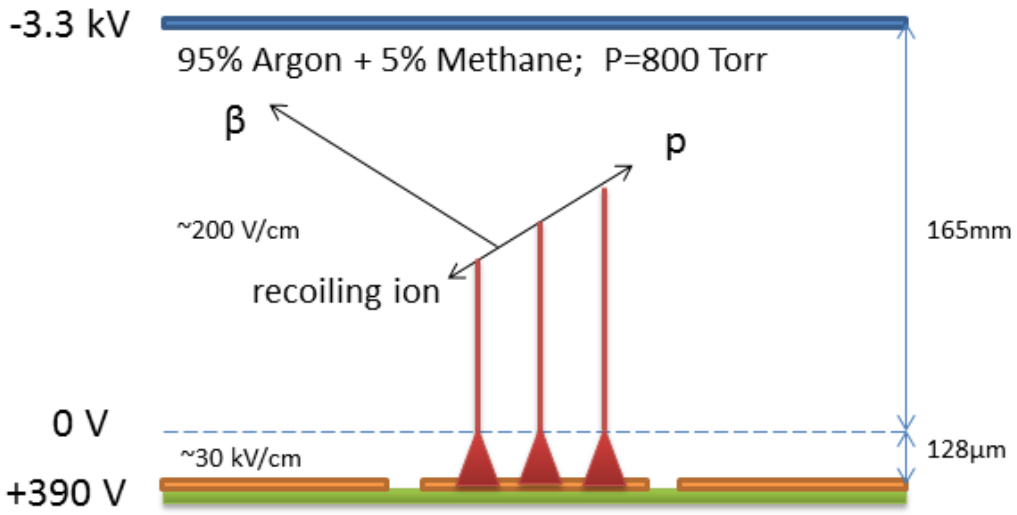

Figure 3. 5: Basic principle of operation of the AstroBoxII

The detector in the present experiment used P-5 gas (mixture 95% argon + 5% methane) with a pressure of 800 Torr. The gas pressure is regulated by the gas regulating system, which

refreshes the gas inside the AstroBoxII while maintaining stable pressure. The flow was of the order 0.3 ft^3/h (or 11.32 L/h) for air (as the flowing gauge was calibrated by the manufacturer for air) for the gas handling system used in the October experiment. The signal from the pads is read by a pair of Mesytec MPR16-100 16-channel preamplifiers along with Mesytec MSCF-16 shapers (with built-in discriminators).

The total energy loss inside the sensitive volume of the detector during the implantation phase can be very high (>50 MeV). However the dynamic range used for proton measurements is between 40-1600 keV. This means that the amplification used for the measurements (beam-off) will be too high for the implantation phase and as a result some spark damage can occur during the implantation (beam-on). Due to the nature of the delayed proton measurements one needs to first implant nuclei inside the AstroBoxII and then measure the decay. During the beam-on period (also referred to as implantation) the GG voltage was such that it inhibited the drift of electrons towards the anode. However it is still possible to measure the change in energy loss (not calibrated) during the implantation phase. In fact during the beam-on period adjustments to the implantation spot are made by rotating the aluminum degrader and changing the effective thickness of the material the beam has to go through. After the beam was implanted the voltage on the GG was switched again making it transparent for the drifting electrons. The latter mode is called the beam-off period (also referred as the measurement). A special device was built in-house by Matthew McCleskey to control the voltages during the beam-on and beam-off period, as described below.

The layout of the measuring pads in the AstroBoxII is shown in Fig. 3.6.

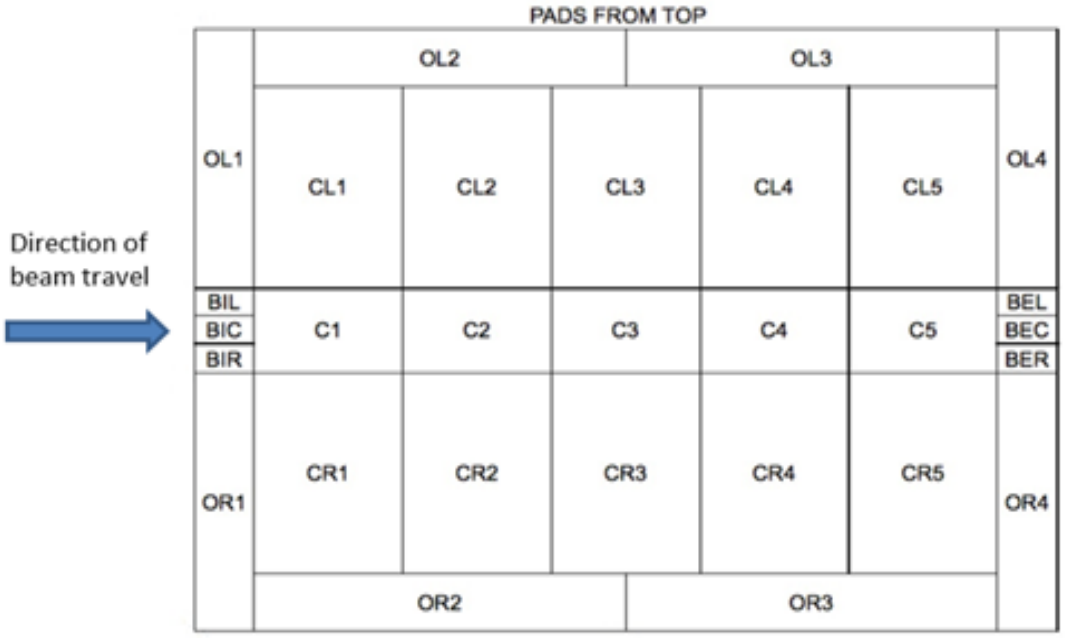

Figure 3. 6: General layout of the AstroBoxII pads. The beam is traveling over the central pads from the left to the right as seen in the picture [51].

The Micromegas used in the experiment had a 128 µm gap, but the design of the AstroBoxII allows quick replacement of the Micromegas with different thicknesses. The AstroBoxII efficiency was estimated using code GEANT4 [52]. For the simulation the pressure was set to 800 Torr and the temperature to 293K. The simulations were done for the central pad C3, but they will hold for the other pads as well as they have the same geometry. The efficiency was estimated both for protons and alpha particles. The number of simulated events for a given energy was set at 10000 and the energy range was chosen between 100 keV to 2500 keV. As an example, the simulation for proton efficiency is shown in the Fig 3.7 [51].

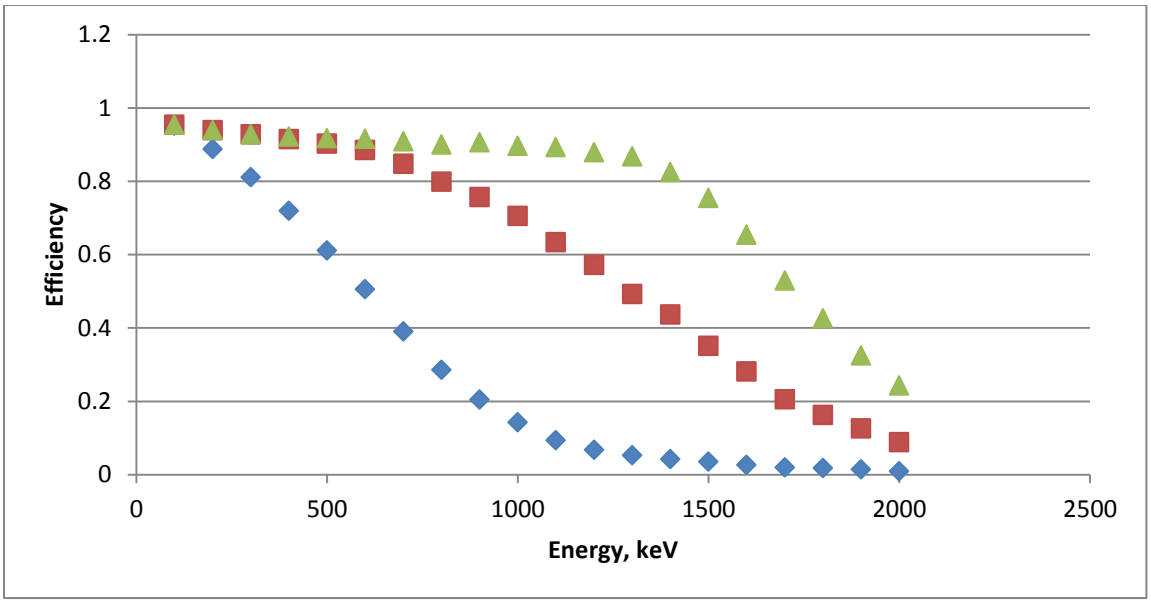

Figure 3. 7: Efficiency of proton detection in AstroBoxII. The blue dots represent the multiplicity m1, the red dots combined multiplicities m1+m2, the green dots combined multiplicities m1+m2+m3.

This particular case was simulated for the multiplicity of events with combined efficiency from multiplicity 1, 1+2, and 1+2+3. Events that trigger one pad at the moment are called multiplicity one, those that trigger two pads at the same time multiplicity two, and those that trigger three pads are multiplicity three.

The detailed schematic of the electronics used in the experiment is presented in the figure below.

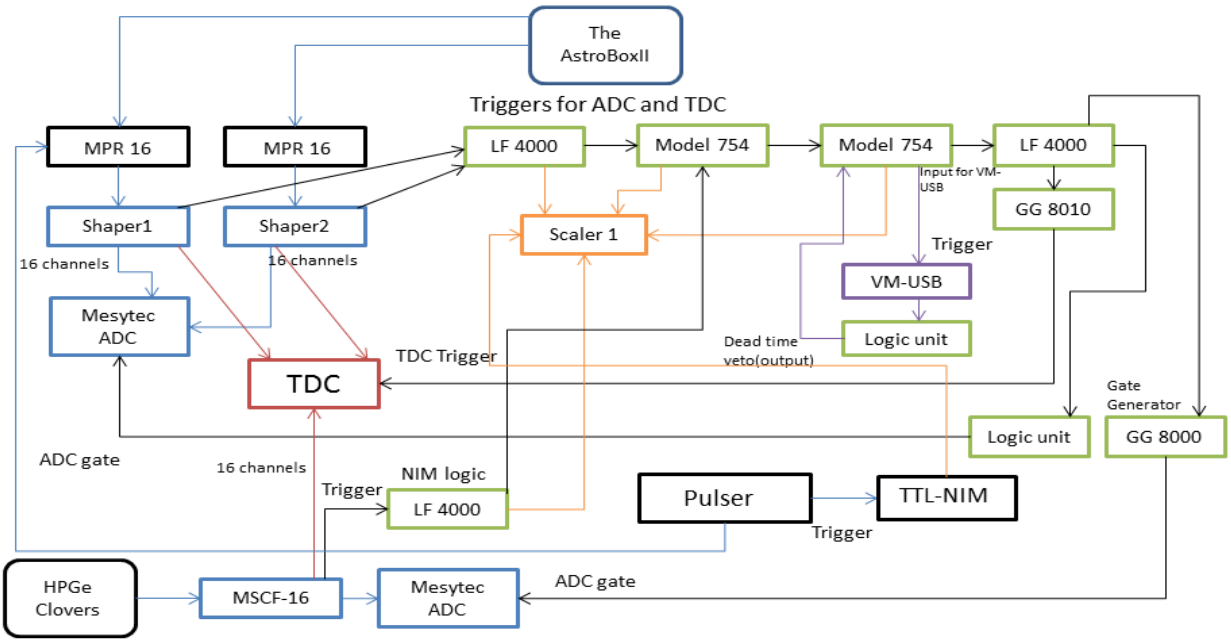

Figure 3. 8: Electronics schematic for the AstroBoxII setup.

The signals created in the Micromegas are fed to the 16 channel MPR-16 Mesytec preamplifiers [53]. After that they are processed by 16 channel shaping/timing filter amplifiers Mesytec MSCF-16 [54] (shaper1, shaper2), which also have Constant Fraction Discriminator (CFD) modules built-in. The gain for the shapers can be adjusted in 16 steps with each step giving a 1.22 amplification factor. Additionally they had a coarse gain jumper set to 2. The modules provide a timing trigger output (NIM logic) for the data acquisition system. Also the system has a VM-USB that sends the data collected from the shapers to a hard drive. It also gives a veto signal during the dead time period, which is defined as the time during which the acquisition system is busy with processing a signal from the AstroBoxII and HPGe Clovers (see more details in the section 3.7). The data taken from HPGe Clovers were fed in the same data stack as the data from the AstroBoxII. The other data stack was self-triggered and read every 10 seconds. It was used for the recording of the pulses from Digital delay generator, which will be explained

below. It is important to notice that the Clovers were not triggering the acquisition system. The only time when gamma detectors are triggering the system is during the calibration of the detectors with multiple gamma sources.

3.4 The pulsing box

The pulsing box (Fig. 3.9) performs several important tasks during the experiment, including: controlling the duration of the beam-on (-off) periods during the implantation and the measurement periods respectively, zeroing the scaler2 (it counts the signals from Digital delay generator (see Fig. 3.10)) for having a correct time stamp, and a switching of the GG (Gating Grid) voltage during the beam-on (-off) phases.

Figure 3. 9: The pulsing box

There are several possibilities for the different setups with the pulsing box, but the one used for this work utilizes three: the “Move”, the “GG”, and “ISO OFF” signals. The electronic schematic that is used with the pulsing box is presented in the Fig. 3.10 below.

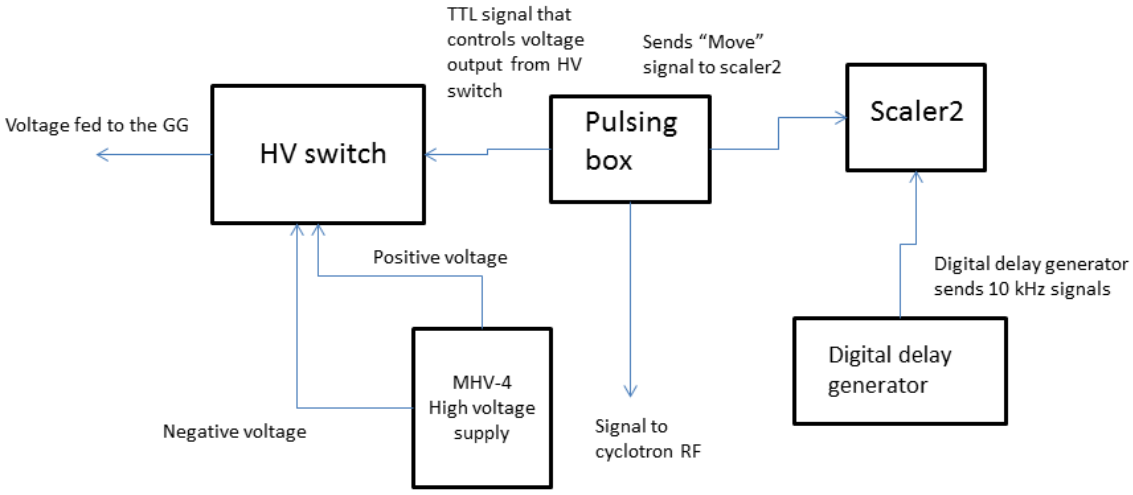

Figure 3. 10: Electronics setup for the pulsing box and switcher.

The important element of the setup that needs some explanation is the HV switch. It does switching of the output voltage for the GG while taking an input from the pulsing box. The HV switch can change the voltage between two preset values. In the case of ^{35}K, the switch was happening between +38 V to -330 V. The first voltage was corresponding to a beam-on period and the second one to a beam-off period. A Mesytec HV supply was providing both negative and positive voltages that were fed into the HV switch. One of elements of the setup in the Fig. 3.10 was the Digital delay generator that was sending signals at a constant rate 10 kHz. Scaler2 was counting the number of sent signals. Therefore the number of recorded signals will provide a time scale.

The schematic output of the pulsing box is presented in Fig. 3.11 [51].

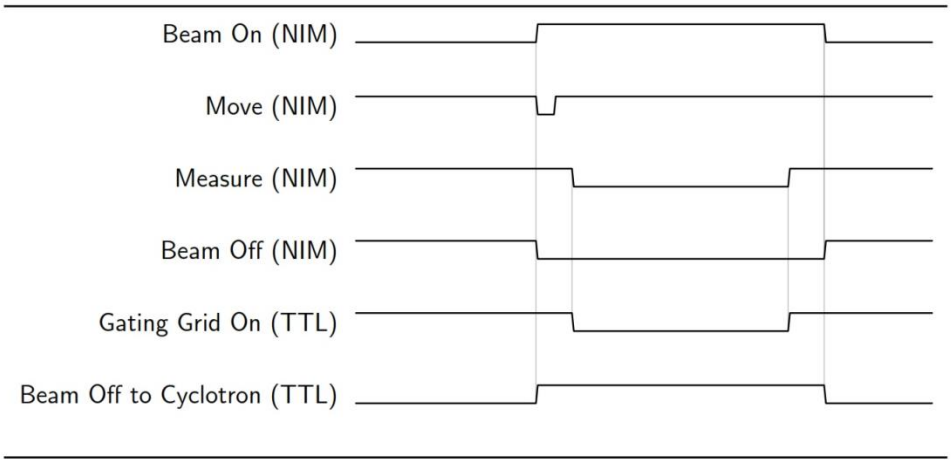

Figure 3. 11: Schematic output of the pulsing box. Three output signals were used in the present experiment “Move”, “Gating Grid On”, and “Beam Off to Cyclotron”. TTL signals have a positive +5 V logic signal (“True”), NIM signals have a negative -0.8 V (“True”) signal.

The output signals from the pulsing box were connected in the following way: the “Move” signal (Fig. 3.11) was hooked up to the Scaler2 and every time the “Move” is sent to the Scaler2 it zeroes it. The “Gating Grid On” was connected to the HV switch and the “Beam Off to Cyclotron” signal was sent to the K500 cyclotron RF. The “Move” has a negative NIM logic and the “Beam Off to Cyclotron” signal has a positive TTL logic. When the “Beam Off to Cyclotron signal” is sent to the cyclotron RF it shifts the phase between the dees and as a result the beam is not accelerated in the cyclotron during this period. Simultaneously the “Move” signal during much shorter amount of time sends a signal to the scaler2 and it zeroes the scaler2 during a relatively short amount of time (this time can be controlled). The next “Move” signal, which again zeroes the scaler2 will come after the “Beam on” period ends. It is important to notice that the Gating Grid will switch into “Beam off” with a slight delay when compared with the “Beam off” mode for the cyclotron. It is made this way for the safety of the detector because if

the cyclotron stays in the “Beam on” mode, but the GG is already switched to “Beam off” it can cause damage to the Micromegas. Similar logic is used when switching back to the “Beam on” mode: first the GG is switched and only after that the cyclotron. The delay is controlled from a program written in-house and in both cases for ^{25}Si and ^{35}K it was set at 5 ms for all measurements. The pulsing box time settings are shown in the Table 3.1

	^{25}Si (ms)	^{35}K (ms)	^{32}Cl (ms)
Implant (Beam On)	500	400	600
Move	5	5	5
Measure (Beam Off)	500	400	600
GG offset	5	5	5

Table 3. 1: Time settings for the pulsing box used for three different isotopes: ^{25}Si, ^{35}K, and ^{32}Cl.

3.5 Implantation phase

After initial focusing and production optimization is done with the target detector the next phase is to implant the secondary beam into the AstroBoxII. There are several reasons why one cannot just start measuring the decay of ^{35}K. The optics of the secondary beam in MARS is done in such way that if the beam spot is focused on the target detector it will start to diverge when going down along the axis of the beam travel. To assure adequate transmission on the AstroBoxII implantation, changes must be made to Q4 and Q5. Another reason is the positioning of the implantation inside the detector. For this purpose an aluminum degrader 13 mil (330.2 μm) thickness was used. This thickness was chosen based on a TRIM simulation. TRIM [34] is a special program that gives a Monte Carlo simulation of energy losses of heavy ions in different materials. The same degrader was utilized for both ^{25}S and ^{35}K beams. It was installed on a rotary mechanism that allows setting the required thickness along the beam travel path by altering the angle of the degrader. For ^{25}Si the degrader was set at 35.5^0, and for ^{35}K it was set at 24^0 degrees. These settings allow stopping the beam in the middle of the C3 pad. Normally the optimal spot to implant is right in the center of the C3 pad. The setting for the AstroBoxII must be set such that the Micromegas would not get damaged by sparks. In this phase the beam is not pulsed into the detector, but sent at the constant rate and essentially the AstroBoxII is in the "beam on" mode.

3.6 Calibration of the AstroBoxII

A beam of ^{25}Si was used to calibrate the AstroBoxII. For the calibration purposes three major proton lines were used, 401(1) keV, 555(11) keV, and 943(2) keV [55]. However one must be careful while measuring these energies, since the recoiling energy of ^{24}Mg will be on the order of few tens of keV. Some fraction of the energy of the heavy ion will be spent on excitation so as a result only some part of energy of the recoiling heavy ion will be spent on ionization. The corrected energy is calculated in the formula (3.2):

$$E_{obs} = E_p + E_{rec} * \alpha + E_{pos} \quad (3.2)$$

Here E_{obs} is the observed total ionization (measured by the AstroBoxII), E_p is the energy of the proton, E_{rec} is the energy of the recoiling heavy ion (^{24}Mg), α is the fraction of the energy of the recoiling ion that is spent on ionization, and E_{pos} is the average amount of energy deposited by a positron (from β-decay) in one pad (it was estimated to be around ~ 3 keV).

With the help of the code TRIM the observed total energies were calculated to be 392(1) keV, 542(11) keV, and 920(2) keV. After initial tuning was done with the target detector the following production rate was achieved: ^{25}Si at 1.24 event/nC, ^{27}P at 0.1 event/nC, and ^{23}Al at 0.04 event/nC. These numbers were calculated using a Faraday Cup integrator - 1000 pulses on the integrator correspond to a charge that equals to full scale used for reading the beam current multiplied by one second.

$$\frac{Event}{nC} = \frac{N_{event}}{\frac{N}{1000} * F.S. * 1s} \tag{3.3}$$

In formula (3.3) N_{event} is the number of nuclei counted, N is the number of pulses in the integrator, $F.S.$ is the full scaler used for the current reader. The figure below shows energy versus position on target detector. The most intense spot corresponds to ^{25}Si.

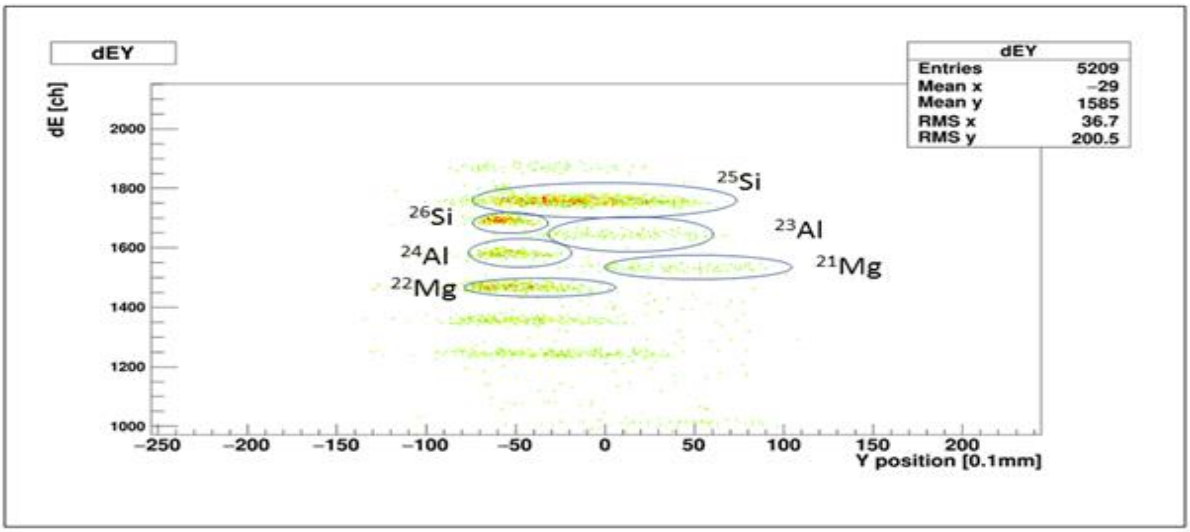

Figure 3. 12: ^{25}Si on the target detector. The quantity dEY represents the energy loss in the detector, which is plotted versus the vertical position given as the x-axis

As can be seen from the groups of events in Fig 3.12, there are more isotopes than just one that is entering the detector. However the extra groups have significantly smaller ΔE loss in the gas. As a result when implanting inside the AstroBoxII they will be not be fully stopped over the sensitive volume of the detector this was determined experimentally during the implantation phase. By looking at energy loss histograms inside the AstroBoxII only ^{25}Si was stopping inside the sensitive volume of the detector. Settings for the two Mesytec shapers were changed for the implantation phase, Fine Gain was set at 0 (FG=0) which corresponds to factor 1.22^0=1 (Coarse Gain=2), the GG voltage was set at -330 V (which makes the GG fully transparent), and the Micromegas (the anode) was set at +300 V. This voltage was chosen on the amplification dependence of anode voltage versus amplitude of the signal. The simulation proved to be fairly accurate with about one full pad length accuracy (see Fig. 3.13).

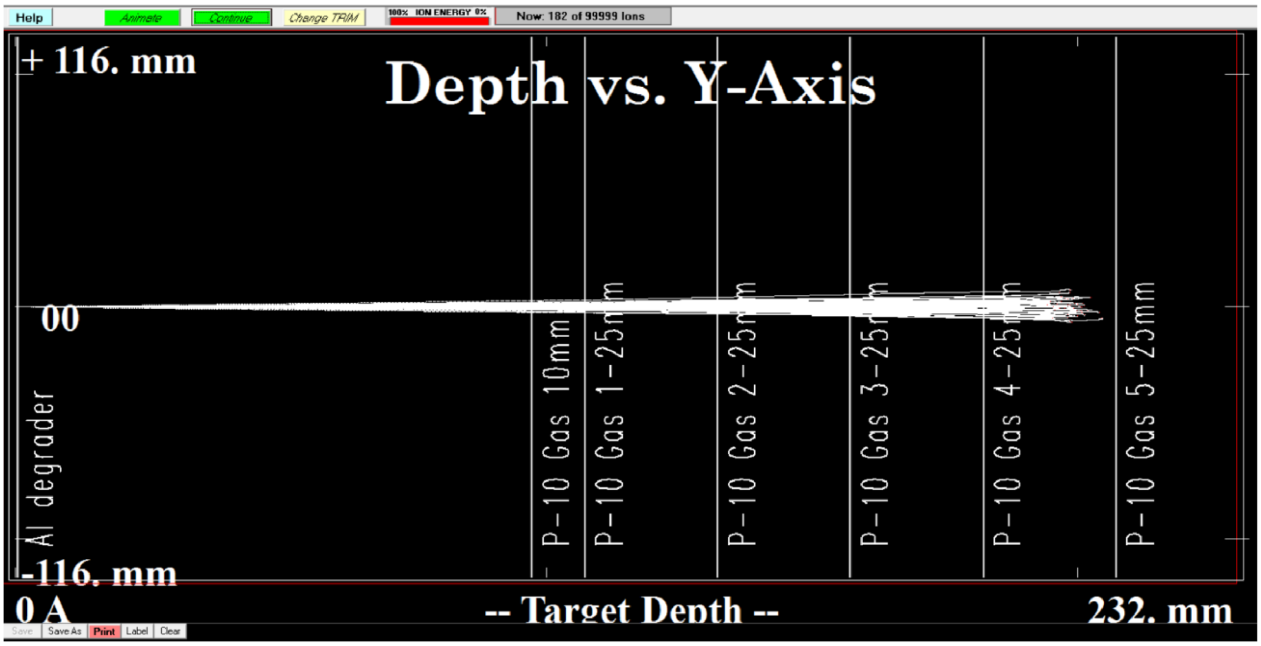

Figure 3. 13: Simulation (TRIM [56]) of stopping distances inside of the AstroBoxII. The degrader thickness was 13 mil (0.3302 mm). The angle was set at 35.5^0. It can be seen that the beam mostly stops in the C4 pad.

After trying several angles the final angle for the degrader was set at 35.5^0.

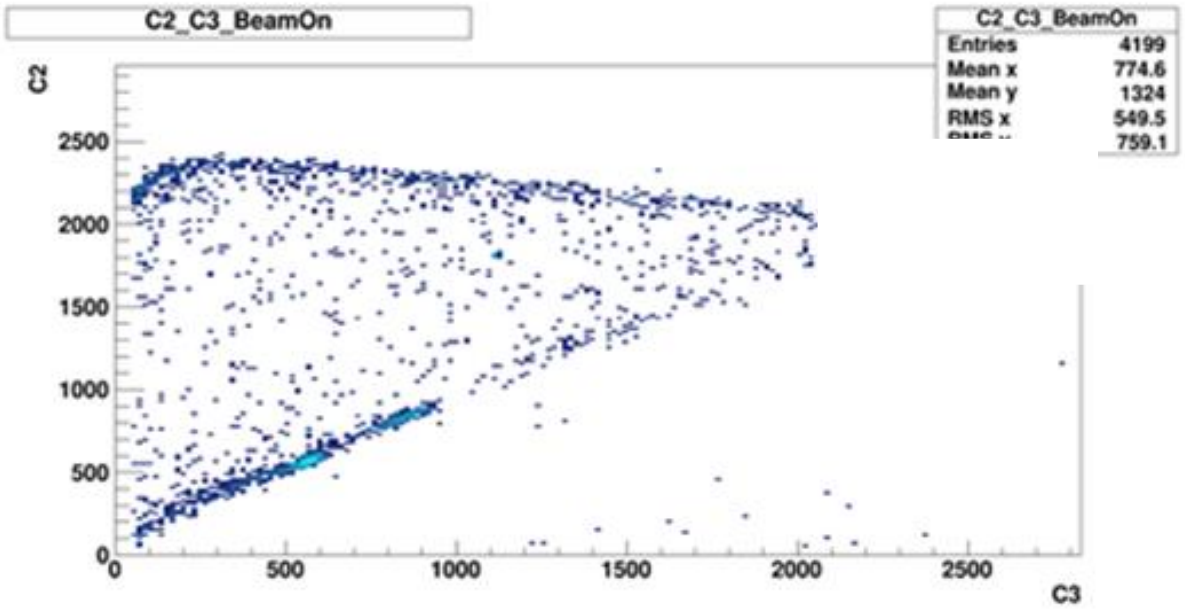

Figure 3. 14: ^{25}Si implantation phase in the AstroBoxII. On the x-axis energy loss over C3 pad and the y-axis energy loss in the C2 pad. The horizontal stripe between channels 2000-2500 corresponds to ^{25}Si. Colors represent different intensities. The angle was 35.5^0.

Now using the energy loss histogram (see Fig 3.14) the number of ^{25}Si isotopes could be counted for the same amount of current as in the case of target detector giving the implantation rate at 0.76 event/nC. It gives a 60% transmission rate when compared with the production on the target detector. Once everything is set, the settings for the AstroBoxII have to be changed for measuring a proton spectrum from ^{25}Si. The FG was set at 11 (amplification factor 1.22^{12}), anode voltage was raised to +390 V (this voltage was experimentally chosen based on how the amplitude of the signal depends on the anode bias), and the GG voltage was set to + 36 V and -330 V (the first one is enacted in “beam on” mode, the second one in “beam off”). The pulsing box had the following settings: implantation – 500 ms, move signal – 5 ms,

measurement – 500 ms, the Gating Grid offset – 5 ms. It should be pointed out that during the experiment a radioactive α-source was placed inside the AstroBoxII (see Fig. 3.15) for the purpose of monitoring changes in gas gain (assuming that the electronic gain is stable). The source is a mixture of 4 isotopes with 4 major α-lines from ^{148}Gd (3182.690(24) keV), ^{239}Pu (5156.59(14) keV), ^{241}Am (5485.56(12) keV), ^{244}Cm (5804.77(5) keV) [29].

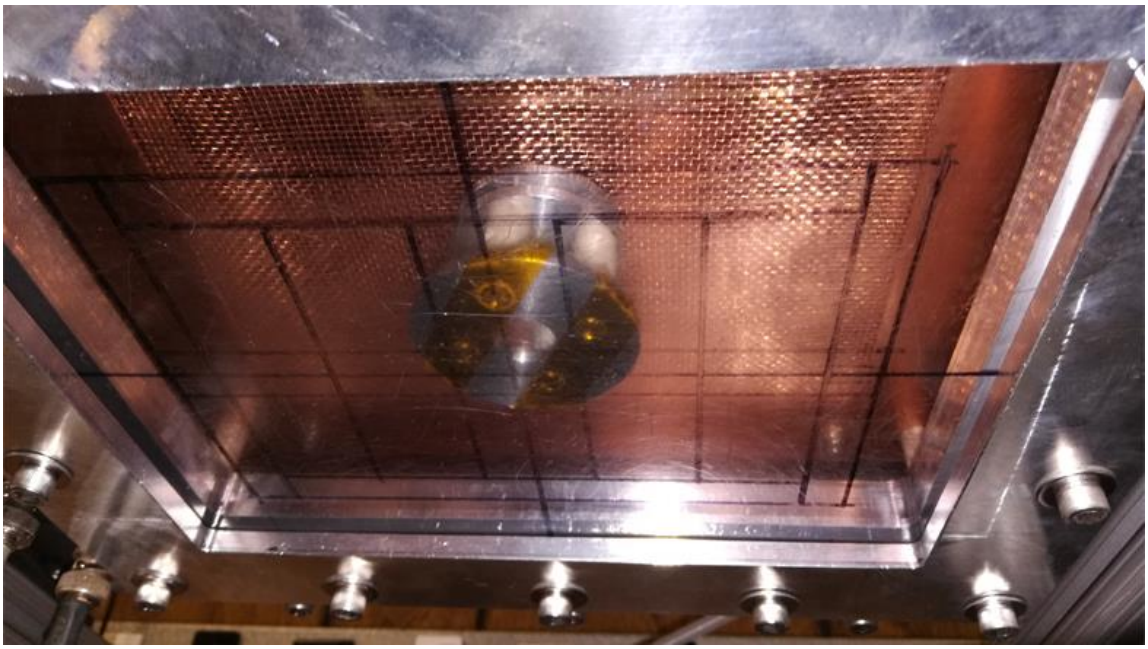

Figure 3. 15: α-source sits below the cathode. In the figure the source sits in C3 pad. In the actual experiment the source was placed over CR5 pad.

Since the given energies are significantly higher than the proton energies of interest, to fit the α-source into the dynamic range of the ADCs the setting for the FG, specifically for the pad CR5 (where the α-source sat) was set at 4 (actual gain $1.22^4 \approx 2.21$), the CG was set at 2. The CR5 pad was chosen because it was located fairly far from the center pads. As a result there were practically no decays occurring in this pad. To be precise 4 channels in the shaper1 (see Fig. 3.8) were set to the same FG since the Mesytec shapers have channels divided in 4 different groups. The other three groups have FG set at 11 (actual gain $1.22^{11} = 8.91$) CG was set at 2. Monitoring the shift in gas gain is important as the AstroBoxII is sensitive enough to see the temperature fluctuations in the order of several tenths of a degree (see gain drift in Fig. 4.17

from Data Analysis Chapter). This was observed numerous times during tests, so it was important to monitor the gas gain shift during the experiment. The utility of this monitoring will be discussed more in the data analysis section. After everything is set the slits3 were opened left and right ± 4 cm and slits4 were opened to left and right ± 3 cm. The coffin slits were opened ± 2 cm. This allows collecting enough statistics to calibrate 15 central pads. The calibration spectra were collected for both experiments (in July and in October) over about the same amount of time ~ 1.5 day.

3.7 Gamma ray detectors

An important part of the setup was utilizing 4 HPGe detectors also referred to as Clover detectors (the position of the Ge crystals within the detector resembles a clover leaf). These detectors were used to see if there are the coincidences between gamma and proton emission. Every detector has 4 leaves – essentially independent crystals with individual readouts. The preamplifiers were already built into the detectors themselves. The shapers used for the HPGe were of the same type used for the AstroBoxII Mesytec MSCF-16. The resolution provided by the Clovers was ~ 3 keV at 1.33 MeV from a ^{60}Co source. They were located as close to the AstroBoxII as possible, symmetrically on both sides of the beam travel. The main idea behind using the HPGe detectors was to have a coincidence scheme between proton detection and γ-ray detection. This allows excluding those cases when an excited state in ^{35}Ar decays into an excited state in ^{34}Cl* + p. If such events occur then it would be possible to see a coincidence between a proton emitted by ^{35}Ar* and a γ-ray followed by de-excitation of ^{34}Cl*. These states, however, are of no direct interest in the present thesis work as they do not contribute to the astrophysical reaction rate. As the main goal is the study of resonance capture of a proton by ^{34}Cl, with the latter being in the ground state. Theoretically one could utilize these gamma detectors for determining the branching ratios (proton/gamma) of a given state, but very low efficiency along with a limited amount of beam time does not make it possible. The gamma efficiency of the actual setup was established with a ^{137}Cs source with a single strong line at 661.657(3) keV [29]. To have an idea about the efficiency all across the sensitive volume of the AstroBoxII the source was attached to a string and then moved across the most important 15

central pads. These measurements were done after the experiment and instead of real Micromegas the “dummy” plate was used.

	Clovers	HPGe(1+2)
C1	0.0074	0.00269
C2	0.00784	0.00282
C3	0.00777	0.00301
C4	0.00775	0.00287
C5	0.00765	0.00275
CL1	0.0072	0.00273
CL2	0.00732	0.00286
CL3	0.00737	0.0029
CL4	0.00731	0.0028
CL5	0.00695	0.00266
CR1	0.00761	0.00277
CR2	0.00536	0.00285
CR3	0.00788	0.00294
CR4	0.00797	0.00298
CR5	0.00798	0.00284

Table 3. 2: Efficiency of the Clovers versus Ortec HPGe detectors. This data was determined as a ratio of a number of a detected event in a particular crystal to a known activity produced by the source for the same period of time.

The results are presented in Table 3.2 in the left column are the efficiency values for the experimental setup (for different pads). In the right column for comparison the efficiency measurements done with same technique but instead of Clovers a pair of HPGe detectors was used (from a test experiment). The switch of gamma ray detectors from the test experiment to the setup actually used in the present work allowed improving the efficiency by a factor ~2.5. This is in agreement with the manufacturer claims. Also efficiency curve was measured with

^{152}Eu source using the same method for source attachment as with the ^{137}Cs source. Six gamma lines were used 121.77(3) keV, 244.66(3) keV, 344.29(3) keV, 778.9045(24) keV, 964.057(5) keV, 1408.013(3) keV the results are shown in the Fig 3.16.

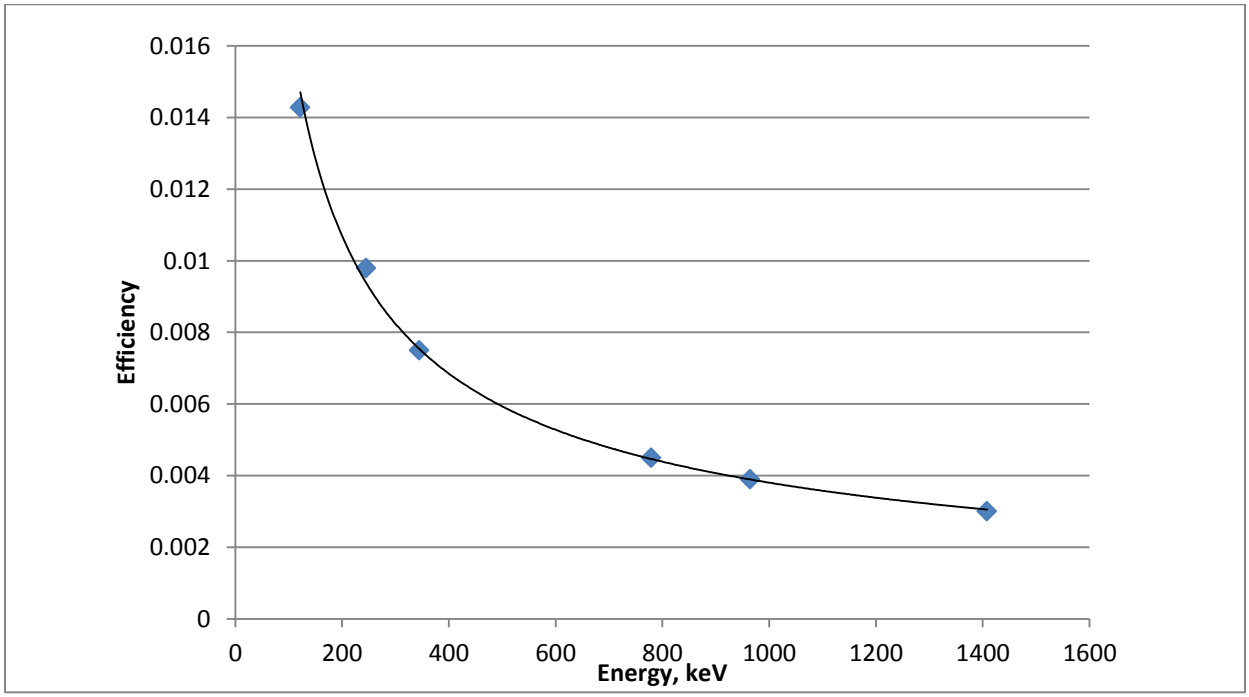

Figure 3. 16: Efficiency versus gamma energy. Data obtained from ^{152}Eu gamma source for the C3 pad. The efficiency is combined from all 16 crystals (Clover leaves).

The calibration of the gamma detectors was done before the run and verified after it. Multiple sources were used ^{133}Ba (31 keV, 81 keV), ^{137}Cs (661.657 keV), ^{54}Mn (834.82 keV), ^{60}Co (1173.2 keV, 1332.5 keV), and ^{152}Eu (multiple lines) [29]. The hardware of a Clover detector allows utilizing the core when the combined signal from 4 leaves can provide better efficiency. However, the resolution from the cores was much worse – 12 keV at 1.33 MeV. That is about 4 times worse than an individual crystal (leaf).

3.8 ^{35}K measurements

After the calibration the next step was switching to the ^{35}K secondary beam. The primary beam was switched to ^{36}Ar (18^{+} charged state). It was run at the same energy as ^{25}Si at 36 MeV/A. This energy was chosen to maximize the cross section on one hand, but also keep the intensity high enough to have good production rate. The other major change was using as a target of H_2 gas in a gas cell cooled to 77 K by LN_2. The production mechanism for ^{35}K was ^{1}H(^{36}Ar, ^{35}K)2n. After going through the same procedure of tuning MARS as for ^{25}Si secondary beam the following isotope production was achieved: ^{35}K: 2.7 event/nC, ^{33}Ar: 0.02 event/nC, ^{34}Ar: 0.02 event/nC, ^{32}Cl: 0.61 event/nC (see Fig 3.17). The same method for determining production was used as in the case of ^{25}Si.

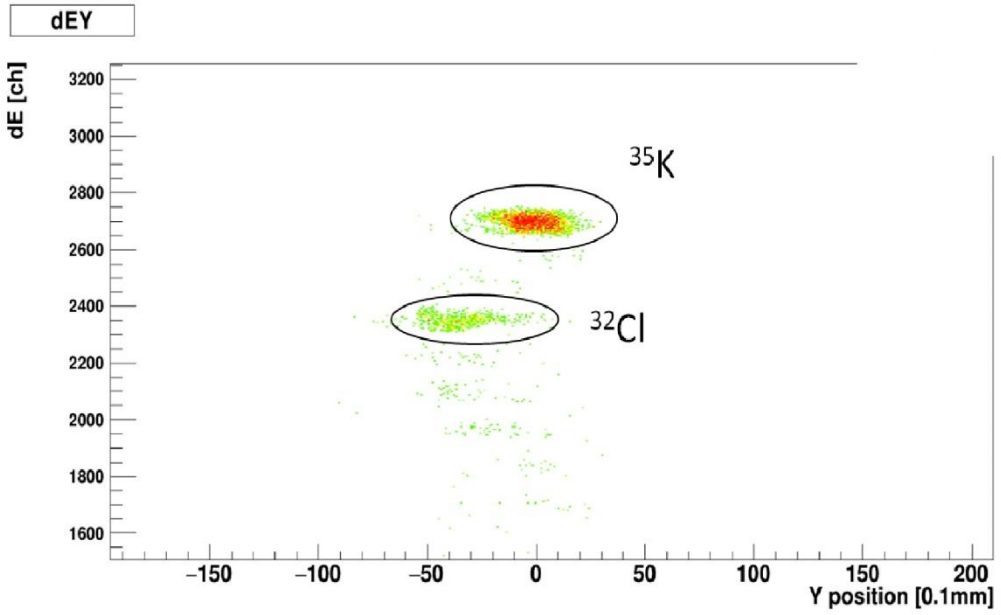

Figure 3. 17: ^{35}K seen in the target detector. Here different colors represent different intensities. On the y-axis is energy loss in channels. On the x-axis is the position relative to the center of the target detector. The picture shows the October experiment.

After this the AstroBoxII was switched to the implantation mode as in the case of ^{25}Si. The implantation rate of ^{35}K and ^{32}Cl inside the AstroBoxII were 1.1 event/nC and 0.23 event/nC correspondingly (the October experiment). This gives a transmission probability at ~ 40%. The aluminum degrader was set at 24 degrees. Also there was a change in the duration of "implant" and "measure" phases of the pulsing box. Both were set to 400 ms (see Table 3.12). After returning the settings for the AstroBoxII and the electronic gain to the calibration settings, the collection of the proton spectra began.

3.9 ^{32}Cl measurements

Since the presence of the ^{32}Cl in the cocktail of isotopes during the ^{35}K experiment was significant and ^{32}Cl was also known as a proton emitter, it was decided to tune MARS specifically for ^{32}Cl production and collect a spectrum for background subtraction from ^{35}K data set. This was done by changing the setting for D1-D2 dipole magnets to adjust the rigidity of the secondary beam. The production of ^{32}Cl, ^{36}K, ^{34}Ar was 5.93, 3.98, 1.97 event/nC respectively (see Fig. 3.18).

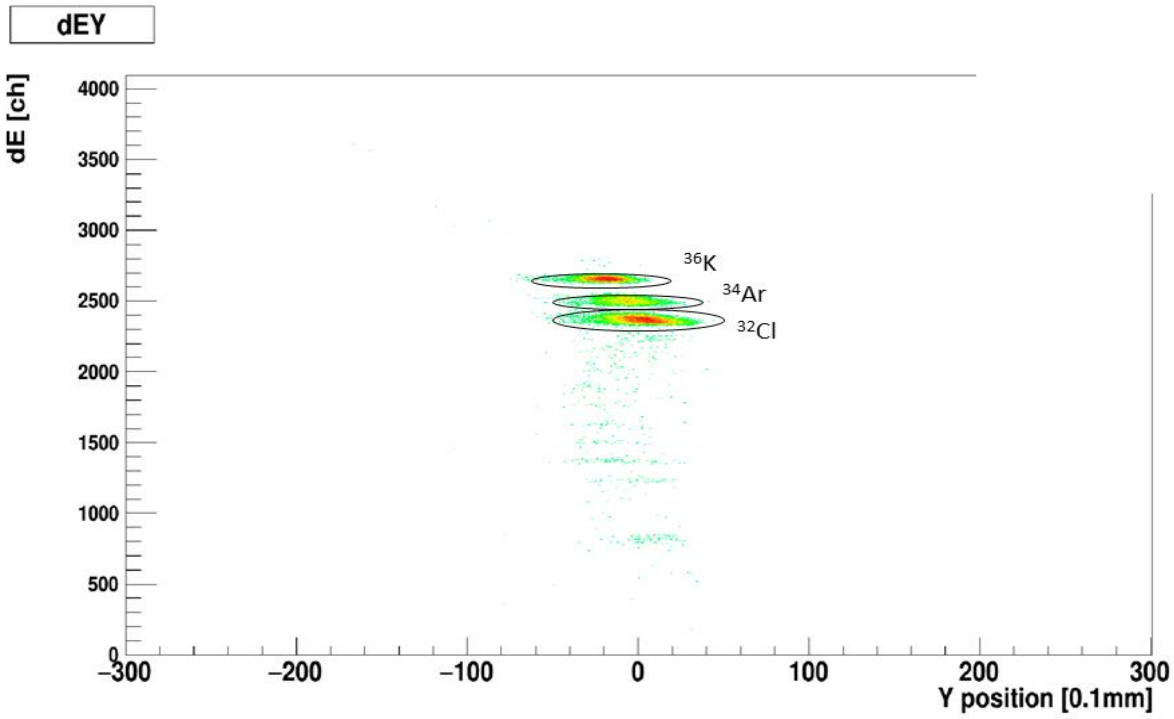

Figure 3. 18: ^{32}Cl in the target detector. The quantity dEY represents the energy loss in the detector, which is plotted versus the vertical position given as the x-axis. Also, visible is a significant presence of ^{36}K and ^{34}Ar.

The final setting for the degrader was 32.5^{0} and “implant” and “measure” times were set at 600ms. A spectrum of protons was collected over about one day of time. It should be noted that the data rate in case of ^{32}Cl was much higher than for ^{35}K, which led to some unexpected consequences that are discussed in the data analysis section.

4. DATA ANALYSIS

4.1 Linearity checks

One the first checks to perform near the beginning of the experiment is a linearity check of the system. It was performed with the Ortec Reasearch Pulser 448. It allows for setting discrete pulse heights by adjusting a calibrated dial on the front panel. In case of the AstroBoxII, the pulses were fed directly into the MSCF-16 preamplifiers to assure that the signal goes through the same electronic chain as the actual signals generated by the charged particles in the sensitive volume of the detector. The pulse heights were chosen in such way that that they could reliably cover the dynamic range of the ADCs used in the experiment. Another important aspect of the linearity check is that the calibration of the AstroBoxII (which will be discussed later) was done with ^{25}Si decays. The three major proton lines used for the calibration were 401(1) keV, 555(11) keV, and 943(2) keV [29]. It is possible in the case of ^{35}K that some proton lines exist below 401 keV, where there is no reliable calibration point. This makes the linearity check even more important to make sure that the system response is highly linear when we go below the lowest energy provided by the 401 keV line.

A simple linear function was chosen for a fit, $y = a + bx$ where a and b are coefficients – the intercept and slope, respectively. The positions of the centroids from the pulser were determined with software in *ROOT* [57]. A simple program then makes a fit and provides parameters of the fit. A *chi-square* test was used to estimate the 'goodness' of the fit. The *chi-square* is defined as

$$\chi^2 = \sum_{k=1}^{n} \frac{(O_k - E_k)^2}{\sigma_k^2} \tag{4.1}$$

In equation (4.1) O_k is the observed value and E_k is the expected theoretical value, and σ_k^2 is the variance of O_k. As can be seen from the 4.1 expression, the *chi-square* will have a tendency to grow as the number of the experimental points increases. Therefore it is convenient to normalize the 4.1 definition. In error analysis, the *reduced chi-square* provides a normalized

version since it takes into account the number of degrees of freedom. By definition, the *reduced chi-square* is

$$\chi_r^2 = \frac{1}{v}\sum_{k=1}^{n}\frac{(O_k - E_k)^2}{\sigma_k^2} \quad . \tag{4.2}$$

The only difference between the expression 4.2 and 4.1 is that the former is divided by the number degrees of freedom v, which is calculated by subtracting the number of fit parameters from the number of data points that are used. In the case of a linear fit there are just two parameters a and b (intercept and slope respectively). Analyzing the data from the two experiments, it was discovered that the reduced Chi-square is significantly larger than 1 (normally a good measure of a fit function is a value close to one) (see Table 4.1).

Fit method	χ_r (July 2017)	χ_r (October 2017)
Linear	306.803	709.452
Quadratic	133.413	280.245
Cubic	26.131	50.604

Table 4. 1: Shows reduced Chi-squared for three different polynomial fits. The data shown here is for CL4 pad.

Further investigation of causes for a poor fit involved building the residuals table for every pad in which the known data point values were subtracted from the values obtained from the fit and then plotted in a 2D graph versus the value of the amplitude (numerical value on the dial of the pulser). As it can be seen from Fig. 4.1, the residuals were following certain trends, thus making it look like it was not a statistical error, but a systematic one. The residuals were calculated as a difference between an experimental data point and the point obtained from linear fit. To be completely sure that the systematic error was generated by the pulser only, one would need to do a separate test with a high precision voltmeter. However such equipment was not available for the present work.

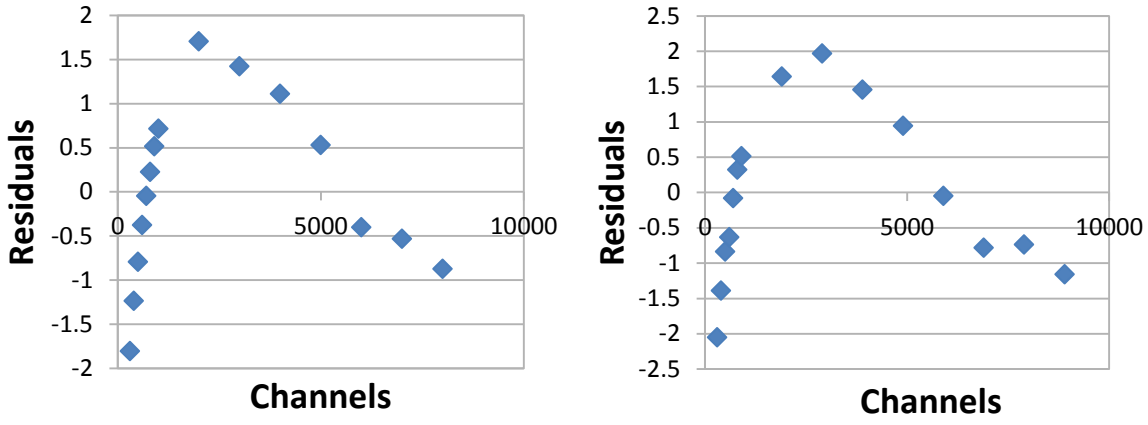

Figure 4. 1: Residuals on the y-axis (difference between the fit and experimental data point) plotted versus the value of the amplitude dialed on the pulser on the x-axis. Left and right graphs show the July and October experiments correspondingly.

As it was mentioned previously, this was not just a check of the linearity, but also an experimental determination of the zero point in the ADCs. After trying different approximation fits (linear, quadratic, cubic) it was decided that the quadratic ones generated a lower value of *chi-square*. A cubic fit was also considered as an alternative, but it was already overfitting

(based on the great reduction in *chi-square,* see Table 4.1) the data and unnecessarily complicating the fitting procedure.

4.2 Calibration procedure

Calibration of the AstroBoxII is important as its precision will be one of the major factors that will contribute to the resolution of the whole system. As was noted the system was calibrated with proton decays from a source of ^{25}Si. The following proton groups were used for calibration: 401(1) keV, 555(11) keV, and 943(2) keV [29]. Because the first proton group (401 keV) is much more intense than the other two, getting enough statistics for the remaining 555 keV line and 943 keV line in the CL and CR pads was problematic (the pads map in is the experimental chapter Fig. 3.6). Therefore getting the zero point in the ADCs would provide a valuable bit of information especially given the fact that there was no reliable proton group below 401 keV.

During the measurements of ^{35}K decay, the beam is collimated in such way that most of the nuclei stop in the C3 pad. However as the experiment is performed, there necessarily will be nuclei stopped in the neighboring pads. Therefore to have better statistics as well as counting the protons stopping over two or more pads one needs to have a reliable calibration for at least 15 central pads. That is why the beam of ^{25}Si is purposefully spread over the entire area of the detector. The spread of the beam is controlled by the Coffin slits as well as Slits3 and Slits4 (from the schematics of MARS Fig. 3.2). It is important to point it out here that the ^{35}K data set is based on two experiments performed in July and October 2017. As a result there were two different calibrations done, independent of each other for each experiment. Before integrating the peaks and determining the energies of the ^{25}Si proton group one needs to check the stability of the system as it will affect the positions of the proton lines used in the calibration procedure. Plotting the energy during the “beam-off” period versus time can provide important information about the stability of the system during the calibration. The plot (see Fig.4.2) from the July experiment did not reveal anything abnormal, since the 401 keV, 555 keV, 943 keV lines remain stable (no change on the y-axis).

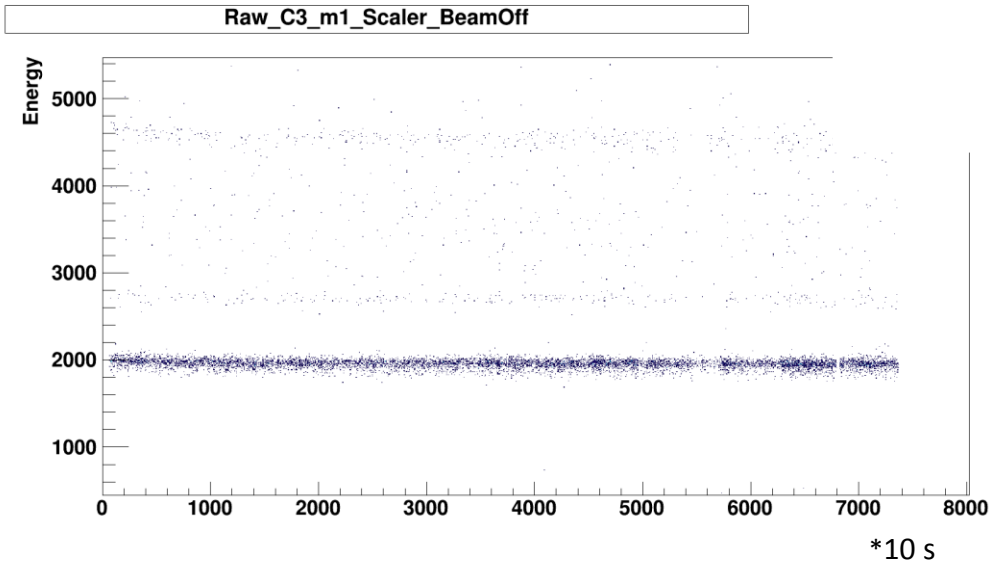

Figure 4. 2: Energy in the C3 pad (in channels) on the y-axis plotted versus time (x10 seconds) on the x- axis for the July experiment. As can be seen from the plot, the line around channel 2000 (401 keV line) stays relatively flat

The projection of energy on the y-axis shows no relative movement of the centroid. In the October experiment however there was a noticeable shift in the position of the 401 keV line (Fig. 4.3) with time (555 kev and 943 keV lines exhibited similar behavior, but due to lower statistics it was not as obvious).

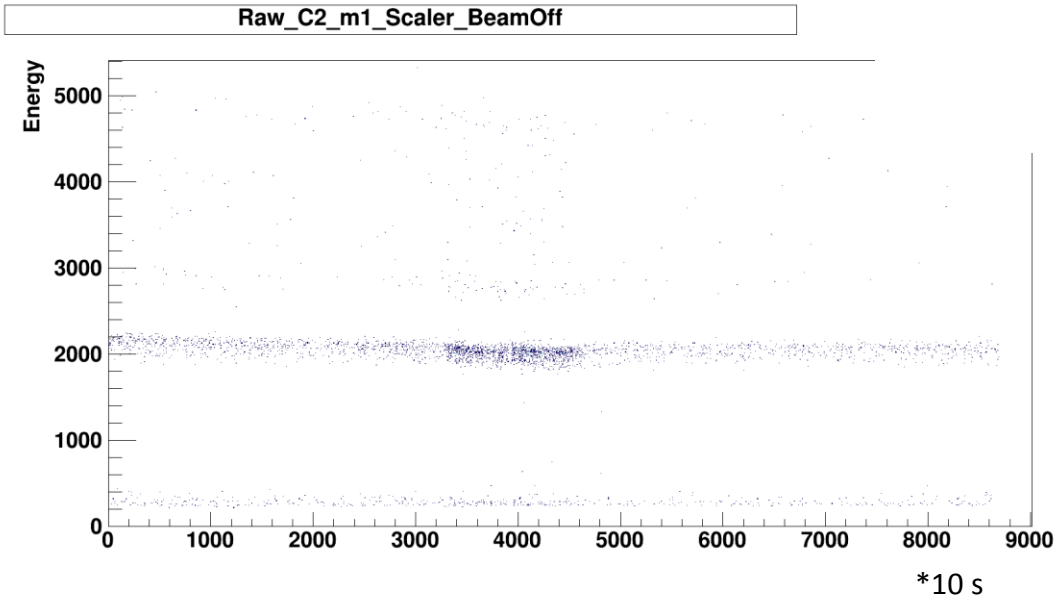

Figure 4. 3: Energy in channels (y-axis) versus time (x-axis) in the C2 pad for the October data. A noticeable shift in energy for 401 keV line can be seen.

It is interesting to point out that that the middle section (channel 4000 on x-axis) of the picture shows another position shift which is most likely linked to higher beam current for that section. The typical beam current was about a factor of 3 higher for these runs. The difference between the highest and the lowest peak projection on the y-axis is as high as 100 channels. This yields an energy shift of about ~ 20 keV. Also in contrast to this the two neighboring pads, namely the CL3 and the CR3 have almost no shift in the position of the peak. When taking into account the 555 keV and 943 keV lines it becomes obvious that the present effect is a non-linear one, as the shift appears to be bigger for the higher energy lines. Therefore a simple linear adjustment would not suffice. With a closer inspection of the behavior of 401 keV line it becomes obvious that there was a slow shift in energy for the first several runs. Normally such shifts could be connected to a temperature change. However, there was no visible daily drift (see Fig. 4.4).

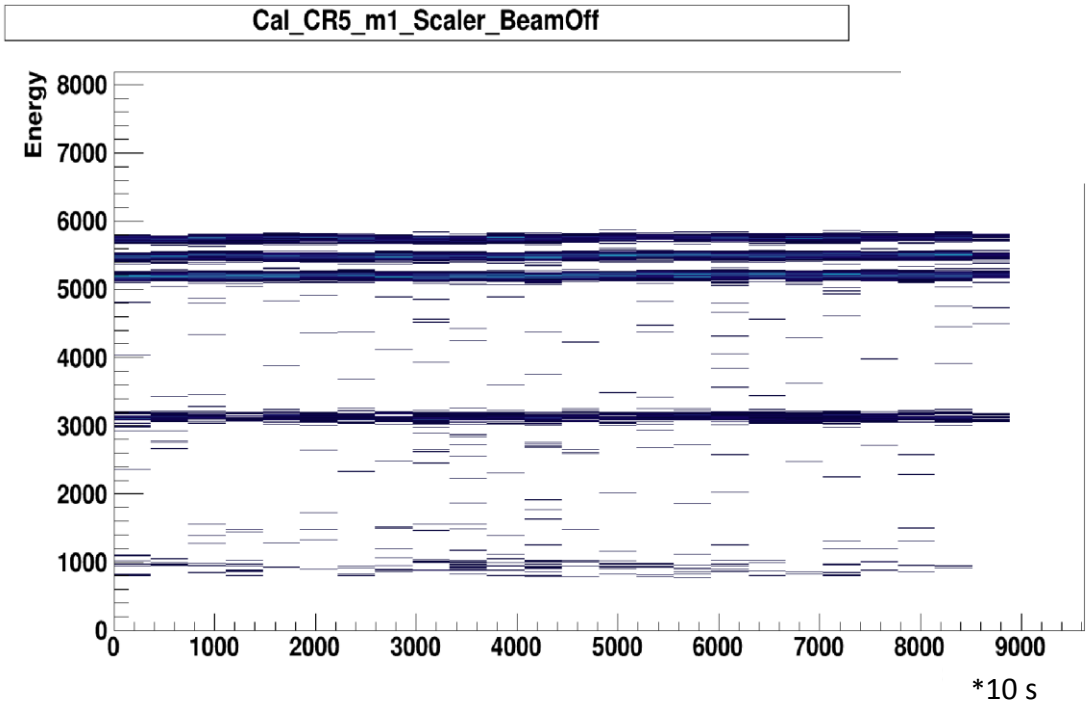

Figure 4. 4: Energy on the y-axis in the CR5 pad (where the 4 peak alpha source was sitting) versus time on the x-axis. The y-axis is in keV units and x-axis is in *10 seconds units.

Also, the temperature could be checked only manually every 8 hours when accessing the cave. The temperature throughout the records appears to be the same at 23^0 C, but the precision of this instrument is ± 1 ^{0}C. Also the thermometer used to monitor temperature changes was sitting outside the AstroBoxII. Initially a calibration was tried with the last quarter of the ^{25}Si data set, but the amount of data for the CL and CR pads was insufficient for a good calibration. Eventually it was decided to use all of the data set at the cost of increased uncertainty as it was not possible to determine the exact causes of the shift.

4.3 Absolute branching ratios for ^{25}Si

Another useful check is to see how the observed absolute branching ratios for the major proton groups of ^{25}Si compare to the literature results. In this case it is a simple ratio of protons/implants with the corrections noted below. The number of protons in a given peak is

measured by simply integrating the peak yield in the energy spectrum for multiplicity one events during the "beam-off" period. The histograms are gated in the way that only ions traveling through the central pads and not beyond a certain pad (can be changed in the software) are displayed in the picture and can be counted. As an example below a histogram (Fig. 4.5) that was gated on left (CL) pads and right (CR) pads so only those ions that traveled over the central pads (C pads) is shown. In this particular example there was an additional gate on the C4 pad.

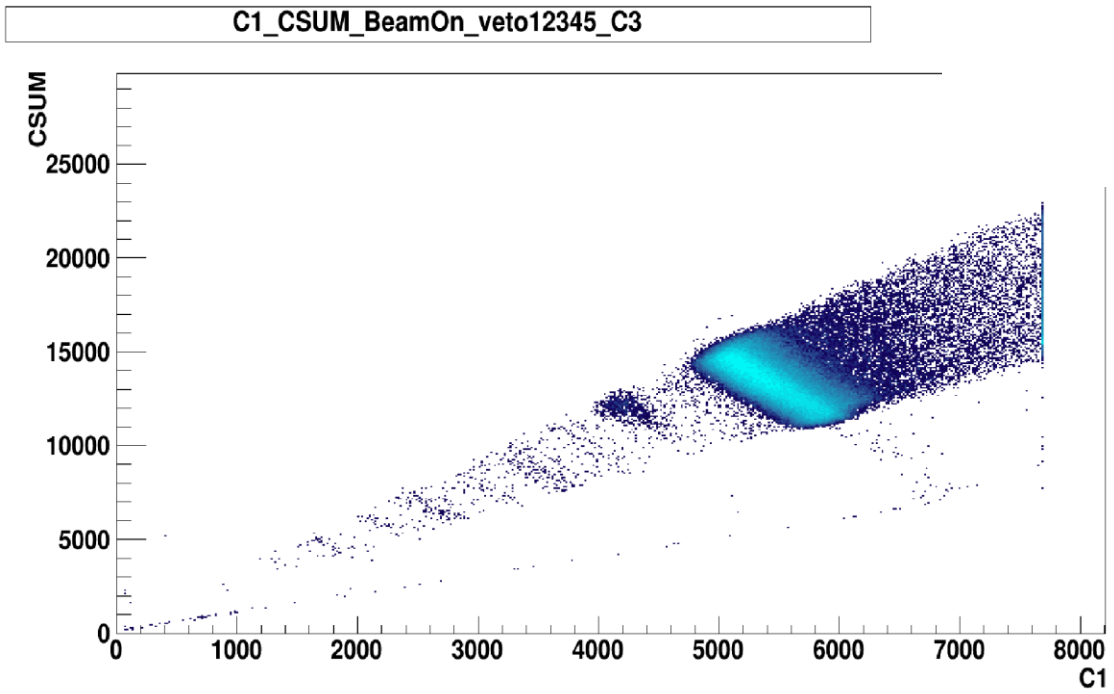

Figure 4. 5: The sum of energies (channel units) from C1->C5 pads on y-axis plotted versus energy (channel units) in the C1 pad during the "beam-on" period. The bigger group corresponds to ^{25}Si implants. These are the ions that stopped in the C3 pad.

Here multiplicity simply refers to how many pads are firing at the same time. One needs to be sure that the protons counted in the "beam-off" period originated from the decay of ^{25}Si

implanted during the “beam-on” period in the specific pad. After counting the number of implants in the central pads it is important to take into account the fact that while ^{25}Si was implanted during the “beam-on” period it was undergoing radioactive decay and the protons during this period are not counted. Protons will only be counted from those implants that decay during the “beam-off” period. However the total number of ^{25}Si is counted during the “beam-on” period. So the radioactive decay that will decrease the number of ^{25}Si, which are available for decay, in the “beam-off” period, needs to be taken into account. It can be shown [3] that when radioactivity is building up inside the AstroBoxII at the constant rate R particles per second and has a half-life time $t_{1/2}$ (220(3) ms for ^{25}Si [55]) the remaining number of atoms after time t elapses is given by

$$N = \frac{R}{\lambda}(1 - e^{-\lambda t}) \, . \tag{4.3}$$

In the formula (4.3), λ is the decay constant, which is related to the half-life by a simple relation

$$\lambda = \ln(2)/t_{1/2} \, . \tag{4.4}$$

When taking into account this effect, only $\approx$ 0.5 of the isotopes of ^{25}Si are remaining at the beginning of the “beam-off” period (see Fig 4.6).

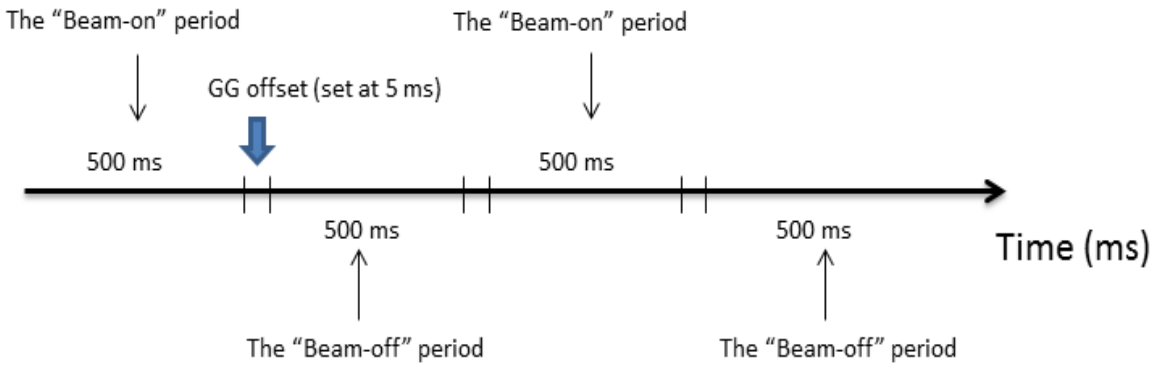

Figure 4. 6: The schematic of timing during the "beam-on" and "beam-off" periods. Time is on the x-axis in milliseconds.

Also one needs to be careful about counting the protons. The "beam-off" period is 500 ms long while ^{25}Si has a half-life time 220(3) ms [55]. As a result only 79.3% of the implanted nuclei will decay on average. Theoretically it is possible to extend the "beam-off" period to a value that would allow (practically) the decay of all ^{25}Si nuclei, but it would come at the cost of reduced "beam-on" period. In fact it can be shown from the formula (4.3) that 75% of radioactivity comes from two half-lives. Increasing it more will create more isotopes available for decay. That, however, shortens the measurement period ("beam-off"). So overall the best timing strategy is to keep the implantation time ("beam-on") at roughly two half-lives.

Another important aspect of the calculation of the absolute branching ratios is the knowledge about the efficiency of detection of protons at a given energy and multiplicity.

The simulated efficiency for the AstroBoxII was made by Dr. A. Saastamoinen [51] using the code GEANT 4. The simulated efficiency for a non-point like source for the 401 keV line was 0.75, 555 keV – 0.55, and 943 keV line – 0.17. These numbers are given for a multiplicity m=1 events. As the higher energy protons will be more likely to create a signal in more than one pad. Therefore such protons will not contribute to multiplicity one. The data set from the July experiment was used in calculating the absolute branching ratios for ^{25}Si, since the October

experiment had some issues with the gain drift discussed above. Also, only information obtained from the pads C2, C3, C4 were used for such calculations, as both the efficiency simulation and gating conditions for pads C1 and C5 were less reliable. It is due to the fact that the geometry for the pads C2, C3, C4 is identical, whereas pads C1 and C5 have different neighboring pads. Those include small pads on the entrance and exit correspondingly (see Fig. 3.6 in the Experimental chapter). The branching ratios were calculated individually for each of the C2, C3, C4 pads. After that an arithmetic average of these three pads was taken. Statistical errors were calculated appropriately. The result is shown in the table 4.2 below

Energy, keV	Present work ABR, %	Literature ABR, %
401	5.11(3)	4.75(32)
555	0.22(1)	0.69(25)
943	0.96(2)	1.63(2)

Table 4. 2: Absolute Branching Ratios (ABR) measured for ^{25}Si (absolute intensity values are given). Highlighted in grey color are the experimental results from the present work and in green – values taken from the literature [55].

It is worth noting that only statistical errors were taken into consideration while determining absolute branching ratios for ^{25}Si. The major contributor to the error comes from fairly low statistics for protons. Systematic errors are much harder to estimate due to their unknown nature and quantitative effect on the final result. Since the absolute branching ratios were not the main focus of this work the extracted values were deemed as satisfactory. Also, it is important to point out a significant discrepancy in absolute branching ratio (ABR) for a 555 keV proton group. It can be partially explained by the presence of a strong positron background measurement in the work described in reference [55]. Also the escaping proton background is a possible contributor to the error in counting protons during “beam-off” period. An experimental measurement of the half-life was possible. It was estimated for ^{25}Si at 216 ± 4 ms

for the July experiment and at 217±4 ms for the October experiment, these values are close to the literature value 220(3) ms [55].

4.4 Proton-gamma coincidences

As was mentioned before the idea of using gamma detectors was to help determine that a state that was populated in the emitter (^{35}Ar, ^{25}Al) decays to the ground state in the daughter (^{34}Cl or isomer state ^{34}Cl*, ^{24}Mg). For this reason coincidences between protons and gammas were added to the experimental setup. Since the data acquisition was triggered by the AstroBoxII, only those gammas that were detected during that time would tell if the state in the emitter decayed directly to the ground state. To establish that the coincidence scheme works, the calibration data set (^{25}Si) was used. The coincidence plot of protons versus gammas can be seen below in Fig. 4.7.

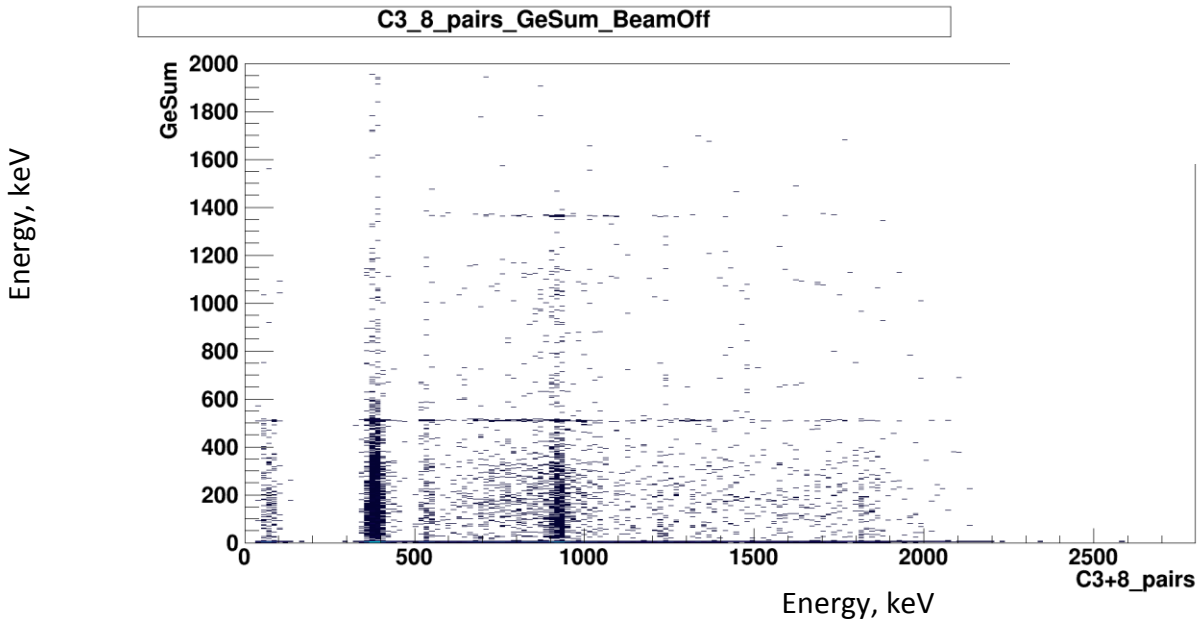

Figure 4. 7: (The July experiment). Energy spectrum from the AstroBoxII plotted versus energy from HPGe "Clover" detectors. On the x-axis is shown the combined proton energy spectrum of the C3 pad plus eight neighbor pads (multiplicity=2), on the y-axis the combined gamma energy spectrum from 16 individual crystals is plotted.

It can be seen from Fig. 4.7 that 511 keV gammas are visible all across the AstroBoxII decay data and, more importantly, for the gamma line at 1368.672(5) keV [29]. This corresponds to the first excited state in ^{24}Mg. It has fairly low statistics for 555 keV protons (see Fig. 4.7 x-axis), but much more for the 943 keV protons. The most intense line, on the other hand, 401 keV, decays directly to the ground state of ^{24}Mg. A similar check was also made for the October experiment to be sure that the setup was functioning properly. These three proton groups (401 keV, 555 keV, 943 keV) correspond to following energy levels in ^{25}Al 2673.3(6) keV, 4192(4) keV, and 4582(2) keV [55].

4.5 ^{35}K (The July experiment)

4.5.1 The "tune1"

In this section the results from the July experiment are discussed. During that experiment two slightly different tunes were used for the implants put into the detector. In the "tune1" there were three major isotopes in the AstroBoxII: ^{35}K, ^{36}K, ^{32}Cl. During the implant phase the Al degrader was set at 32 degrees. It allowed ^{35}K to be mostly stopped in the C3 pad with some amount in the C2 and C4 pads. The production of ^{32}Cl was comparable to the production of ^{35}K, while ^{36}K production was almost ten times smaller. The estimated absolute proton branches from the literature [29] are about two orders of magnitude smaller for ^{36}K than from ^{35}K. Also due to slightly bigger mass and energy into the detector, ^{36}K would almost entirely stop in the C2 pad. Given the production rate of ^{36}K relative to the ^{35}K along with significantly smaller absolute branching ratio, it should not have given appreciable contamination in the delayed protons coming from ^{35}K. ^{32}Cl, on the other hand is lighter and carries smaller charge so it would travel further in the AstroBoxII before it stopped. It is mostly present in the C4 pad. Below in Fig. 4.8 is the combined proton energy spectrum from the C2, C3, and C4 pads.

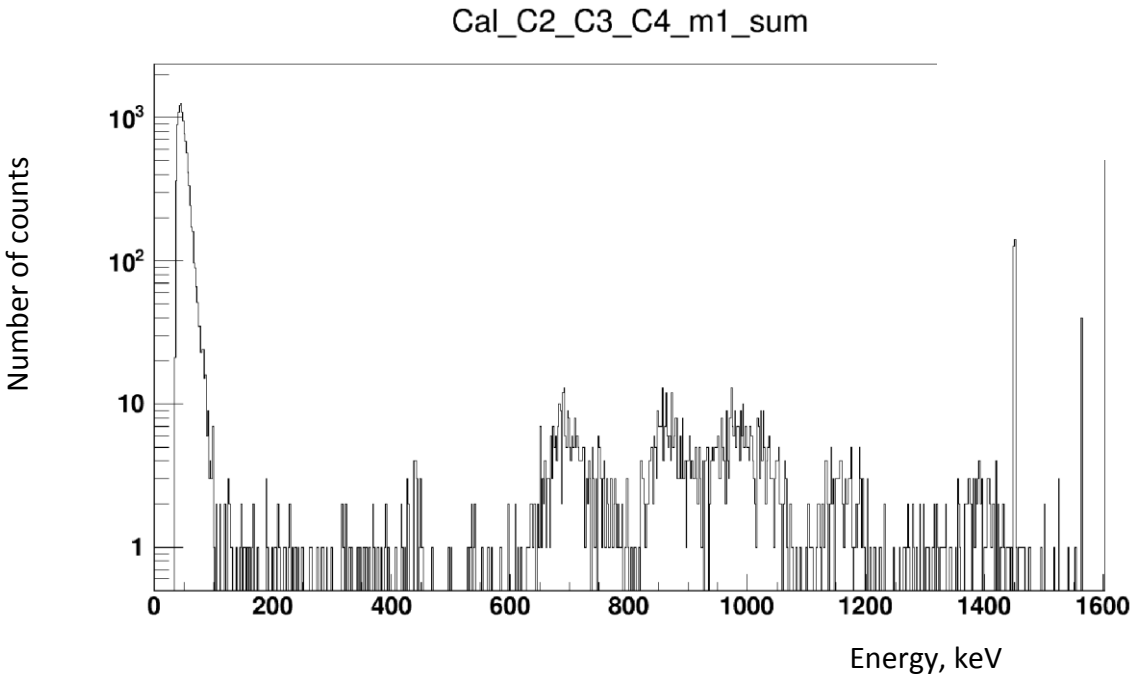

Figure 4. 8: Energy spectrum of protons (in keV on x-axis) combined from the C2, C3, and C4 pads. Number of counts is on the y-axis. The sharp peaks around 1400-1600 keV correspond to overflows in the ADCs for different pads.

Here it is important to note that the focus of this work is mostly on the low energy protons. It can be seen that below 500 keV only one group appears to be visible above the background. From the statistics it was determined that this line sits at around 435 (4) keV (here only statistical error was numerically evaluated). It should be pointed out that all energies measured are the total decay energy. When a proton unbound state decays the energy is shared between a proton and a nucleus. However not all the kinetic energy of the heavy ions goes to ionization of the gas in the AstroBoxII. Some fraction of the energy will be spent on recoiling ions and excitation. This fraction will depend upon the energy and mass of the heavy ion. Also a positron created in β^+ decay of ^{35}K also deposits a fraction of its energy in a given pad, which was estimated at ~ 3 keV.

By looking at the protons versus gammas in coincidence (Fig. 4.9) it is possible to tell if a given state in ^{35}Ar decays directly to the ground state of ^{34}Cl plus a proton.

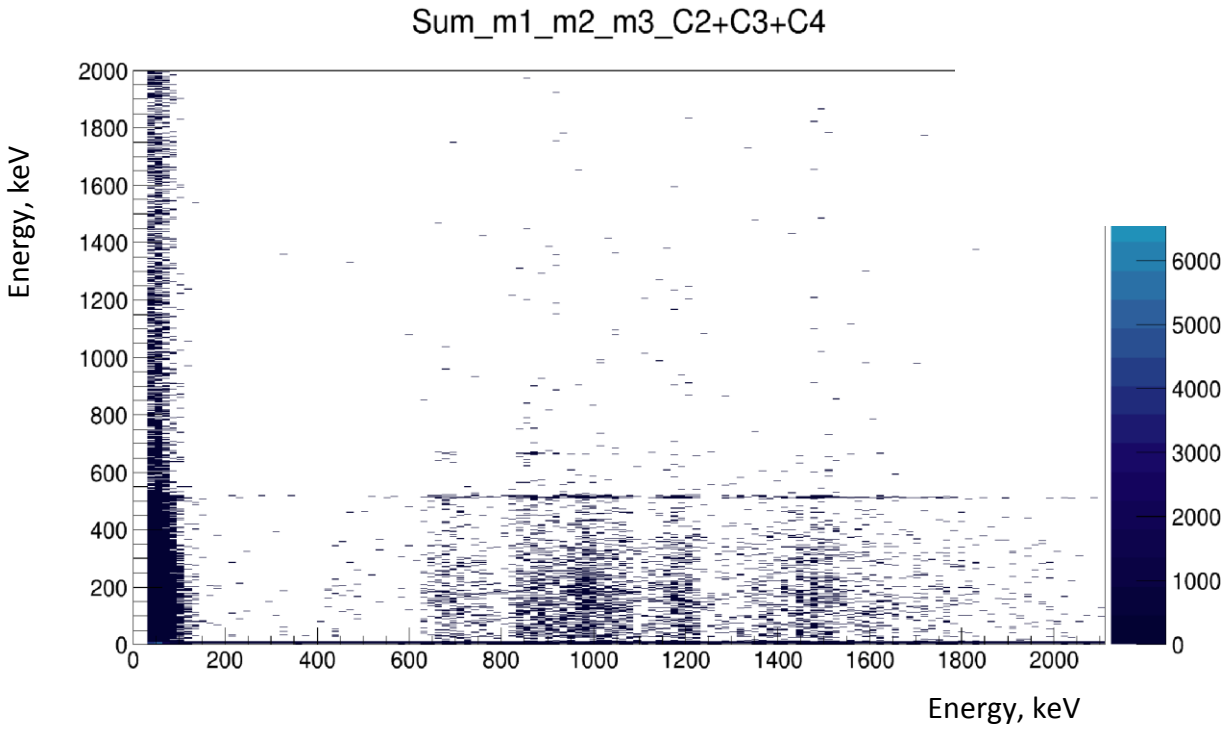

Figure 4. 9: Combined energy spectrum of protons (x-axis) from the central pads for multiplicities m=1, m=2, m=3 versus 16 germanium crystals combined (y-axis).

In the region of interest (<500 keV) there were no significant groups detected. However it should be noted that the gamma efficiency detection is below 0.7% for that region and that makes the detection of gammas very hard due to very limited statistics from the proton spectrum. It is possible to see coincidences of protons and gammas for 693(3) keV protons and 865(3) keV. These proton groups coincide with the measured gamma energy at 667(2) keV. This gamma line corresponds to the fourth excited state in ^{34}Cl, which is given in the literature as 665.56(4) [58]. The result quoted in this work is within the statistical uncertainty.

4.5.2 The "tune2"

During the experiment it was decided to change the tune of MARS in an attempt to eliminate ^{36}K from the AstroBoxII. By adjusting the rigidity of D1-2 magnets it was possible to almost entirely eliminate ^{36}K with only 0.6% of the rate of ^{35}K. The figure below (Fig. 4.10) shows comparison of the implantation spectra for "tune1" and "tune2"

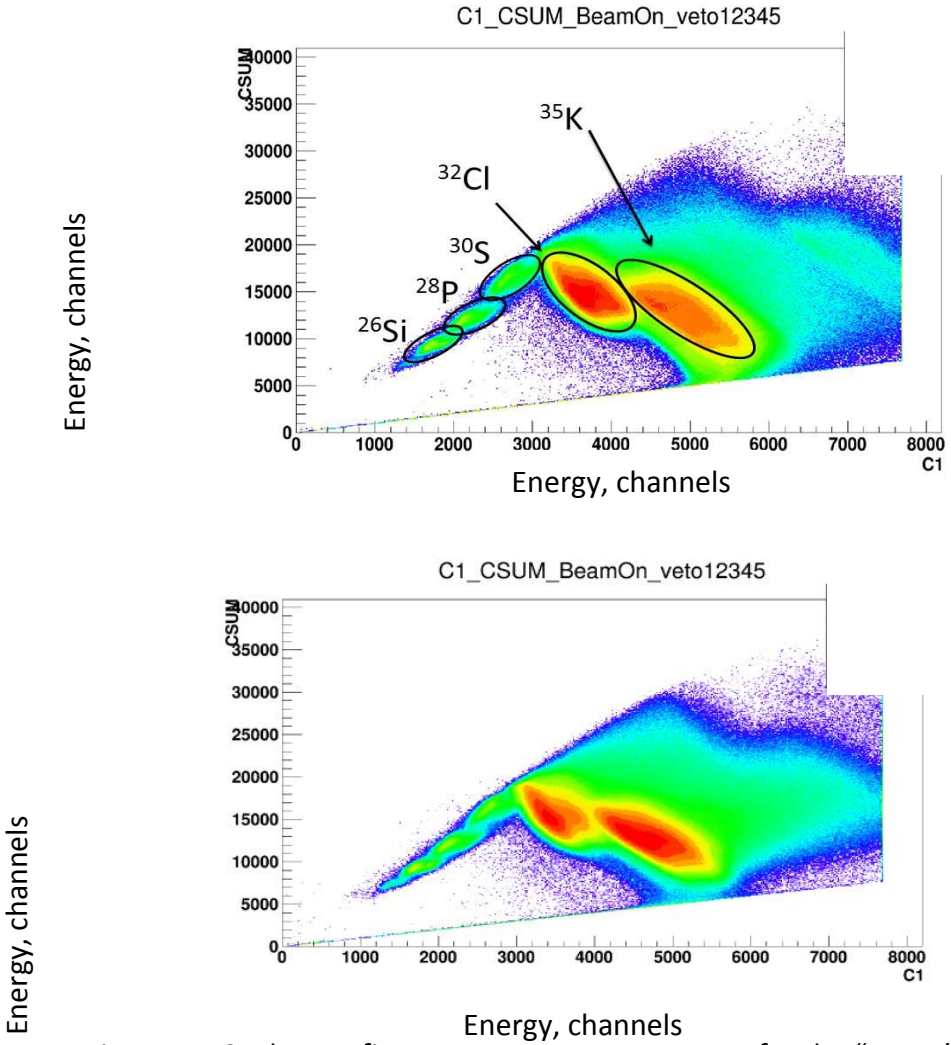

Figure 4. 10: The top figure shows the implantation for the "tune1" and the bottom one shows the same picture for the "tune2". On the y-axis is the sum of energies (in units of channels) of all central pads C1->C5 and on the x-axis only C1 pad (in units of channels).

It can be seen that on the top picture for the channel ~5000 on the x-axis and y-axis there is a presence of ^{36}K. It is visible as a small "shoulder" to the main peak, which is ^{35}K. The picture on the bottom does not have the same feature. Therefore the only meaningful contamination could come from ^{32}Cl. The resulting energy spectrum for the C2, C3, and C4 pads is presented below in Fig. 4.11.

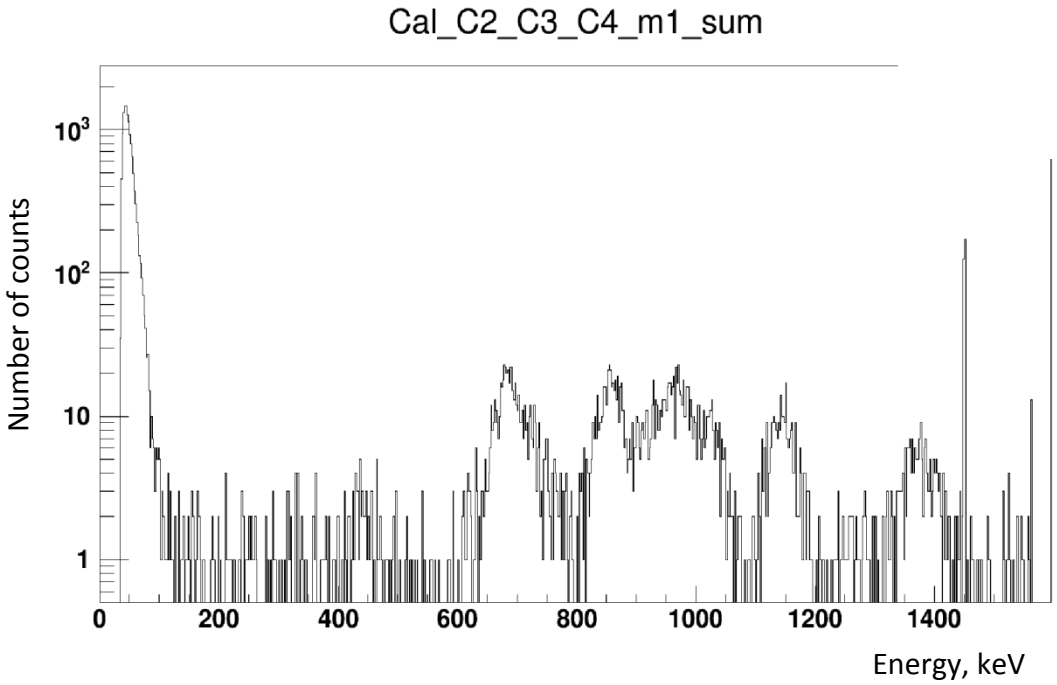

Figure 4. 11 Energy spectrum from the C2, C3, and C4 pads combined on the x-axis vs number of counts on the y-axis.

Like in the first tune, no major changes were observed. Again there is a visible buildup of counts around 441(4) keV. The two pads (C2 and C3) in the "tune2" should only include ^{35}K and no contaminants. With the addition of the C4 pad there will be some protons from ^{32}Cl protons, but their absolute proton branching ratios are about an order of magnitude smaller than for ^{35}K.

One of the possible contributors to the error of determining the energies for the proton peaks in ^{35}K decay is the possibility of the decay taking place on the cathode. On the figure below (Fig. 4.12) is shown a histogram that plotted energy from two pads (multiplicity=2) versus time difference between those two pads.

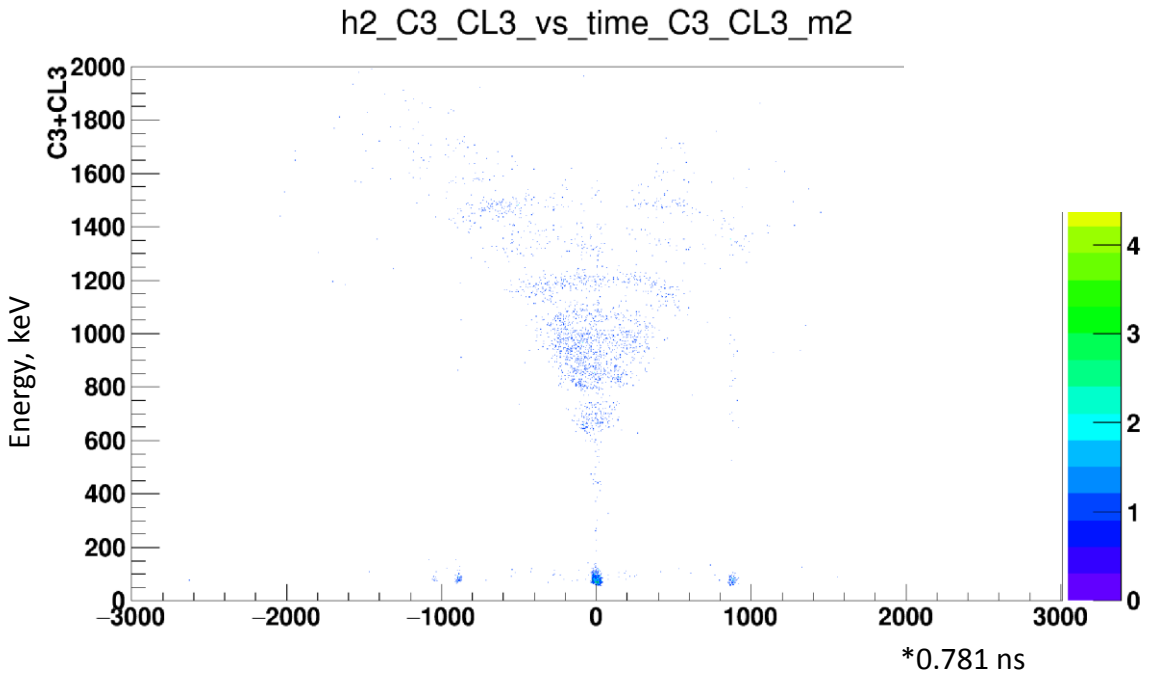

Figure 4. 12: Sum of energies from two pads C3 and CL3 (y-axis) plotted versus time difference between C3 and CL3 pad (x-axis). One channel on the x-axis corresponds to 0.781 nanoseconds.

It can be seen that there seem to be more particles on the negative side (relative to the zero point). That means that the times recorded from CL3 tend to be bigger than the times from C3. Ideally one would expect to have exactly the same number of particles going upward and downward, but due to ability of ^{35}K forming a positive ion, the number of ions traveling towards the cathode is higher by 30-40%. This corresponds to the situation when ions have preferred

direction of travel towards the cathode. However there was no reliable way to determine if the proton decay of ^{35}Ar was taking place on the cathode and in the given work such a possible contribution was neglected.

4.6 ^{35}K (The October experiment)

To improve the statistics of the first experiment (the July experiment) it was decided to carry out another run. The October experiment was run at settings similar to the "tune2" settings from the July run. Having more beam time allowed us to collect better statistics. The energy spectrum from the combined C2, C3, C4 pads was obtained as shown in Fig. 4.13 below.

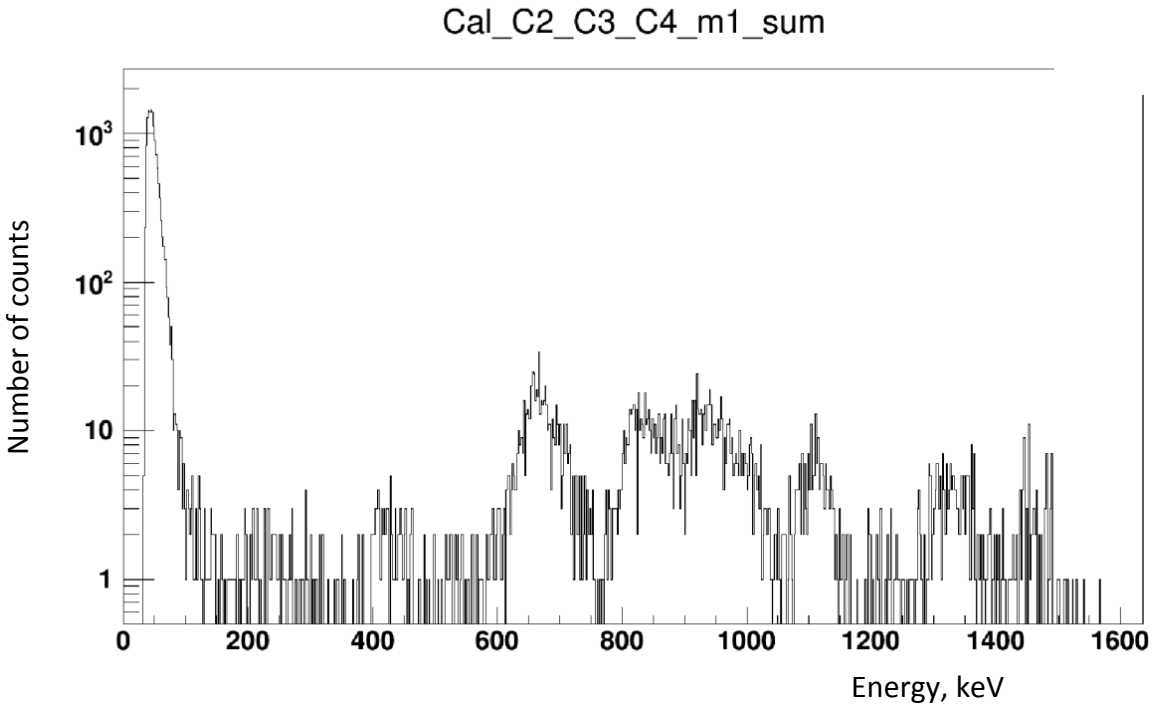

Figure 4. 13: Energy spectrum combined from ^{35}K (the C2, C3, C4) pads on the x-axis versus number of counts on the y-axis.

It is important to point out that because of inclusion of the C4 pad presence of ^{32}Cl is possible. Again the same group ~430 keV as in the July experiment was observed. In this experiment it was measured to be 441(11) keV. Also it should be remembered that the calibration in the October experiment had higher uncertainty than the one used in the July experiment. The compiled list of proton energies and errors is presented in the Table 4.3 (the data only from the October experiment).

E, p keV	^{35}Ar, keV	Error, keV
441	6329	5
685	7255	2
860	7431	3
948	7527	3
1132	7053	3
1345	7283	4

Table 4. 3: Measured energies of protons and corresponding energy levels in ^{35}Ar.

The coincidences between protons and gammas from ^{35}K are shown below in the Fig. 4.14

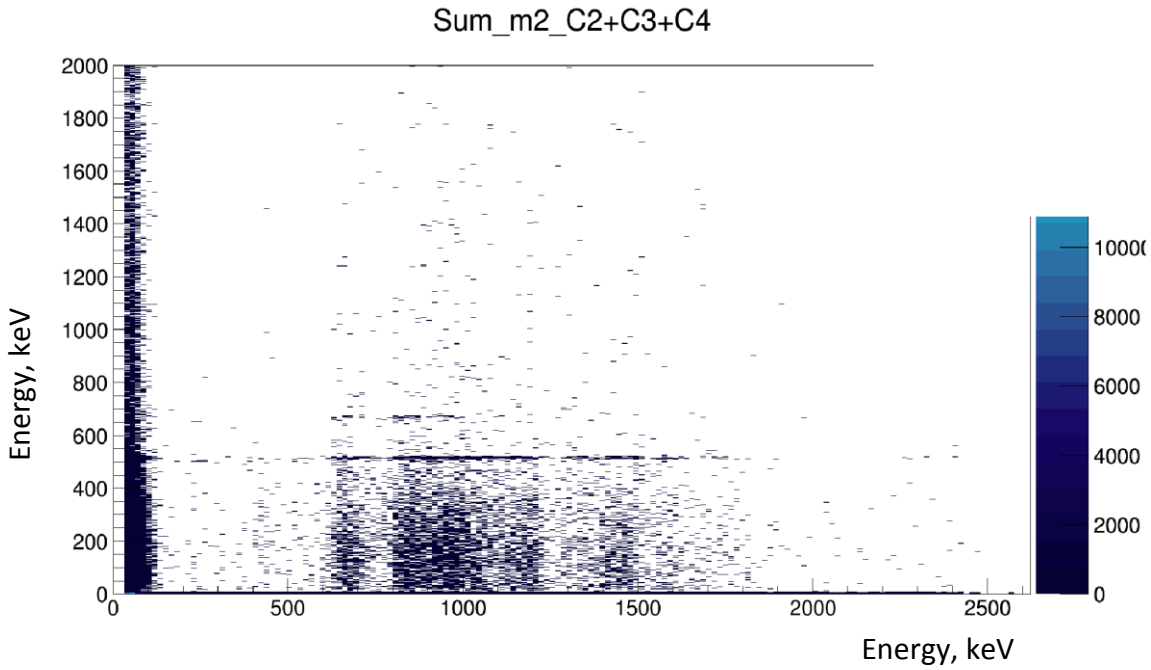

Figure 4. 14: Combined energy spectrum (keV) from the C3 plus 8 neighboring pads (multiplicity=2) on the x-axis versus 16 germanium crystals combined on the y-axis (the October experiment).

Again, no coincidences were detected in the region below 500 keV and just like in the July experiment one can see some coincidences for 665(2) keV and 840(3)keV protons with 665.56(4) keV protons [29]. The October experiment while having more statistics than the July experiment was less stable. During the ^{35}K run as well as ^{32}Cl there were significant gain fluctuations observed (see Fig. 4.15).

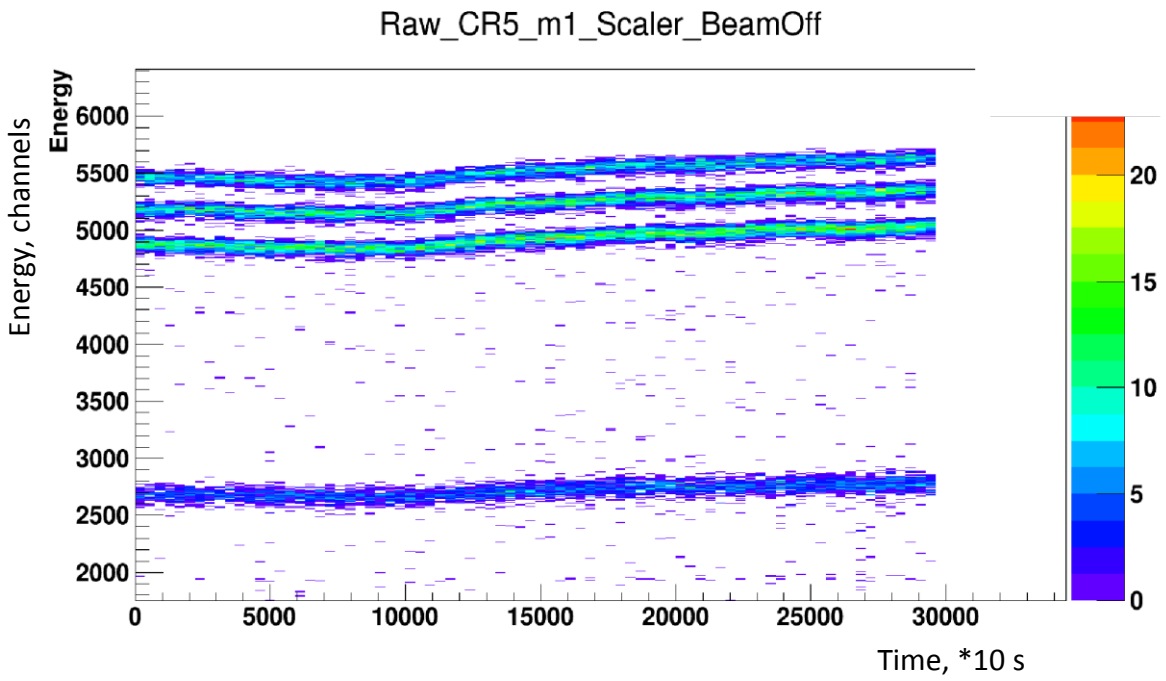

Figure 4. 15: Energy (non-calibrated) from 4 peak α-source on the y-axis plotted versus time on the x-axis. On the x-axis each buffer corresponds to 10 seconds. Data presented for ^{35}K case.

The corrections were based on monitoring the gain drift from the 4-peak α-source (^{148}Gd, ^{239}Pu, ^{241}Am, ^{244}Cm). They were taken into account by choosing the position of 4 peaks from earlier files of ^{35}K run, and then doing splits of the data and adjusting the position of 4 peaks appropriately to the chosen base. The gain drift was corrected for the 4 alpha lines (~3.1-5.8 MeV). The result is presented in the Fig. 4.16. As it can be seen from the Fig. 4.16, the method used to correct a gain shift produces flat lines for four alpha peaks. The exact same method was applied for a gain shift correction during the ^{32}Cl run.

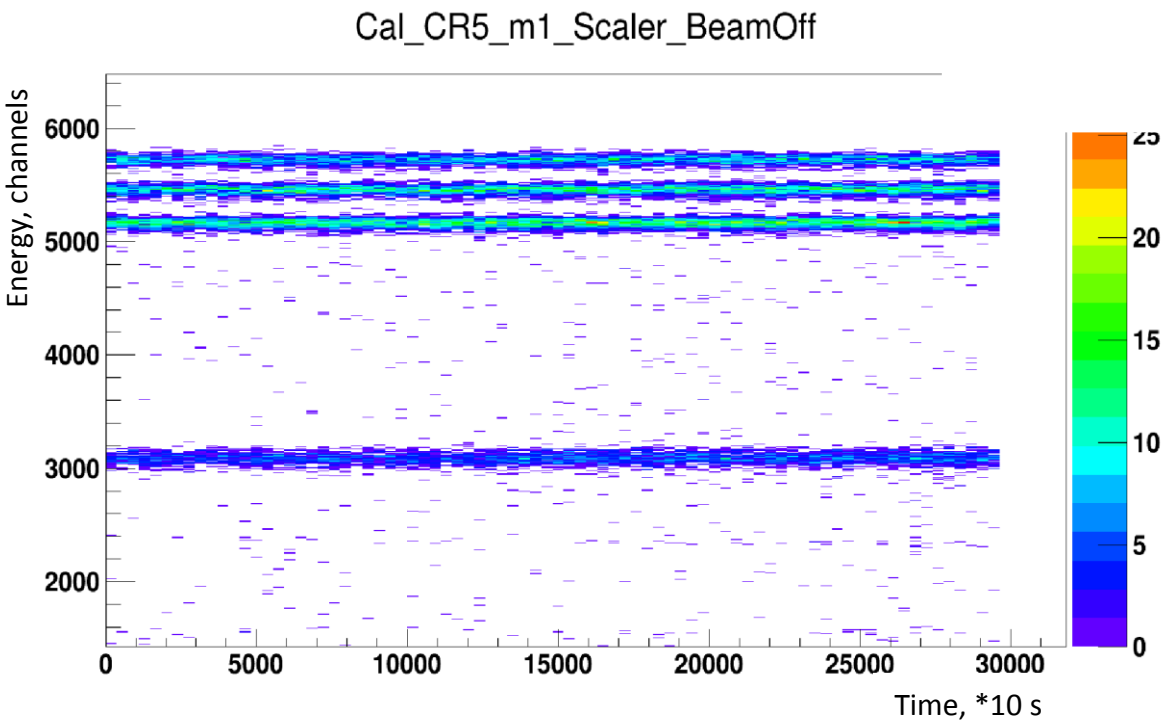

Figure 4. 16: Gain corrected energy (non-calibrated) from 4 peak α-source on the y-axis plotted versus time on the x-axis. On the x-axis each buffer corresponds to 10 seconds. Data presented for ^{35}K case.

4.7 ^{32}Cl (the October experiment)

Near the end of the October experiment, MARS was tuned purely for ^{32}Cl as it was still a possibility for contamination in the ^{35}K spectrum. During the implantation phase some amount of ^{32}Cl was always present (^{35}K data from the October experiment). In Fig 4.17 it can be seen as a smaller group below 4000 channels (the bigger group is ^{35}K).

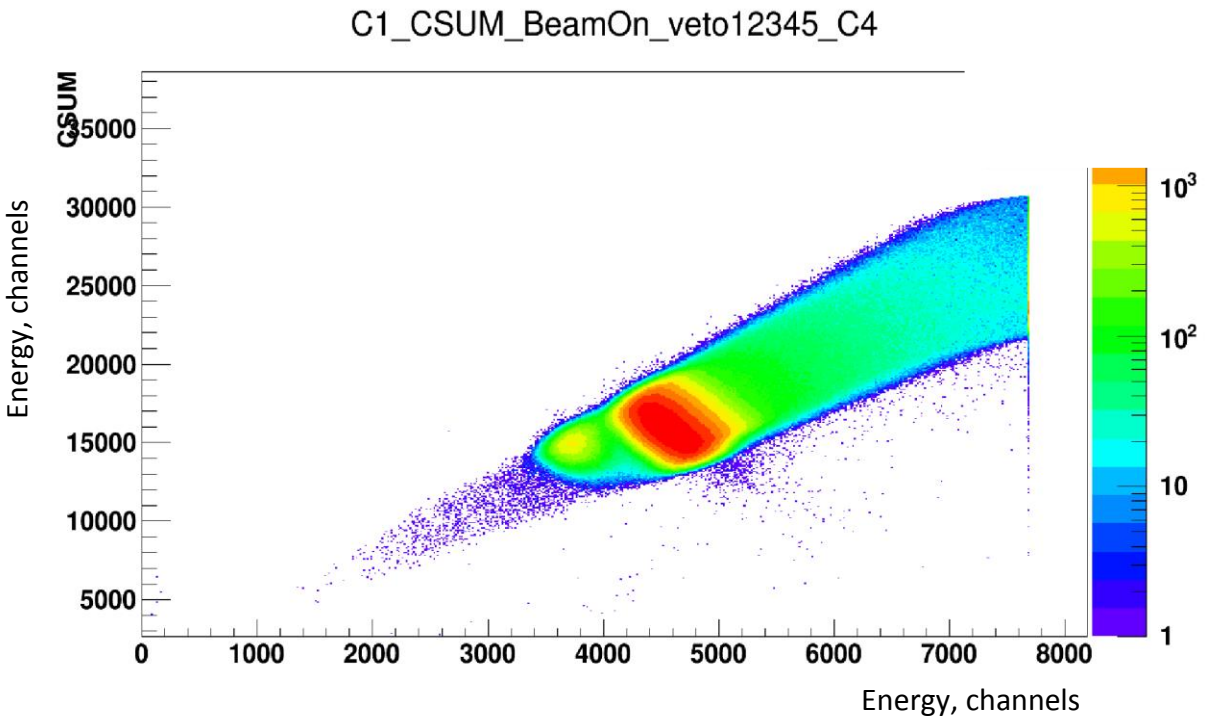

Figure 4. 17: On the y-axis sum of energies in units of channels from C1, C2, C3, C4, C5 pads plotted versus energy in C1 in units of channels (implantation phase). The conditions for this histogram were such that allowed to see only those isotopes that were traveling through central pads only and not beyond pad C4.

To rule out any presence of ^{32}Cl beta-delayed protons in the ^{35}K spectrum one would need to get a good spectrum for ^{32}Cl. The degrader was set at 32.5^0 to stop ^{32}Cl in the middle of the AstroBoxII. One must note that a number of ^{32}Cl implanted during in the C4 and C5 pads during the ^{35}K run was significantly smaller than an amount of ^{32}Cl during the ^{32}Cl separate run. In Table 4.4 the comparison is given between the numbers of ^{32}Cl implanted during the ^{35}K run and the ^{32}Cl separate run.

		C2	C3	C4	C5
^{35}K run	^{32}Cl			326228	852626
	^{35}K	190900	2858440	8811409	1305937
^{32}Cl run	^{32}Cl	2044416	9363743	6244032	294499

Table 4. 4: Comparison between the numbers of ^{32}Cl during the ^{35}K tune and ^{32}Cl tune.

One of the issues during the run with ^{32}Cl was that the energy spectra obtained for the central pads where most of ^{32}Cl was implanted (the C2, C3, and C4 pads) have significant difference in the position of the two main peaks at 762(5) keV and 991(5) keV. As can be seen from the Fig. 4.18 there is a progressive “migration” of the 762 keV and 991 keV peaks from lower to higher energy.

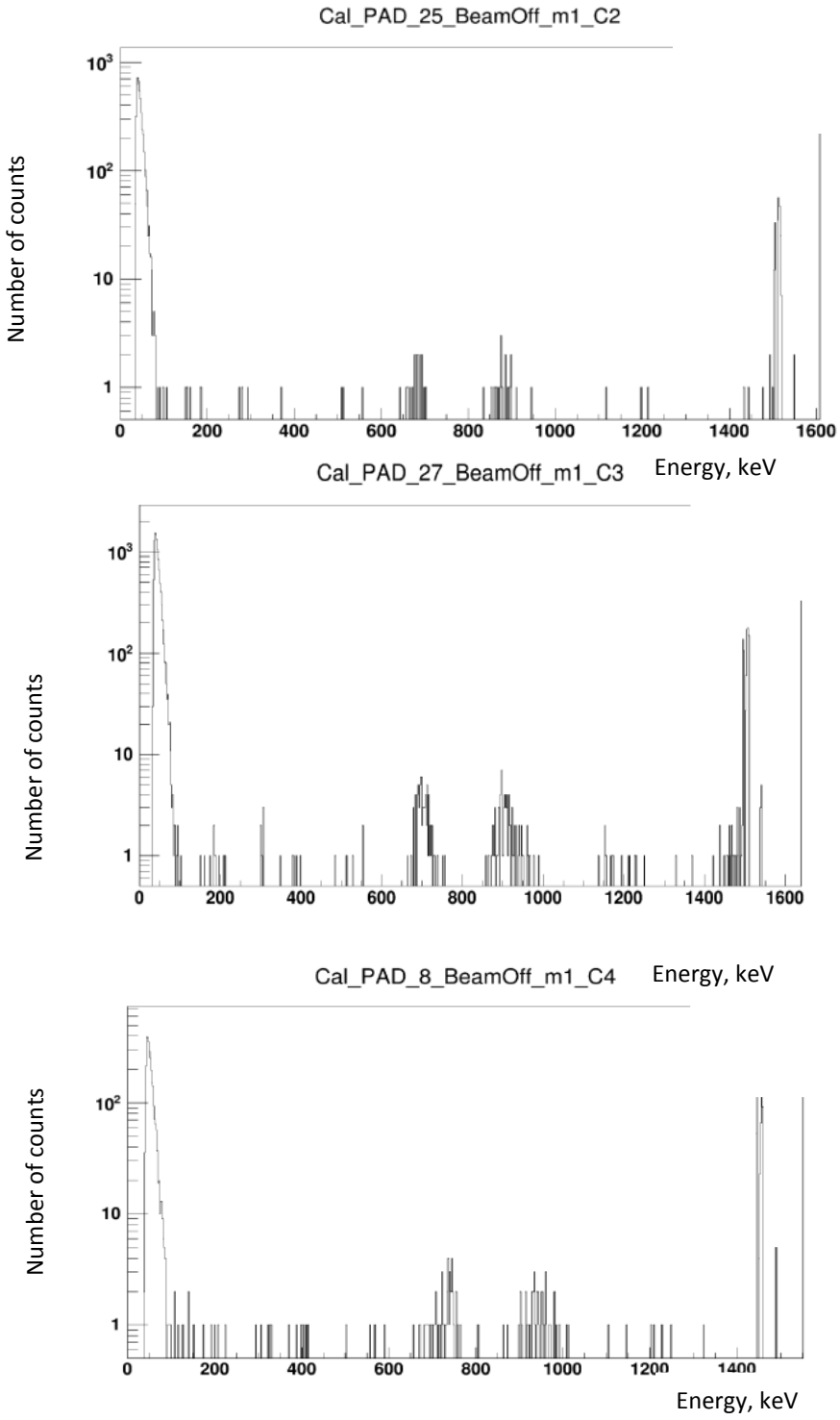

Figure 4. 18: Proton energy spectra for ^{32}Cl for the C2 (top), the C3 (middle), and the C4 (bottom) pads on the x-axis versus number of counts on the y-axis. As can be seen the position of the major peaks are shifted relative to one another. Peaks above 1400 keV correspond to overflows in the ADCs (due to gain shift correction)

The shift is significant at around ~20 keV when going from the C2 to the C3 and then to the C4 pad. The side pads on the other hand show little or no shift at all (within the statistical uncertainty). The closest possible peak in Fig 4.18 is around 420 keV, but one must note that the absolute branching ratios for beta delayed protons coming from ^{32}Cl is about one order of magnitude smaller than from ^{35}K [29]. Even more so, the ratio of the number of implants of ^{32}Cl in the ^{35}K run to the number of implants of ^{32}Cl in the ^{32}Cl run yields the value ~1/20. This ratio combined with much smaller absolute branching ratio for beta delayed protons from ^{32}Cl rules out any presence of protons from ^{32}Cl in the ^{35}K spectrum. It provides strong evidence that the measured proton group in both the July and October experiments indeed is coming from ^{35}K beta-delayed protons. If the data from the two experiments on ^{35}K are combined it is possible to build one spectrum for the multiplicity one events.

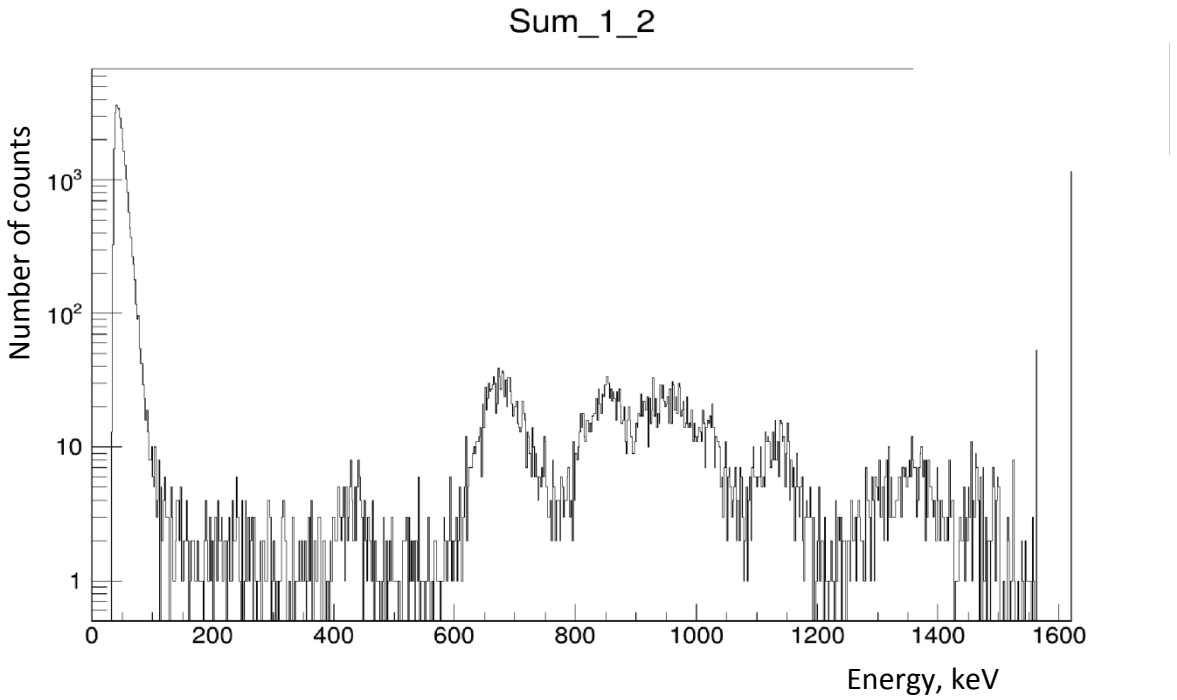

Figure 4. 19: Combined proton energy spectrum of ^{35}K from the July and October experiments (multiplicity one) for the C2, C3 and C4 pads on the x-axis versus number of counts on the y-axis.

From Fig. 4.19 it is possible to see that around ~250 keV region there is a possible peak forming, but the statistics are very limited. The final measured states for ^{35}Ar will be shown in the conclusion chapter.

5. CONCLUSIONS

In this work the AstroBoxII detector was used to determine astrophysically relevant resonances in ^{35}Ar. States that lie just above the proton separation threshold S_p (5896.3(8) keV for ^{35}Ar [32]) are of particular importance. The Gamow peak for the reaction ^{34}Cl+p will depend on the temperature of the stellar environment: for novae explosions (~0.4 GK) it sits at 433 keV above the S_p and for the X-ray bursts (~1GK) 634 keV above the S_p. The newly identified resonance at ~ 443(11) keV is located within the Gamow window for the typical temperatures of both novae and X-ray bursts. The 11 keV error consists of 3 keV statistical and 10 keV systematic errors.

The final measured decay scheme and levels reported in this work are shown in the Fig. 5.1.

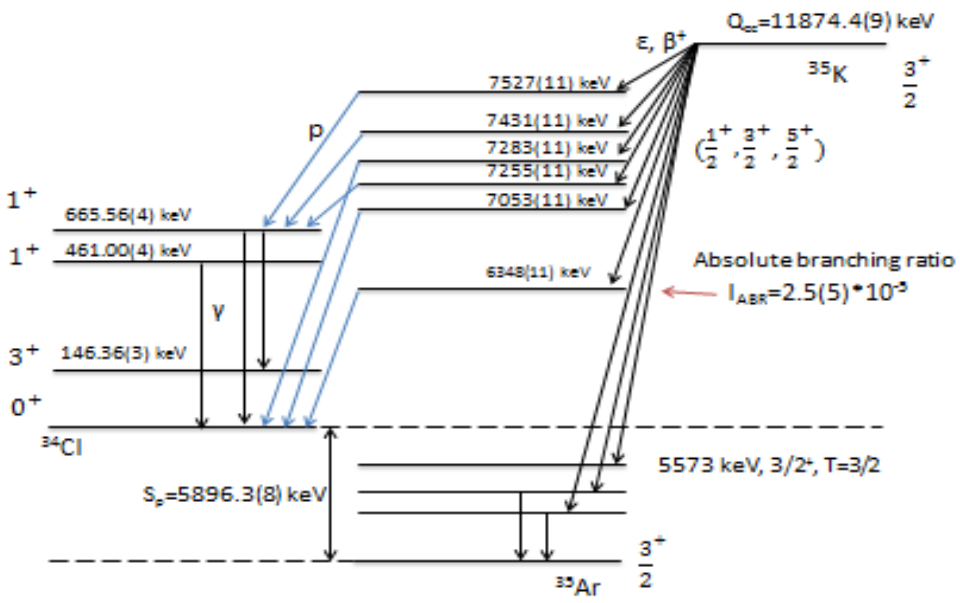

Figure 5. 1: The final measured proposed states for ^{35}Ar from the measurement of the beta-delayed protons. The state assignments assume all decays go to the ground state in ^{34}Cl.

From Fig. 5.1 the state at 6348(11) keV is identified as corresponding to the 443(11) keV proton group measured in the present experiment. Its absolute proton branching ratio was determined to be 0.000025(5). A state with similar energy was also reported in the work of Fry et al. [24] where the states in ^{35}Ar were populated by the ^{36}Ar(d,t)^{35}Ar reaction. In that experiment it was determined at 6334(3) keV. It is important to notice that in the present experiment it was not possible to tell whether a proton-unbound state in ^{35}Ar decayed to the ground state of ^{34}Cl or to the metastable state at 146.36(3) keV [29]. Given the half-life of the metastable state ~ 32 min and the setup of the experiment (triggering the data acquisition system only from the AstroBoxII) it was not possible to see delayed gammas corresponding to a transition from the metastable state to the ground state. Therefore it is reasonable to assume that both decay modes are possible. For the decay to ^{34}Cl^{m} only one possible state in ^{35}Ar can be populated, namely 5/2^{+}.

The expression (2.55) from the Chapter II allows an estimation of the resonant reaction rate for ^{34}Cl+p. The only value that is missing from the experiment is the resonance strength $\omega\gamma$, but it can be estimated with certain assumptions. The expression for the resonance strength is given by $\omega\gamma \equiv \omega\frac{\Gamma_p\Gamma_\gamma}{\Gamma_p+\Gamma_\gamma}$. Both Γ_p and Γ_γ are unknown but they can be estimated. The expression for the proton width Γ_p is given by the equation (2.57) from the Chapter II. The value for Γ_γ can be approximated from *Weisskopf estimates*. Then, by evaluating a single-particle partial width one can, with an assumption for the spectroscopic factor, calculate the reaction rate for a given resonance and compare it to the other calculated rates, such as a JINAWEB calculation. The calculation of a single-particle partial width for the new resonance was done with the program written by V**.** Goldberg and S. Fayans [59], which calculates a width for levels in a Woods-Saxon potential. The orbital momentum of the incident proton was taken to be $l = 0$. Higher values have much smaller probabilities penetrating the centrifugal barrier. The value obtained, assuming a maximal spectroscopic factor, was approximately 0.4 eV. It is important to note that in the present work the numerical value of spectroscopic factor is not known. Therefore it was decided to set to $C^2S = 0.1$, which yields $\Gamma_p = C^2S * 0.4\ eV = 0.04\ eV$. To evaluate the partial gamma width, Γ_γ, a *Weisskopf estimate* [eq. 2.31, 2.34 from the Chapter II] was used. ^{35}Ar in

the ground state has spin-parity $3/2^+$. The states that are populated by beta decay of ^{35}K have possible spin-parity combinations $1/2^+$, $3/2^+$, $5/2^+$ .Therefore the most likely transitions to consider are M1 and E2, as E1 is not allowed in this case due to parity conservation, and higher order multipole transitions are many orders of magnitude smaller. For an M1 transition, the Γ_γ width was estimated at 0.82 eV and for an E2 transition it was 0.0087 eV. Since the probability for M1 in the calculation is almost two orders of magnitude bigger it is going to be the dominant channel for the gamma transitions.

Another important point needs to be made. In the expression (2.56) (The Chapter II) for the resonance strength, the value of ω is dependent on the spin-parity of the resonances in ^{35}Ar as well as values for angular momentum of the target (^{34}Cl) and the projectile (proton). All three resonances possibilities ($1/2^+$, $3/2^+$, $5/2^+$) in ^{35}Ar need to be considered. However parity conservation and the selection rules for angular momentum will give the same value of ω=1 for all three states (^{34}Cl in the ground state). Also for the calculation of the reaction rate of $^{34}Cl^m$+p the resonance in ^{35}Ar has to be higher by 146.36(3) keV and ω=3/7. Taking all of the above into consideration and using expression (2.55) from the Theory Chapter, the astrophysical reaction rates of ^{34}Cl+p and $^{34}Cl^m$+p are presented in the Fig. 5.2.

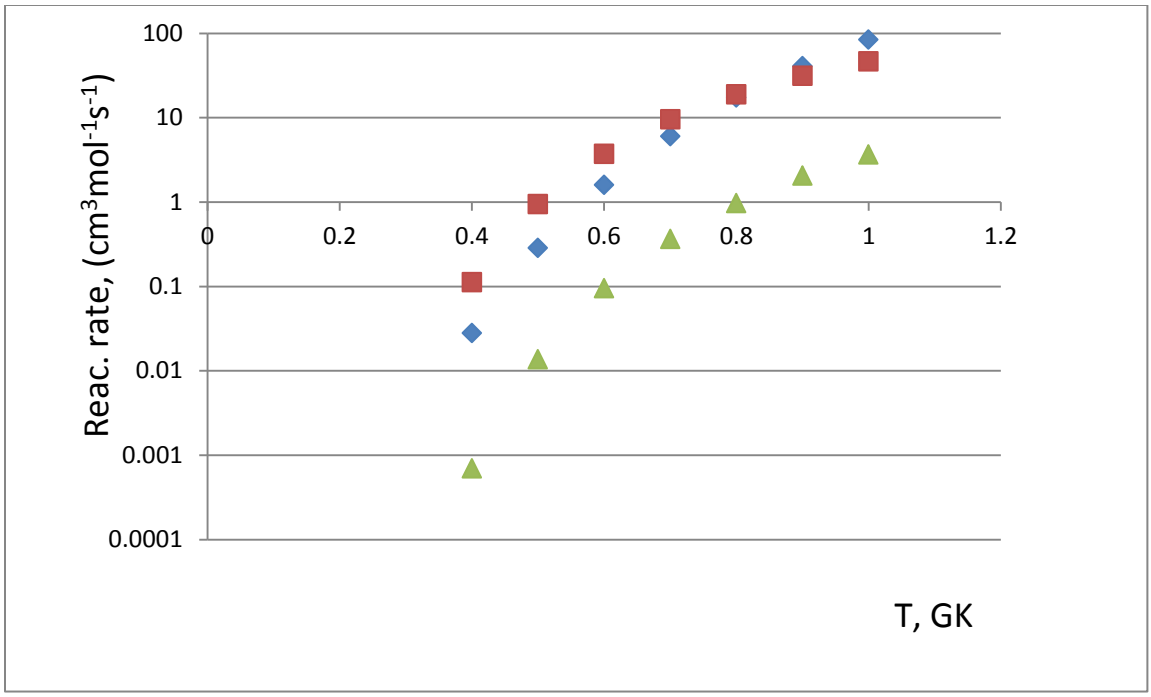

Figure 5. 2: Evaluated reaction rates from the present experiment compared to JINAWEB theoretical calculation. The blue dots represent the JINAWEB calculation [60] for ^{34}Cl in ground state plus proton. The red and green dots show the calculation in the present work for ^{34}Cl in ground state plus proton and ^{34}Cl in metastable plus proton, correspondingly.

As it can be seen from the Fig. 5.2 the calculation from JINAWEB (blue dots) shows similar rate dependence. JINAWEB gives a theoretical rate from T. Rauscher as part of REACLIB V 1.0 release) [61]. The reaction rate of ^{34}Cl^{m}+p (green dots) is significantly smaller but certainly can have some contribution at temperatures ~ 1 GK.

The newly discovered resonance in this work at 443(11)keV and an evaluation of the reaction rate of ^{34}Cl+p suggest a possibly faster rate than previously thought for the temperature range considered here. It is worth mentioning that the uncertainty for the estimated reaction rate can be quite large due to the unknown actual values for the spectroscopic factor as well as proton and gamma widths. It can easily exceed an order of magnitude. Therefore, only precise measurements for the resonance strength can provide an accurate value of the rate. However

even with some reasonable assumption for the spectroscopic factor one can obtain an estimate. Also it is worth noting that the JINAWEB calculation does not provide any information about $^{34}Cl^{m}$+p reaction. If $^{34}Cl^{m}$ is present in sufficient amount in Novae or X-ray bursts this reaction can have some contribution to the total rate. This is especially important for X-ray bursts with higher peak temperatures (~1 GK) than Novae.

There were some issues discovered during the series of experiments performed with the AstroBoxII. One of the main causes of the gain shift was temperature instability. Even a change of temperature of about 0.5 K can cause a visible shift (few keV) in the spectra. Therefore it would be useful to have a temperature sensor inside of the AstroBoxII to continuously monitor this for possible gain shift. Writing this information into a data stream can facilitate future analysis of how the temperature affects gas gain. Another big issue discovered with the detector was how the AstroBoxII was responding to higher particle rates as was seen in the ^{32}Cl experiment. The number of particles per unit time implanted in the ^{32}Cl experiment was higher than in ^{35}K measurement by about an order of magnitude. It caused very large 30-40 keV shifts for the two proton groups when going from the C2 to C3 and C4 pads. Also the live time during the beam-on period was around 90%. Understanding the cause of this effect and how to mitigate it will be very important for future experiments with other isotopes.

REFERENCES:

[1] E. M. Burbidge et al. Rev. of Mod. Phys. Vol 29, N4 1957

[2] J. Jose, C. Iliadis Rep. Prog. Phys. 74 (2011) 096901

[3] K. S. Krane Introductory Nuclear Physics by John Wiley & Sons, 1988

[4] J. D. Cockcroft et al., Proceeding of the Royal Soc. A, vol 136, pp. 619-630, 1932

[5] C. Iliadis Nuclear Physics of Stars, Wiley-VCH, 2007

[6] C. C. Lauritsen et al. Science, Vol. 79, Issue 2045, pp. 234-235, 1934

[7] D. N. F. Dunbar et al. Phys. Rev. 92, 649 1953

[8] M. Arnold et al. Univ. Libre de Brux. CP226, B-1050

[9] Claus E. Rolfs Cauldrons in the Cosmos, Univ. of Chicago Pr, 1988

[10] Donald Perkins Particle Astrophysics

[11] C. Iliadis, A. Champagne, J. Jose, S. Starrfield, and P. Tupper, Astrophys. J. Suppl. Ser. 142, 105(2002)]

[12] J. Jose and M. Hernanz J. Phys. G: Nucl. Part. Phys. 34 (2007) R431-R458

[13] S. Chandrasekhar The Lon., Edin., and Dub. Phil. Mag. and Jour. Of Science, 592-596 (1931)

[14] Cornish, Neil J. (1998). "The Lagrange Points"

[15] J. Jose et al. Nucl. Phys A777 (2006) 550-578

[16] A.W. Shafter, in: M. Hernanz, J. José (Eds.), Classical Nova Explosions, in: AIP Conference Proceedings, vol. 637, AIP, New York, 2002, p. 462

[17] B. Warner, Cataclysmic Variable Stars, Cambridge Univ. Press, Cambridge, 1995.

[18] https://www.nasa.gov/sites/default/files/thumbnails/image/gkper.jpg (08/2018)

[19] A. Parikh et al. Prog. In Particle and Nucl. Phys 69, 225-253, 2013

[20] Walter H. G. Lewin, Jan Van Paradijs, Ronald E. Taam X-ray bursts

[21] J. A. Hoffman, H.L. Marshall, W.H.G. Lewin, Nature 271 (1978) 630

[22] K. Lodders, S. Amari Presolar grains from meteorites: **arXiv:astro-ph/0501430**

[23] S. Amari, X. Gao, L.R. Nittler, E. Zinner, J. José, M. Hernanz, R.S. Lewis, Astrophys. J. 551 (2001) 1065

[24] C. Fry et al. Phys. Rev. C91, 015803 (2015)

[25] R. L. Kozub et al. Phys Rev. Vol. 172 Num. 4, 1968

[26] R. R. Johnson and R. J. Griffiths Nuc. Phys. A108 p.(113-123), 1968

[27] R. R. Betts et al. Phys. Rev. C Vol.8, N2, 1973

[28] G. T. Ewan et al. Nucl. Phys. A343, 1980

[29] https://www.nndc.bnl.gov/ (09/2018)

[30] P. Banerjee et al. Phys. Rev. C 97, 065807 2018

[31] C. L. Cowan, Jr., F. Reines, F. B. Harrison, H. W. Kruse, A.D. McGuire Science Vol. 124 N.3212 (1956)

[32] (NNDC data sheet) https://www.nndc.bnl.gov/chart/reCenter.jsp?z=0&n=1 (10/2018)

[33] https://www.nndc.bnl.gov/ensdf/EnsdfDispatcherServlet (10/2018)

[34] J. Suhonen From Nucleons to Necleus

[35] J. Janecke Nuclear Physics 73 (1965) 97-112

[36] D.V. Sivuhin Nuclear Physics, Vol. 5, Part 2 (1986)

[37] L.D. Landau and E. M. Lifshitz Quantum Mechanics, non-relativistic theory (1963)

[38] I. O. Vakarchuk Quantum Mechanics (2004)

[39] M. Pfutzner, L. V. Grigorenko, M. Karny, and K. Riisager, arXiv:1111.0482v1 (nucl-ex)

[40] D. H. Youngblood Nucl. Inst. and Meth. In Phys Res. B56/57 (1991) 991-995 North-Holland

[41] E. *Lawrence et al. Phys. Review. APS 40(1): 19-35 (April 1, 1932).*

[42] R. Geller, Peroc. 1st Int. Con. Ion Source, Saclay, p. 537, 1969 (ECR sources)

[43] R. E. Tribble, R.H. Burch and C.A. Gagliardi, Nucl. Instr. and Meth. A285 (1989) 441-446

[44] R. E. Tribble, C. A. Gagliardi and W. Liu, Nucl. Instr. and Meth. B56/57 (1991) 956-959

[45] http://lise.nscl.msu.edu/lise.html (version 10.0.10)

[46] http://www.micronsemiconductor.co.uk/product/x1/ (11/2018)

[47] http://www.micronsemiconductor.co.uk/product/msx25/ (11/2018)

[48] E. Pollacco, et al. Nucl. Instr. and Meth. Phys. A 723 (2013) 102-108

[49] A. Saastamoinen, et al. Nucl. Instr. and Meth. Phys. Vol. 376 (2016) 357-360

[50] Y. Giomataris, et al. Nucl. Instr. and Meth. Phys. A, 376 (1) (1996) 29-35

[51] Dr. A. Saastamoinen, Cyclotron Institute, TAMU (private communication)

[52] S. Agostinelli et al. Nucl. Instr. and Meth. Vol 506, Issue3 p.250-303 (2003)

[53] https://www.mesytec.com/products/nuclear-physics/MPR-16.html (11/2018)

[54] https://www.mesytec.com/products/nuclear-physics/MSCF-16_F_V.html (11/2018)

[55] J.-C. Thomas et al. Eur. Phys. J. A 21, 419-435 (2004)

[56] http://www.srim.org/ (version SRIM-2013.00) (11/2015)

[57] https://root.cern.ch/ (09/2018)

[58]https://www.nndc.bnl.gov/nudat2/getdataset.jsp?nucleus=34CL&unc=nds (retrieved 06/2019)

[59] A. M. Mukhamedzhanov et al. Phys. Rev. C81, 054314 (2010)

[60] https://www.jinaweb.org/ (02/2019)

[61] Cyburt, R. H. et al. ApJS (189) 240 (2010)